FINAL REPORT

INVESTIGATION OF DELAYED CRACKING IN PIVOT STEEL BOX GIRDERS

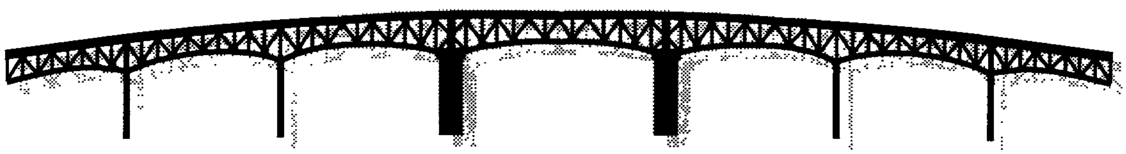

MARGARIT G. LOZEV, Ph.D.
Senior Research Scientist
Virginia Transportation Research Council

GLENN A. WASHER, P.E.
Research Structural Engineer
Federal Highway Administration

WILLIAM J. WRIGHT, P.E.
Research Structural Engineer
Federal Highway Administration

V · I · R · G · I · N · I · A
VTRC
TRANSPORTATION RESEARCH COUNCIL

VIRGINIA TRANSPORTATION RESEARCH COUNCIL

Standard Title Page - Report on State Project

Report No.	Report Date	No. Pages	Type Report:	Project No.: 9133-010
			Final	
VTRC 97-R18	June 1997	110	Period Covered: April 96-June 97	Contract No.

Title and Subtitle: Investigation of Delayed Cracking in Pivot Steel Girders	Key Words: high-strength steel, box girder, delayed cracks, nondestructive evaluation, metallurgical and failure analyses, crack growth, brittle and fatigue failure assessment
Authors: M. G. Lozev, G. A. Washer, and W. J. Wright	
Performing Organization Name and Address: Virginia Transportation Research Council 530 Edgemont Road Charlottesville, VA 22903	
Sponsoring Agencies' Name and Address Virginia Department of Transportation 1401 E. Broad Street Richmond, VA 23219	
Supplementary Notes	

Abstract:

This report describes the results of an investigation to find the cause of the delayed cracking in the welds of the fracture-critical steel pivot box girders fabricated for the George P. Coleman Bridge. Through the use of different nondestructive methods, more than 200 transverse and longitudinal cracks were found.

The possibility of unique, rare, and very long-term delayed cracking (cold or hydrogen-induced cracking) was supported by the results of the hydrogen content analysis, residual stress measurements, and macro-microstructural metallography and fractography.

There was strong evidence that a susceptibility to hydrogen-induced cracking of the weld metal in the north girder developed during fabrication and that this susceptibility, the presence of hydrogen in the weld and base metal, and residual stresses combined to cause cracking to occur.

The great number of cracks detected in the welds of the north girder, coupled with the very large total crack lengths, demonstrated that these welds have been and still are inordinately susceptible to cold cracking.

Calculations showed that brittle fracture could occur in the partial penetration groove weld under the worst conditions, but this is not probable. Calculations also showed that there is little probability that the cracks will extend in any significant amount because of fatigue during the life of the bridge.

The author recommends that the north box girder be inspected by magnetic particle testing or eddy current testing at least every 6 months for the next 3 years and that cracks be repaired when found.

FINAL REPORT

INVESTIGATION OF DELAYED CRACKING IN PIVOT STEEL BOX GIRDERS

Margarit G. Lozev, Ph.D.
Senior Research Scientist
Virginia Transportation Research Council

Glenn A. Washer, P.E.
Research Structural Engineer
Federal Highway Administration

William J. Wright, P.E.
Research Structural Engineer
Federal Highway Administration

Virginia Transportation Research Council
(A Cooperative Organization Sponsored Jointly by the
Virginia Department of Transportation and the
University of Virginia)

Charlottesville, Virginia

June 1997
VTRC 97-R18

ABSTRACT

This report describes the results of an investigation to find the cause of the delayed cracking in the welds of the fracture-critical steel pivot box girders fabricated for the George P. Coleman Bridge. Through the use of different nondestructive methods, more than 200 transverse and longitudinal cracks were found.

The possibility of unique, rare, and very long-term delayed cracking (cold or hydrogen-induced cracking) was supported by the results of the hydrogen content analysis, residual stress measurements, and macro-microstructural metallography and fractography.

There was strong evidence that a susceptibility to hydrogen-induced cracking of the weld metal in the north girder developed during fabrication and that this susceptibility, the presence of hydrogen in the weld and base metal, and residual stresses combined to cause cracking to occur.

The great number of cracks detected in the welds of the north girder, coupled with the very large total crack lengths, demonstrated that these welds have been and still are inordinately susceptible to cold cracking.

Calculations showed that brittle fracture could occur in the partial penetration groove weld under the worst conditions, but this is not probable. Calculations also showed that there is little probability that the cracks will extend in any significant amount because of fatigue during the life of the bridge.

The author recommends that the north box girder be inspected by magnetic particle testing or eddy current testing at least every 6 months for the next 3 years and that cracks be repaired when found.

FINAL REPORT

INVESTIGATION OF DELAYED CRACKING IN PIVOT STEEL BOX GIRDERS

Margarit G. Lozev, Ph.D.
Senior Research Scientist
Virginia Transportation Research Council

Glenn A. Washer, P.E.
Research Structural Engineer
Federal Highway Administration

William J. Wright, P.E.
Research Structural Engineer
Federal Highway Administration

INTRODUCTION

The new George P. Coleman Bridge on Rte. 17 over the York River currently carries 28,000 vehicles per day, with traffic projections of 43,000 vehicles per day in the year 2015.[2] The old two-lane bridge, the second-largest double-swing-span bridge in the world, was replaced in record time and was the first bridge replacement "floated" into position with everything ready to carry traffic.[3] The six new sections were preassembled on temporary supports 48 km (30 mi) from the bridge at Norfolk International Terminal (NIT) from March 1995 to April 1996 and then floated on barges to the bridge site in April and May 1996. The innovative construction techniques and extensive preassembly radically cut time and limited bridge closure during the project to just 12 days.[2]

The Materials Division of the Virginia Department of Transportation (VDOT) requested an analysis of metal cores taken from the pivot metal box girders fabricated for the expansion of the bridge.[1] More than 100 cracks were observed in the first girder after it was shipped by the fabricator from Indiana to NIT. The cracks were removed by grinding and repaired by manual welding in the field. Questions have been raised about the safety of these fracture-critical members and the entire superstructure because the interaction between welding-induced defects and fatigue stresses during service is extremely damaging. Was the base metal preheated in accordance with the specifications before welding? What caused the delayed weld cracking? Should these welds be monitored? If so, what kind of methods should be used? How often should the welds be monitored and for how long?

PROBLEM STATEMENT

There is a great deal of concern about the cause of the delayed transverse cracking in the groove and fillet welds of the fracture-critical box girders fabricated for the Coleman Bridge. The cracking probably occurred in the fabrication shop, during handling and shipping, during preassembly, and after on-site erection.

PURPOSE AND SCOPE

The objectives of this study were to perform a comprehensive laboratory failure analysis of the steel cores and a comprehensive field nondestructive evaluation (NDE) of the box girders of the Coleman Bridge before and after on-site erection and to assess the potential for crack growth.

METHODS

A literature search, an NDE, metallurgical and failure analyses, and an assessment of the potential for crack growth were performed during this investigation. Equipment belonging to the Virginia Transportation Research Council (VTRC) and the Federal Highway Administration (FHWA) was used to conduct this investigation. In addition, the services of Law Engineering and Environmental Services, Inc.; SI-TECH, Inc.; American Stress Technologies (AST), Inc.; Stress Engineering Services (SES), Inc.; Chicago Spectro Service Laboratory, Inc.; Aston Metallurgical Services, Inc.; and Sherry Laboratories, Inc., were procured.

1. *Literature search.* The literature on similar delayed cracking cases was reviewed.

2. *Comprehensive NDE.* Visual testing (VT), magnetic particle testing (MT), radiographic testing (RT), and eddy current testing (ET) of the fillet welds and heat-affected zone (HAZ) were performed after the repairs, before and after the swing trusses were floated from NIT, and after erection. The depth of the cracks was measured using the drop potential testing (DPT) method and an alternating current field measurement (ACFM) device. Acoustic emission (AE) monitoring after erection was also performed.

3. *Stress measurements.* X-ray diffraction, magnetoelastic, and blind hole-drilling residual stress measurements of the welds, HAZ, and base metal were conducted at the bridge site. Applied stress measurements were obtained during normal traffic operations.

4. *Specimens.* Metal cores were taken from seven locations. The cores were composed of the weld metal with HAZ and base metal (flange and web, or web and stiffener). The cores were used later to fabricate tension, Charpy V-notch (CVN), compact tension (CT), metallographic, and fractographic testing specimens from the weld, HAZ, and base metal.

5. *Metallurgical and failure analysis.* Hardness testing of the weld, HAZ, and base metal (longitudinal, transverse, and vertical) was done. Macro- and microstructure metallographic analyses of the weld, HAZ, and base metal (grain size) were performed. Tension tests at room temperature and the CVN test at -23° C (-10° F), -18° C (0° F), and -7° C (20° F) were performed along with liquid nitrogen brittle fracturing to open and separate the crack surfaces. Fractographic examinations of the fractured surfaces from the tension, CVN, and compact specimens and exposed crack surfaces were conducted. The chemical and microstructure composition of the base metal (top flange, web, and stiffeners) and the weld metal was determined using the test specimens or remaining metal parts after machining. The accuracy, resolution, and errors for the crack width and length measured with the NDE methods were compared and correlated with the results of the mechanical, metallographic, and fractographic analyses.

6. *Fracture analysis.* The potential for cracks growing larger either by fatigue or brittle fracture was assessed.

DESCRIPTION OF THE GEORGE P. COLEMAN BRIDGE

The bridge consists of six sections: two swing spans, two anchor spans, and two suspended spans. Figure 1 shows the elevation of the bridge. At each pier, the swing spans rest on a fracture-critical steel box girder connected to the pivoting mechanism of the structure. The weight of the box girder is around 65 tons. Typical details and dimensions of the box girders are shown in Figure 2.

Steel manufactured in accordance with ASTM A852 (ASTM A709, Grade 70W, or AASHTO M270, Grade 70W), a C-Mn low-alloy high-strength steel, was used to fabricate the box girders. This steel, hereinafter called A709-70W steel, which has a smaller plate thickness than traditional steel, was used to reduce the weight of the new bridge and is a relatively new bridge steel. It is a quenched and tempered version of the weathering steel manufactured in accordance with ASTM A588.[4,5] Quenching and tempering increase strength and improve toughness. A typical microstructure is tempered martensite. In accordance with ASTM designation A 709/A709M-95a, the minimum yield strength is 485 MPa (70 ksi) and the tensile strength is 620 to 760 MPa (90 to 110 ksi). The chemical composition is equivalent to that specified in ASTM A852/A852A. The steel was provided by two producers: Burns Harbor Plant, a division of Bethlehem Steel Co., supplied the base metal plates for the north girder, and U.S. Steel Group, a division of USX. Co., supplied the base metal plates for the south girder. Different heats were used in producing the plates for the flanges, webs, and stiffeners. The chemical composition and mechanical properties reported in the mill reports were in accordance with the ASTM specifications. No maximum value for the hydrogen content in the plates was stipulated.

Stupp Brothers Bridge and Iron Co., a division of Stupp Brothers, Inc., St. Louis, Missouri, was responsible for fabricating the steel box girders. However, to meet the schedule, the company subcontracted one box girder and half of the trusses to Vincennes Steel Co., Vincennes, Indiana.[3] Both steel fabricators on the project were members of the American Iron and Steel Institute (AISI).

To produce high-quality welds with good penetration using an automated welding process, the companies used submerged arc welding (SAW).[3] This welding was supposedly performed in accordance with AWS D1.5-88, Bridge Welding Code, and the specifications of the 1991 AASHTO Fracture Critical Material Guide. For automatic SAW on the Grade 70 steel, the companies used Lincoln LA100 (AWS A5.23 F96-EM2-M2) wire and 880M flux with an electrode extension of 19 mm (¾ in). Welding was done with 2-mm (3/32-in) wire at a travel speed of 300 mm/min (12 in/min) at 370 A, 30 V. For manual shielded metal arc welding (SMAW), Murex 9018 (AWS 5.5 E9018-M) electrodes were used. The preheating temperature ranged from 93 to 177° C (100 to 350° F). Maximum interpass temperatures ranged from 204 to 232° C (400 to 450° F). SMAW in the horizontal position calls for 5-mm (3/16-in) electrodes at a travel speed of 254 mm/min (10 in/min) at 220 A, 26 V. Welds in the flat position call for a travel speed of 280 mm/min (11 in/min). No postweld heat treatment was required for either process.[3] A 1-hour postweld heat treatment at 205° C (400° F) minimum and 260° C (500° F) maximum was required for the weld repairing in the field. Undermatching is not permissible for groove and fillet welds, and filler metal suitable for welding on A709-50W steel was not used on the A709-70W steel. The welding procedures were reviewed and approved by VDOT.

Figure 3 shows sketches for the weld seams selected to join the flanges, webs, vertical stiffeners, and diaphragms. Both fabricators used MT to inspect the welds: 100 percent for web-to-bottom flange (tee) welds and 10 percent for all fillet (tee) welds; 100 percent ultrasonic testing (UT) was used to inspect web-to-top flange (groove, tee) and web-to-connection angle (corner) welds. NDE was probably performed in accordance with AASHTO requirements 48 hours after fabrication. At least 98 percent of the welds tested passed inspection.[3]

Vincennes Steel Co. fabricated and inspected the first box girder (B121, or the north girder) from December 1994 to January 1995. No rejections were documented, but a few cracks were repaired in the shop.[6] The first girder was shipped to NIT in February 1995. Stupp Brothers Bridge and Iron Co. fabricated and inspected the second box girder (A121, or the south girder) in April and May 1995. No rejections were documented in the NDE reports. Discontinuities were probably observed because MT of all repair areas was reported. The second girder was shipped to NIT in June 1995.

THE MECHANISM OF DELAYED CRACKING (COLD CRACKING OR HYDROGEN-INDUCED CRACKING)

One of the most difficult problems in the contemporary manufacturing of welded joints are delayed, or cold, or hydrogen-induced cracks. They represent more than 50 percent of all defects typical for the welded joints of low-alloy high-strength steels. As a result of extensive work, many aspects of this phenomenon are understood. Others, such as the moment of delayed crack nucleation, crack growth rate, and failure mechanism, are still to be clarified.[7]

The conditions that collectively result in hydrogen cracking can be recognized and may be stated simply as "sufficient hydrogen and sufficient stress in a susceptible microstructure at a temperature usually below 150° C (302° F)."[8] Delayed cracking occurs when all four conditions occur simultaneously. It is still uncertain how long an incubation period is required for hydrogen cracks to start and how long they can continue growing. Several periods have been proposed, varying from overnight to 1 year. There is evidence that when a plentiful supply of hydrogen is available, cracks start forming fairly soon after the weld has cooled, or months later, and grow to a detectable size within a few hours or years.

According to the most widely accepted model for hydrogen-induced crack formation (still being investigated), the preexisting defects in the metal, such as small inclusions, in the presence of existing stress may develop high local areas of biaxial or triaxial tensile stresses. Hydrogen diffuses preferentially to these sites with a dilated lattice structure. As the local hydrogen concentration increases, the cohesive energy and stress of the lattice decrease. When the cohesive stress falls below the local intensified stress level, fracture occurs spontaneously. Hydrogen then evolves in the crack volume, and the process is repeated.[9]

During welding, hydrogen is absorbed by the weld pool from the arc atmosphere. During cooling, much of this hydrogen escapes from the solidified bead by diffusion, but some also diffuses into the HAZ and the base metal. The critical level of hydrogen to induce cold cracking is alloy and microstructural dependent; in general, the more hydrogen present in the metal, the greater the risk of cracking. The principal sources of hydrogen in welding consumables are[8]:

- moisture or any other hydrogenous compounds in the coating of SMAW electrodes or in the flux used in SAW
- oil, dirt, and grease either on the surface or trapped in the surface layers of welding wires
- hydrated oxides, e.g., rust, on the surface of welding wires.

The principal sources of hydrogen from the material to be welded are[8]:

- oil, grease, dirt, paint, or rust on the surface and adjacent to the weld preparation area
- degreasing fluids used to clean the surface before welding
- hydrogen from the parent steel remaining from the original casting process in the interior of heavy, thick sections.

Control over the hydrogen level may be achieved either by minimizing the amount initially absorbed or by ensuring that sufficient hydrogen is allowed to escape by diffusion before the weld cools. There are no AASHTO requirements to measure the concentration of diffusible or residual hydrogen in deposited SAW metal during production welding.[10] It is assumed that if the recommended low-hydrogen consumables are used and the recommended preheating is performed, cold cracks should not occur. In consumables used to weld base metal with a minimum specified tensile strength of 552 MPa (80 ksi) to less than 689 MPa (100 ksi), the hydrogen content must not exceed the level of 8.9 ml/100 g (10 ppm).[11]

The presence of hydrogen appears to lower the stress level at which cracking will occur. In rigid structures, the natural contraction stresses are intensified because of the restraint imposed on the weld. Hydrogen embrittlement is strain-rate dependent, and the risk of cracking is greatest at slow rates. Delayed cracking is not normally revealed by high strain rate impact tests such as the CVN.

As a general rule for C-Mn low-alloy steels, the harder the microstructure, the greater the risk of cracking. A soft microstructure can tolerate more hydrogen than a hard microstructure before cracking occurs. The carbon-equivalent (CE) value accounts for the important elements that are known to affect hardening. According to the ANSI/AWS Bridge Welding Code, for fillet welds, cold cracking should not occur if the Vickers hardness number is less than 350 VH with high-hydrogen electrodes. With low-hydrogen electrodes, a hardness of 400 HV could be tolerated without delayed cracking.[10] No critical hardness level above which a high risk of cold cracking exists for A709 70W steel weld metal is specified in the Code or proposed in the literature. There is a recommendation in the Code that the selection of the critical hardness depend on steel type, hydrogen level, restraint, and service conditions.[10]

Preheating softens the microstructure and helps hydrogen escape by slowing the weld cooling rate. It is possible to avoid cold cracking in a susceptible microstructure by maintaining it at a sufficiently high temperature by postheating until sufficient hydrogen has diffused away.[8]

When hydrogen-induced cracking occurs as a result of welding, the cracks are located either in the HAZ of the base material or in the weld metal itself. Delayed cracks in the weld metal can be oriented longitudinally or transversely to the weld length. The cracks may be buried or may break the weld surface. Under the microscope, they are usually recognized as being predominantly transgranular, although in more alloyed deposits an increasing proportion has an intergranular morphology.[8] Typically, cold cracks in weld metal can occur at much lower levels of hardness than in the HAZ.

Cracking is more likely in weld metal under the following conditions:

1. **when little or no preheating was performed during the welding of plates with a thickness of 50 mm (2 in) or greater,**

2. **when alloyed weld metal is used (especially if the CE of the weld metal exceeds that of the base metal), or**

3. **when C-Mn weld metal is used that contains 1.5 percent or more Mn.[8]**

Delayed cracks are normally very difficult to detect, even when they break the surface, which does not often occur. When using direct current (DC) MT, subsurface cracks can be detected. For buried cold crack detection and identification, UT is greatly preferred to RT, but the use of conventional UT is not always successful.

Hydrogen-induced cracking of truss gusset plates of carbon steel conforming to the requirements of ASTM A36 has been reported.[12] The gusset plates failed in the HAZ via an intergranular microcracking mechanism because of hydrogen-assisted underbead and toe-weld cracking. Recently, two long and numerous shorter transverse cracks were observed in the bottom flange and at the web-to-flange plate connecting fillet welds throughout the girders in the Green River Bridge on I-26 near Asheville, North Carolina. Corten B weathering steel modified in accordance with ASTM A441 was used to fabricate the bridge. The metallographic and fractographic examination found that the cracks occurred 23 years ago at the time of fabrication and appeared to result from hydrogen-related cold cracking.[13] The bridge was closed, and repairs were completed in 2 years.

RESULTS AND DISCUSSION

Comprehensive NDE

Visual Testing (VT)

The first delayed cracks were originally found in the web-to-stiffener fillet welds in the north girder upon visual inspection following shipment to NIT in March 1995. The cracks were typically transverse to the welding direction in the weld crown. Some cracks propagated into the web base metal. A few cracks were discovered at the crown of the fillet weld in the longitudinal direction.

Magnetic Particle Testing (MT)

More than 100 cracks were discovered in the north girder by the MT conducted in March and April 1995. The Parker probe for longitudinal magnetization was used, and dry red particles were applied. MT was performed in accordance with ASTM E709, and the standard of acceptance was in accordance with Section 9.21 of the Bridge Welding Code.[10] The girder had a coating system, made up only of a zinc primer. The primer was removed at the electrodes to provide direct electrical contact with the metal surface. The second MT conducted by VDOT personnel in March 1996 (just before the preassemby was finished) detected 7 new transverse cracks in the far girder side in the web-to-stiffener No. 8 weld. The cracks were in the web plate and were approximately 6 mm (¼ in) long and 3 mm (1/8 in) deep. Two additional MTs were performed in June 1996 and April 1997. The prod MT method with dry red particles was used with a 100-mm (4-in) prod spacing, with continuous magnetization at 500 A DC.

Typical MT indications for the detected cracks are shown in Figure 4. **The locations of the crack indications in the box girder are shown in Figures 5 through 7. The most severe cracks were five transverse cracks detected at the web-to-top flange groove weld in the midspan, outside the south (far) side (see Figure 5, location F1). The potential of top flange fracture initiating from the existing transverse cracks in the midspan should be the subject of a great deal of concern. MT showed the crack length indications to be from 6 to 31 mm (¼ to 1¼ in) long. The actual crack length observed during the repair work was 6 to 12 mm (¼ to ½ in) longer. To excavate the cracks, the weld metal was completely removed in the crack areas.[6] This was an indication that some of these cracks were very deep and probably through-weld cracks.**

The distribution of the number and length of cracks in the north girder vs. time after fabrication is shown in Figures 8 and 9. Increased delayed cracking was observed in the web-to-top flange groove weld in June 1996 and in the web-to-bottom flange weld in April 1997. A steady decline of cold cracking was noticed in the web and flange-to-stiffener and diaphragm welds. The distribution of the number of cracks vs. length of crack for these three MTs is shown in Figures 10 through 12. Most of the transverse cracks were less than 50 mm (2 in) long. The longest longitudinal crack was more than 0.5 m (20 in) long and was detected in the web-to-stiffener and flange-to-diaphragm welds. Two longitudinal cracks longer than 375 mm (15 in) were detected in the web-to-top flange welds. MT reinspection after field repairs detected five transverse cracks 13 mm (½ in) long 13 to 25 mm (½ to 1 in) outside the repair areas and only one transverse crack 13 mm (½ in) long in the repair areas.

MT inspection of the south girder was performed at NIT in June through October 1995. Only four crack indications were observed. The locations and length of these cracks are shown in Figure 13.

Eddy Current Testing (ET)

The applied final coatings on the south girder and the paint removal at the MT electrodes to provide direct electrical contact with the metal surface were less than ideal during the June 1996 MT. Detecting transverse cracks in the weld crown once the final bridge coating is applied is still a difficult inspection problem. The possible solution is the use of ET.

ET is based on the principles of electromagnetic induction. When an alternating current is used to excite a coil, an alternating magnetic field is produced that generates circular eddy currents in conductive materials. If a test coil is moved over a discontinuity in a metal plate or weld at a constant clearance and constant rate of speed, a momentary change will occur in the reactance and current of the coil. This change can be amplified, detected, and displayed by electronic instruments. Because of the skin (eddy current heating) effect, the depth of penetration of eddy currents is relatively small and is a function of the probe frequency and the material conductivity and permeability. The most widely used application of ET is the inspection of nonferromagnetic materials, stainless steels, and ferromagnetic tubes. The use of ET for detecting cracks in thicker ferromagnetic sections such as bridge steel is not well developed.

Procedures for implementing this technology are not generally available outside the FHWA and VTRC NDE laboratories, and research is ongoing to establish a standard or procedure.[14,15]

VTRC NDE personnel began experimenting with ET in June 1996, when a computerized eddy current instrument (SmartEDDY 3000 System), owned by FHWA, and a hand-held eddy current instrument (DEFECTOMETER 2.837), owned by VTRC, were used to detect surface breaking cracks in the welds of the north pivot girder.

SmartEDDY 3.0 is a highly sensitive tester capable of operating in the absolute or differential mode, or both. It has the ability to record data in real time and in a format suitable for evaluation and archival storage. The values of drive levels (voltage peak) and frequencies can be selected independently. The instrument voltage range is 0 to 9 V peak to peak, and the frequency ranges from 5 Hz to 10 MHz. Zetec's Plus-Point Differential Weld Scan Probe was used to scan the surface of the welds. System calibration was performed at the start of each EC operation and was verified every 4 hours, or when a crack indication was discovered. No calibration specimens were available that had magnetic properties similar to those of the A709 steel used in the bridge, so calibration was conducted on the known cracks. The change in phase and amplitude caused by the cracks was small, but clearly measurable.

DEFECTOMETER 2.837 was developed by Institute Dr. Forster (Germany) specifically for maintenance inspection. It is extremely easy to use. It requires from the user a general knowledge of ET. The instrument is hand held and battery operated and uses a 4-MHz absolute probe with a 2-mm (0.1-in) probe footprint. This small footprint has the advantage of reducing the sensitivity to geometric indications. The instrument is self-balancing and displays indications as a normalized impedance.

Several transverse cracks that had been previously identified with MT on the north girder were selected for ET. The cracks were detected and verified with ET. One area contained a longitudinal crack at the weld (location H, June 1996 MT results). The metal was removed by grinding to observe the crack visually. The area had significantly different magnetic properties than the surrounding steel and weld metal. The inspection of this area with ET was not possible because of its unique material properties. This was identified as a potential problem, but its significance could not be determined from the available data. In addition to the areas containing known cracks, several areas without cracks were scanned, but no new cracks were found.

This preliminary field test showed that ET is an alternative to MT that will not adversely affect the coating system on the bridge. If ET were adopted for inspecting the south girder, MT or grinding could be performed to confirm the results, and the number of times the coating system had to be penetrated to make electrical contact would be significantly reduced. This would extend the life of the coating system and reduce the time required to inspect the welds.

Welds 211 m long at the south girder were tested over 8 days in August 1996. An EC reference standard, fabricated from A709 steel, was used for the calibration. Three electrode discharge machine (EDM) notches were machined into the standard. The notches were approximately 0.15 mm (6 mils) wide and 25 mm (1 in) long with depths of 0.5, 1, and 2 mm

(0.02, 0.04, and 0.09 in). The reference standard was unpainted. The girder had a complete coating system made up of a zinc primer and two layers of a nonconductive coating. The measurements of the coating system indicated an average thickness of 0.4 mm (16 mils). Lift-off changes, attributable to the coating system, were compensated for during the calibration process. Lift-off attributable to the coating was assumed to reduce signal amplitudes approximately 40 percent. Indications were determined by a simple reactance threshold equivalent to approximately 20 percent of the full screen height.

Table 1 describes the crack indications revealed during ET. Six were noted in the welds inside the girder, and 12 were noted in the outer welds. The surface in these areas was removed by grinding to allow verification of the ET results. ET reinspection of these areas was performed to verify that the cause of the indications had been removed. Visual observation during the grinding process confirmed one visible transverse crack 6 mm (¼ in) long, two visible longitudinal cracks 6 mm (¼ in) long, eight slag inclusions, six undercuts, and one weld rollover. The probability of detecting discontinuities under the paint was very high, with some probability of making an incorrect determination (overestimation) of cracklike indications. Much research remains to be done in ET of high-strength steels. However, the evaluation of the welds in the south girder demonstrated the viability of using ET to test painted ferromagnetic steels.

Alternating Current Field Measurements (ACFM)

Another technology used at the Coleman Bridge was the U9 ACFM device. The operation of this instrument is similar in theory to that of MT in that a magnetic field is induced in the material and the flux leakage caused by a crack is measured. The significant difference is that the flux leakage is measured by coils rather than by placement of particles on the material surface. The output signal of these coils can be analyzed quantitatively to determine the dimensions of a surface-breaking crack.

The evaluation of the longitudinal crack at location H was performed using the ACFM instrument. The results indicated that the crack was actually two crack segments. The first crack was 30 mm (1.2 in) long and 3.8 mm (0.15 in) deep, and the second was 11 mm (0.4 in) long and 2.4 mm (0.1 in) deep. These results were consistent with the MT results and were not affected by the unusual material properties in this area. These ACFM results were confirmed later during the metallographic and fractographic examinations.

The U9 ACFM instrument was shown to be effective at detecting and measuring longitudinal cracks in the weld. However, it is quite large and bulky, making it more difficult to use in the field. The ability of this instrument to detect cracks and measure crack depth makes it a valuable tool that resolves a long-standing problem. The benefits of this type of instrumentation far outweigh the inconvenience of the instrument's size and weight. The U9 ACFM system tested was leased from Technical Software Consultants, Inc., England. At present, FHWA is providing strong leadership in the bridge inspection field by bringing this innovative and well-developed technology to the United States.

Drop Potential Testing (DPT)

DPT, or the four-point probe technique, has been around for years, and its possible use for evaluating crack depth is still being investigated. If four electrodes are placed in contact with an electrically conducting object and current is passed between two outer electrodes, a potential will be produced between the other two inside electrodes (usually placed above surface-breaking cracks). For a fixed electrode arrangement and one material, an observed change in the current/potential ratio will represent a change in the depth of a crack. The CC-800B instrument, owned by VTRC, with an SP1-B probe was used to measure crack depth in different locations during this investigation. The crack depth varied from microns to 25 mm (1 in). The accuracy was ±10 percent. The measurements were performed at the weld face only on surface-breaking cracks. The depth of the cracks in locations A, H, and K (June 1996 MT results) were confirmed later during the metallographic and fractographic examinations. An additional comprehensive DPT in April 1997 revealed that the transverse crack in the web-to-top flange single-bevel groove weld at location T (April 1997 MT results) was 50 mm (2 in) long and 13 mm (½ in) deep in the weld. The depth was measured after 10 mm (3/8 in) of weld metal was removed from the face (crown) of the weld. **The same crack is propagating in the top flange. Its visible length there was 6 mm (¼ in), and its depth was 2 to 3 mm (0.1 to 0.12 in). The projected crack geometry is shown in Figure 14.**

Radiographic Testing (RT)

RT was conducted in July 1996 to verify the MT indications at locations A, J, and H (June 1996 MT results). Isotope Ir-192 with 100 Curies activities was used. The detectability of the longitudinal cracks at location H was not very good. At location A, two transverse cracks were detected. On the radiograph, the visible part of the longer crack (A1) was 25 mm (1 in) long and the second crack (A2) was 10 mm (3/8 in) long. Both cracks are shown in Figure 15. In the plane of the radiographic film, the distance between the two cracks is approximately 1 mm (0.04 in). Only the longer crack was detected during MT in June 1996. The shorter crack was probably a root crack with a crack tip below the weld surface and was not detectable with MT. **This assumption was confirmed later during the metallographic and fractographic examination.**

Acoustic Emission Testing (AE)

AE monitoring for 12 hours during afternoon rush hours and one very cold night was performed on the north girder in January 1997. A prototype of a portable, wireless, six-channel AE bridge monitoring system developed cooperatively by Physical Acoustic Co., FHWA, and VTRC was used.[15] Very low crack-related AE activity was recorded on the web-to-top flange weld. The location was in the far side, similar to the locations of cores 4 and K. Twelve hours was too short a period to detect very slow and steady delayed crack growth. Continuous AE monitoring was needed.

Table 2 is a summary of the NDE results. The length of the cracks detected in the south girder was negligible compared to the length of those in the north girder.

Stress Measurements

Residual and applied stress measurements were conducted on the north girder in May through August 1996. X-ray diffraction and magnetoelastic (Barkhausen noise) residual stress measurement methods were also evaluated during this project. The preliminary results were promising for bridge applications. Table 3 gives the results for residual stresses measured using the X-ray diffraction method at midspan on the top surface of the top flange. The residual stresses were very low and are typical for welded box sections fabricated from flame-cut plates. Additional research is needed for implementation of these techniques. Currently, no methods or techniques are available to measure the residual stresses at the root of the weld. In this report, only the results from blind hole-drilling strain-gage residual stress measurements and strain-gage applied stress measurements are described in detail.

Blind Hole-Drilling Strain-Gage Residual Stress Measurements

The high-speed blind hole drilling method was used to drill a small hole near strain gages bonded to the surface of the fillet weld. As the hole is created, the surrounding surface adjusts to the removal, and this distortion is measured with strain gages. This procedure is documented in ASTM E837.

The drilling tool was the RS-200 Milling Guide with a high-speed air turbine as provided by Micro Measurements Group. A high-speed inverted cone bit with a diameter of 1.6 mm (0.062 in) was used to drill a hole no deeper than 2 mm (0.08 in). A special strain gage rosette, CEA-06-062UM-120, was used, which includes a positioning target for locating the hole. The rosette was bonded to the prepared surface with a quick-setting cyanoacrylate cement. Provided with the strain gage was a data sheet on which calibration coefficients are graphically shown as a function of hole diameter. These coefficients were used to calculate stress from the microstrain measurements. The calculation was not a conventional one because it accounted for the tangential and radial strain around a hole.[17] As in routine stress calculations, this includes the effect of stress concentration around the hole. Subsequent strain measurements were approximately one third of those normally associated with a given stress level.

A special fixture was created for this application. A mounting plate was machined so that the drilling tool could be placed over the fillet weld to drill perpendicular with the surface. The plate was at a 45° angle to the flange and web of the beam. In general, this worked sufficiently, although it required greater attention and care than standard procedures on flat surfaces. In particular, alignment was difficult because the height of the tool above the surface often exceeded the maximum focal distance of the alignment microscope. Consequently, alignment was generally performed visually from the side, and this was through limited access. The RS-

200 Milling Guide with the fixture attached to the web-to-top flange groove weld is shown in Figure 16, as are a cone bit and a rosette with three strain gages at 45° increments around the target.

Strain gages were recorded with an SES8000 Data Acquisition System and SES8_105.7 software using SES7000 signal conditioning and a Fluke Hydra data logger. The block diagram of the system is shown in Figure 17. Signal conditioning provided the channel amplification and filtering for the circuits of the Wheatstone Bridge. The data logger scanned the inputs and provided voltage readings to be converted by the software to microstrains. For each hole, the gages were zeroed by recording their initial voltage and shunt calibrated to provide a specific reading for the gage factors. This was performed by connecting a precision resistor parallel with the completion leg of the bridge circuits. Depth of penetration was recorded through a precision gage head transducer, which is a spring-loaded linear variable differential transducer (LVDT). By observing the characteristic of the measurement, drilling can be stopped at a minimum depth without completing the full 2-mm (0.08-in) depth. Additionally, the quality of the measurement was evaluated to increase the confidence of the interpretation.

Standard SES procedures were used to perform the measurements. Once the gages were operational, air was supplied at 6 MPa (40 psi) to the drill, which was then lowered until the cutters penetrated the strain gage and not the metal beneath. The gages and depth measurement were re-zeroed. Drilling proceeded in 0.02-mm (0.005-in) increments controlled manually with a threaded micrometer vernier. As the drill penetrated, the holding shaft was rotated to orbit the bit about the centerline of the shaft. This ensures a more uniform hole and reduces problems of full circumferential contact between the bit and side of the hole. Because of the offset drilling method, the hole size was slightly larger than normal. For these holes, the diameter was taken as 2.2 mm (0.085 in), which provides calibration coefficients of 0.22 and 0.59 for the "a" bar and "b" bar, respectively. A modulus of elasticity of 203 MPa (29.5 x 10^6 psi) and a Poisson's ratio of 0.29 were used for the stress calculations. Residual stress results described the principal stresses and the alignment of the maximum stress relative to the first gage of the rosette. All holes not associated with a core location were removed by grinding. All measurements were conducted outside the north (near) box girder side.

Data were recorded and digitally/graphically displayed continuously as the drilling progressed. When the strain gages were no longer sensitive to deepening the hole, drilling was stopped. This was typically at 1.5 mm (0.06 in), which is short of the standard 2 mm (0.08 in) maximum. Generally, 80 percent of the results were obtained in the first 1 mm (0.04 in)—50 percent depth of the hole. Readings were written to sequentially numbered ASCII text files and subsequently reprocessed to files for import to a spreadsheet. Residual stress was graphed for each hole as a function of depth.

Hole 1. This location was selected first to represent an ambient weld condition. It was located on the bottom flange-to-web fillet weld, 375 mm (14¾ in) from stiffener 8 toward stiffener 7. Unfortunately, the air turbine stalled at a depth of 1 mm (0.04 in) and had to be removed and replaced. The result should typically represent 80 percent of the final answer. The maximum tensile stress was 124 MPa (18,755 psi), which would scale to 162 MPa (23,444 psi) and be oriented longitudinally along the weld.

Hole 2. This was the maximum stress location, on the web-to-stiffener fillet (tee) weld of stiffener 8, 380 mm (15 in) above the flange and 38 mm (1½ in) below the longitudinal crack at core location H. The maximum tensile stress was 511 MPa (74,117 psi) in the longitudinal direction, essentially at yield of the base material. The depth of the hole was 1.4 mm (0.055 in). The plots for microstrain vs. elapsed time and stresses vs. depth are shown in Figure 18.

Hole 3. This was intended to be a second hole at the same location as hole 2, with the first hole removed, exposing a deeper layer of the fillet weld. It was aborted when high torque stalled the air turbine and loosened it from its shaft. This measurement should not be considered valid.

Hole 4. This location was near a crack on the web-to-bottom flange fillet weld between stiffeners 8 and 9. As the surface of the weld was being ground, a new crack was discovered. The measurement was approximately 19 mm (¾ in) from the new crack. The maximum tensile stress was 194 MPa (28,076 psi), approximately in the direction of the weld. The depth of the hole was 1.3 mm (0.05 in). The plots for microstrain vs. elapsed time and stresses vs. depth are shown in Figure 19.

Hole 5. At this location, the tool was difficult to position and hold in place. This location was under the top flange near the corner with cracking at location K—at 75 mm (3 in) from the crack and 114 mm (4½ in) from stiffener 9. Several problems developed, including an inactive depth sensor. The alignment was off the target, so the results were not acceptable without compensation. The maximum stress was only 42 MPa (6,069 psi) along the weld. This measurement should not be considered valid.

Hole 6. This was a repeat near hole 5, with the hole located 130 mm (5 1/8 in) from the stiffener. This time, the results were acceptable, with a maximum tensile stress of 192 MPa (27,759 psi) using the full 2-mm (0.080-in) depth. The stress was along the weld. The plots for microstrain vs. elapsed time and stresses vs. depth are shown in Figure 20.

Hole 7. This was another web-to-bottom flange fillet weld location and was placed 559 mm (22 in) from stiffener 7, toward stiffener 8, and 51 mm (2 in) beyond a known crack. The maximum tensile stress was 82 MPa (11,893 psi) along the direction of the weld, and the hole was 1.6 mm (0.065 in) deep.

Hole 8. The final location was on the bottom flange itself and not on a fillet weld. This location was 106 mm (4¼ in) from the corner of stiffener 9 toward the end and 57 mm (2¼ in) from the edge of the flange. The maximum compression stress was -87 MPa (-12,688 psi), and the minimum compression stress was -152 MPa (-22,013 psi). The minimum stress was along the length of the beam, and the maximum was along the transverse. Drilling was halted at 1.5 mm (0.06 in) to minimize the grinding required to remove the hole. The plots for microstrain vs. elapsed time and stresses vs. depth are shown in Figure 21.

The maximum residual tensile stress, 511 MPa (74,117 psi), measured in one location of the fillet weld was very near the specified minimum yield point of the weld metal, 538 MPa (78,000 psi). The typical residual stresses were lower than half the yield specified for the base metal. Contributory stresses were probably introduced by some fabrication operations and transport. However, the transport was not the primary cause of the cracking because fatigue crack enlargement was not encountered during fractographic examination of the exposed cracks.

Strain-Gage Applied Stress Measurements

Seven electrical resistance strain gages (350 ohm) were installed at the center cross section of the box girder over the pivot point at the center of the pier. This section would be expected to have the highest stress attributable to any bending of the box beam and should represent the most critical area of the girder. Figure 22 shows the location of the gages. Gages 1 through 4 were located at the corners of both the top and bottom flange plates. Gages 5 through 7 were arranged in a 45° rosette configuration at the center of the web on one side of the box girder. All gages were connected and monitored using the wireless telemetry system developed by FHWA. Figure 23 shows the strain gages on the top of the top flange (23a) and bottom flange (23b), three gages on the girder web connected to one of the remote telemetry nodes (23c), and the receiver node connected to a laptop computer to display data (23d). Live load data were collected under two conditions: (1) opening and closing of the swing span and (2) a series of "typical" trucks crossing the bridge at a normal traffic speed.

Strain Data, Bridge Opening. Before the opening process began, all of the gages were balanced to read zero strain. Data collection began after the locks were disengaged and the span started to rotate. The data show an initial strain in the gages at time $t = 0$ seconds. This strain resulted when the locks were disengaged from the girder. Data collection was continued until the buffer capacity of the data acquisition equipment was reached. Gages 1 and 2 on the top flange of the girder started out in initial tension, cycled into relative compression as the girder rotated, then went back into tension as the girder approached the fully open position. The bridge was almost fully open at time $t = 150$ seconds. At time $t = 200$ seconds, the bridge was still moving slightly but could be considered fully open.

The two top flange gages (1 and 2) showed about the same strain throughout the opening. Likewise, the two bottom flange gages (3 and 4) were similar. The top and bottom flange gages were opposite in behavior, as would be expected for primary bending of the box girder. There was no evidence of torsion or weak axis bending of the girder. Figure 24a shows the average strain in the top flange compared to the average strain in the bottom flange. The difference indicates bending in the girder. Figure 25a shows the shear strain that was resolved from the three gages at the center of the web. The measured shear strain was very low, indicating no appreciable St. Venant torsion in the box.

Strain Data, Bridge Closing. Figure 24b shows the average flange strain during closing. Data collection was initiated after the girder began to rotate and was stopped before the girder was fully closed and the locks were engaged. As would be expected, the strain during closing was a mirror image of the strain during opening. The opening data at time t = 60 seconds and t = 150 seconds corresponded approximately to the closing data at time t = 150 seconds and t = 50 seconds, respectively. The time base was slightly different between opening and closing, indicating that the speed of rotation was slightly different for the two operations. Similar to the opening data, there was no appreciable shear stress in the web, as is shown in Figure 25b.

The live load stress range in the box girder attributable to bridge opening and closing was about 41 MPa (5.9 ksi).

Strain Data, Live Load Traffic. A series of data sets was recorded for various types of trucks crossing the bridge. Only the general type of truck and a subjective guess as to whether the truck was loaded were logged for each data set. Figure 26 shows the highest strain recorded over about a 1-hour period in the midafternoon. The strain was caused by two closely spaced dump trucks traveling south in the right lane, apparently loaded. The stress range corresponding to this truck event was less than 5 MPa (0.7 ksi). Based on this result, it can be reasonably assumed that live load traffic will cause insignificant stress in the box girder, even with overloaded trucks.

It is interesting to note that the strain gages at adjacent corners were out of phase and those at opposite corners were in phase. This indicates that the strains are caused by warping torsion of the box girder, not primary bending. The 8-second shift between strain peaks is consistent with a truck moving at a normal traffic speed from one end of the swing span truss to the opposite end. This result indicates that the locking wedges under the two ends of the box girder are effective in eliminating bending of the girder under traffic loading; however, there was a slight twisting of the girder as the trucks traversed the length of the swing span. These stresses, however, were of insignificant magnitude.

Metallurgical and Failure Analysis of Cores

Chemical composition analysis, metallography macro- and microstructure analysis, macrofractography, and scanning electron microscopy (SEM) were performed in accordance with ASTM E1019-94, E415-95, E1447-92, E340-95, E1508-93a, E3-95, and E407-93. The etchant was 2 percent Nital. Microstructural identification was performed using a Leitz MM6 widefield metallographic microscope. A Jeol SEM and a Leica SEM equipped with a light element detecting energy dispersive X-ray spectrometer (EDS) were used to examine the fracture surfaces.

Seven cores 75 mm (3 in) in diameter were taken from the north and south girders. The location of the cores is shown in Figure 27. Cores 1, 2, 3, and 4 were removed in November 1995. Three additional cores—A, H, and K—were removed in July 1996. Cores 1 and 2 were taken from the south girder. Cores 3, 4, A, H, and K were taken from the north girder. Cores 2, 4, A, and K were composed of weld metal, base metal of the top flange, and base metal of the web. Cores 1, 3, and H were composed of weld metal, base metal of the web, base metal of the stiffener, and base metal of the diaphragm. A general view of the cores is given in Figure 28. Cores 1, 2, and 4 did not evidence any discontinuity prior to the extraction. Cores 3, A, and K contained MT transverse rejectable indications. Core H contained MT longitudinal rejectable indications. RT confirmed the presence of cracks in cores A, H, and K. In core A, only one crack 50 mm (2 in) long was detected. During the radiographic exposure, the gamma-ray beam was probably parallel only with this crack. The cylindrical shape of the core also reduced the probability of RT detection of the shorter crack, which can be seen on the radiograph taken before the removal of core A. Radiographs for cores A and K are shown in Figure 29.

Visual examination of the cores and macrometallography revealed that the cracks initiated either at the weld root or weld face. Figure 30a shows a root crack at the bottom side (looking to the bottom flange) of core H. Figure 30b shows the crack root, and Figure 30c the crack tip. Figure 30d at higher magnification shows the weld microstructure at the crack tip composed of acicular ferrite and tempered martensite. Figure 30e shows at lower magnification two root cracks in core 4. At the top side (looking to the top flange) of core H, a subsurface crack was visually observed. After metallographic preparation, polishing and etching, it was discovered that the crack was a root crack with a surface-breaking opening (see Figure 30f). Figures 30g and 30i show the crack root and crack tip at higher magnification. The acicular ferrite and tempered martensite weld microstructure at the crack root and crack tip is shown in Figures 30h and 30j.

The crack depth of surface-breaking cracks measured with DPT varied from microns to weld-through cracks 25 mm (1 in) deep. The crack width on the weld face varied from microns to 1 to 2 mm (0.2 to 0.5 in). Figure 31a shows a very fine crack averaging 30 μ wide on the surface of core 3. This crack was detected by MT in March 1995. Figure 31b is a photomicrograph of the tangential longitudinal section taken from this area with a suspected fracture. The microstructure is polygonal ferrite with lower bainite. A suspected slag inclusion within the fracture is shown, too. This very fine crack at the weld face probably developed at the time of fabrication, before the first painting system was applied. Attempts to separate a fracture at this location revealed surfaces extensively coated with organic matter that inhibited imaging in the electron microscopy. The crack was probably very small during the first MT inspection in the shop and was not detectable, or it may have developed after MT but before the coating was applied.

Some of the weld face cracks probably developed at later periods and are still taking place. For example, one face crack was detected on July 16, 1996, during the surface preparation for residual stress measurements on the north girder but was not detected during MT inspection on June 18, 1996. Three eddy current indications on the south girder were confirmed visually to be fine cracks during the grinding process on August 14, 1996.

Some cracks at the weld root probably developed at the time of fabrication and grew very slowly. SEM examination of the exposed fracture surface of the root crack A1 (approximately 25 mm [1 in] long) at core A revealed features that were obscured by surface oxidation (see Figure 32a). The heavy rusting indicated that the crack had been present for a long time.

Macrofractographic examination revealed a transverse crack approximately 25 mm (1 in) long and approximately 25 mm (1 in) deep. **An additional metallographic sectioning of the same core revealed the root crack A2 propagating about 2 to 3 mm (0.1 to 0.12 in) in the base metal of the top flange (see Figure 32b).** The projected crack path is shown in Figure 32c. The microstructure at the crack tip shown in Figure 32d is acicular ferrite and tempered martensite.

Some of the root cracks probably developed at later periods (months after the welding operation). SEM examination of the exposed fracture surface of the transverse crack at core K (Figure 33a) primarily revealed features characteristic of ductile tensile overload (Figure 33b). An underlying intergranular appearance (possible hydrogen-induced cracking) was observed in area 1 (Figure 33c). Evidence of clean, intergranular facets indicative of hydrogen-induced cracking was noted in the region near the external exposed surface of the crack (Figure 33d).

Fractographic examination indicated that the cracks removed from the north pivot box girder were delayed cracks. All of the evaluated cracks appear to have resulted from hydrogen-related cold cracking. The fracture was of either the intergranular or transgranular quasi-cleavage type. Intergranular and transgranular quasi-cleavage is typical in hydrogen-induced cracking. Ductile tearing was also present in the exposed fracture surface of core H (see Figures 34a and b). Fracture features typical of quench cracking were observed in the exposed fracture surface of core A (see Figures 34c and d). No evidence of crack propagation beyond the weld metal into the base metal was observed on the exposed crack surfaces of cores A, H, and K, and no fatigue crack extension was observed.

Generally, very strong evidence for crack initiation and growth at later periods is provided by the 144 cracks detected during the MT inspection in March 1995 that were undetected during the previous shop inspection in January 1995; the 47 cracks detected during the MT inspection in June 1996 that were undetected during the previous inspection in March 1995; and the 24 cracks detected during the MT inspection in April 1997 that were undetected during the previous inspection in June 1996. The crack growth rates were estimated as follows. For the crack at location K detected during the MT inspection in June 1996, if the crack initiated as a root crack immediately after the welding in January 1995 and grew to reach the depth of 25 mm and the face of the weld in June 1996 (17 months), the crack growth rate would be approximately 1.5 mm/month (0.06 in/month). To reach a length of 51 mm (2 in) on the surface, the crack growth rate would be approximately 3 mm/month (0.12 in/month). For the crack at location T detected during the MT inspection in April 1997, two points are important:

1. If the crack initiated as a surface-breaking crack immediately after the MT inspection in June 1996 and reached the depth of 19 mm (¾ in) by April 1997 (10 months), the crack growth rate would be approximately 2 mm/month (0.05 in/month). To reach a length of 51 mm (2 in) on the surface, the crack growth rate would be approximately 5 mm/month (0.1 in/month).

2. If the crack initiated as a root crack immediately after the welding in January 1995 and reached the depth of 19 mm (¾ in) and the face of the weld in April 1997 (28

months), the crack growth rate would be approximately 0.7 mm/month (0.03 in/month).

The maximum depth crack growth rate was probably approximately 1.5 mm/month (0.06 in/month), and the length rate approximately 5 mm/month (0.1 in/month).

An increase in the size of the root gap higher than 0.5 mm (0.002 in) was observed in two cores taken from the north girder (see Figures 30a and e). This could possibly raise the stress imposed on the weld and could cause root cracking even when the hydrogen level was low and welding conditions were held constant.[8] The Bridge Welding Code allows a root opening of 5 mm (3/16 in).[10]

Very small inclusions (10 to 100 μ), most likely aluminum, silicon, or manganese sulfides, were observed in the fracture surfaces of the specimens taken from the north girder. Figures 35a and b show the inclusions in the weld metal of core 4, and Figures 35c and d show inclusions in the base metal of core A. These inclusions, in the presence of existing stress, may develop high local areas of tensile stresses and may serve as crack initiation or continuation sites. The latest model of hydrogen-induced cracking initiated at preexisting small defects is consistent with the relatively slow and discontinuous nature of the cracking process in this case.

The microstructure of the base metal plates (top flange, web, and stiffener) is typical for quenched and tempered C-Mn low-alloy high-strength steels (see Figure 36). The microstructure of the weld metal, fusion zone, and HAZ for cores 2, 3, 4, A, H, and K is shown in Figure 37. The microstructure of the weld metal in the north and south girder was predominantly columnar with acicular ferrite, grain boundary ferrite (widmanstatten), and areas of lower bainite and tempered martensite. A microstructure with components of grain boundary ferrite (widmanstatten) and areas of lower bainite and tempered martensite is more susceptible to hydrogen-induced cracking than a microstructure with acicular ferrite. An intergranular fracture bound by polygonal ferrite grains and tempered martensite of the fusion zone of the web on the side and the HAZ, a fusion zone, and weld metal of the vertical stiffener in the north girder was observed (see Figure 38). There was no significant microstructural difference between the weld metal in the north and south girders. Table 4 summarizes the grain size determinations in the base metal and HAZ in each core and in the welds of cores 2, 3, and 4. The coarse grain structure is typical for HAZ.

The base and weld materials were in accordance with the chemical compositional requirements specified in the ASTM and AWS standards. Table 5 summarizes the chemical analysis and carbon equivalent calculated in accordance with the Bridge Welding Code.[10]

The hydrogen content measurements performed by at least three independent laboratories are given in Table 6. The residual hydrogen content was analyzed by the inert gas fusion method using a Leco RH-404 hydrogen analyzer. The accuracy of the instruments is ±0.2 ppm. The hydrogen content measured in the north girder was 1.4 to 6 ppm for the top flange-to-web groove weld; 0.06 to 6 ppm for the web-to-stiffener fillet weld; 0.9 to 7 ppm for the top flange base metal; 1.08 to 6 ppm for the web base metal; and 5 to 7 ppm for the stiffener base metal. The hydrogen content measured in the south girder was 1.1 to 1.4 ppm for the top flange-to-web groove weld; 1.56 to 2.78 ppm for the web-to-stiffener fillet weld; 1.64 to 1.79 ppm for the web-to-diaphragm fillet weld; 2 to 3.1 ppm for the top flange base metal; and 1.9 ppm for the stiffener base metal. The hydrogen content of the consumables reported by Lincoln Electric Co. was within the AASHTO limit of 8.9 ml/g (10 ppm). A relatively high hydrogen content was measured in the north girder's flange, web, and stiffener base metal and the weld metal of the web-to-top flange weld.

Mechanical Testing of Cores

Impact testing, tensile testing, fracture testing, and hardness testing were performed in accordance with ASTM E23-96, E8-96, E399-90, E384-89, and E18-94. The specimens for mechanical and fracture testing were parallel with the top flange rolling direction and the weld length. The locations of test specimens fabricated (extracted) from different cores are shown in Figure 39.

Test results from tensile tests are given in Table 7. The flange base metal in two tensile specimens fabricated from core K in the north girder did not meet ASTM's yield and tensile strength requirements. An additional mechanical test for the base metal at this location showed that this was probably only scattering in the tensile properties of the base metal. If necessary, a new core close to core K could be taken for additional tension verification tests.

The CVN test results for different temperatures are given in Table 8. Broken CVN samples from cores 2, 4, K, A, and H are shown in Figure 40. The value of 200 J (148 ft-lb) for the absorbed impact energy at -7° C (20° F) for the flange plate material was well above the ASSHTO Zone 2 requirement of 48 J (35 ft-lb). The web impact toughness was 176 J (130 ft-lb) at -23° C (-10° F). The ASSHTO Zone 2 requirement for the web plate is 41 J (30 ft-lb) at -7° C (20° F).

One L-T orientation CVN specimen machined from the north girder flange-web weld material indicated high toughness at -18° C (0° F): 109 J (81 ft-lb). Two additional specimens from the HAZ indicated higher toughness: 123 and 112 J (91 and 83 ft-lb) at the same temperature. The average absorbed energy for these three specimens was 115 J (85 ft-lb). One L-T orientation CVN specimen machined from the north girder web-to-stiffener weld material indicated a toughness of 76 J (56 ft-lb) at -23° C (-10° F). Two L-T orientation CVN specimens machined from the south girder flange-web weld material indicated a lower toughness at -18° C (0° F): 90 and 62 J (67 and 46 ft-lb), an average of 76 J (56 ft-lb). For qualifying the welding procedures, the ASSHTO requirement for the CVN for weld metal connecting ASTM A709 Gr. 70W steel is 41 J (30 ft-lb) at -31.7° C (-25° F).

The weld material was much harder than either the flange or the web and probably has a higher tensile strength. Based on conversion tables, the tensile strength for the welds in the north and south girders was in the range of 773 to 904 MPa (112 to 131 ksi) and for the base metal was in the range of 621 to 704 MPa (90 to 102 ksi). The weld metal with higher strength probably has reduced ductility. The results from the macro- and microhardness measurements across the welds in each core are given in Table 9. Rockwell hardness measurements were performed on the polished cross-sectional surfaces using a 1.6-mm (1/16-in) ball indenter with a 100-kg load for Scale B measurements and a Brale indenter with a 150-kg load for Scale C measurements. Knoop microhardness was measured with a load of 300 and 500 g at 400x magnification. Vickers microhardness was measured with a load of 1000 g at 400x magnification. The maximum value measured in the weld fusion zone of core 3 was 311 HV, and in the weld of core 4 was 302 HV.

A total of 780 Vickers hardness tests (5 per location) were conducted along the welds on both girders in the field: 74 test locations were on the south girder, and 82 were on the north girder. No significant difference in the hardness along the welds and between two girders was noticed. The maximum value measured in the north girder was 307 HV, and in the south girder was 301 HV.

Fracture Analysis

Brittle Fracture Potential

Calculations were performed to estimate the potential for brittle fracture initiating from the existing crack in the top flange-to-web weld. Initial assumptions for crack size were based on the largest transverse crack found to date in the structure using NDE and were confirmed using destructive methods. Very good examples are the five transverse cracks detected by MT and visually observed in the midspan location F1 during the March 1995 inspection (Figure 5), the cracks in cores A and K (Figures 6, 15, 27, 32, and 33), and the crack in location T (Figures 7 and 14).

No exact solution for a stress intensity factor exists for cracks in a partial penetration groove weld connecting the flange and web of a box girder. However, a crack can be conservatively approximated as a semielliptical crack in the surface of a plate.[18] It is also conservatively assumed that the stress at the crack tip is at yield attributable to the combination of the dead load on the structure and residual stresses caused by the welding.

No data were available for the actual yield strength in the weld. For this calculation, the specified minimum yield strength of 538 MPa (78 ksi) in the weld material, a conservative measure, was used to predict the yield strength in the weld. Because the actual yield strength is almost always higher than the specified yield strength for most weld materials, it was assumed that the average yield strength in the weld was 552 MPa (80 ksi). There is no guarantee that this value represents the average yield strength in the weld metal.

Weld material toughness was estimated based on CVN test results. The lowest test value of CVN = 62 J (46 ft-lb) measured for the south girder was used for the fracture analysis. It is very well known that the toughness of welds and thick base metals is highly variable. This fact was confirmed by the scatter in the CVN test results in this study. It was assumed that local areas with low toughness as measured in the south girder probably exist in the north girder groove weld, too. There is no guarantee that this value represents the lowest toughness in the weld.

The critical stress intensity factor K_{Ic} is a function of temperature and can only be estimated from the CVN tests. Using the Barsom-Rolfe two-step correlation,[19] CVN = 46 ft-lb at -32° C (0° F) correlates to $K_{Ic} = 91$ MPa $\cdot$ m$^{1/2}$ (82.7 ksi-in$^{1/2}$) at -70° C (-95° F). This value needs to be adjusted to the lowest anticipated service temperature (LAST) of -34° C (-30° F) for AASHTO zone II to obtain the worst case for fracture at the bridge site. Without further information, this adjustment can only be estimated. Figure A2 (see the Appendix) shows a CVN transition curve for A852 steel that was developed for a previous test program at FHWA.[20] This curve indicates that the upper shelf toughness is about 102 J (75 ft-lb) for this steel. Assuming this is similar to the steel in the Coleman Bridge, this would indicate that a CVN toughness of 102 J (75 ft-lb) would be expected at -34° C (-30° F).

Based on these assumptions, the results shown in the Appendix indicated that the partial penetration groove weld in the box girder could develop a brittle fracture. This does not, however, mean that a fracture will definitely occur. The assumptions used for this analysis were conservative and should produce a conservative answer. The calculations were also based on crack initiation in the weld, where a high residual stress typically exists.

No calculations were performed to estimate the potential for brittle fracture from the existing crack in the top flange base material. Cracks with a length and depth more than 2 to 3 mm are detectable with NDE methods. Any cracks should be detected during the proposed frequent NDE inspection, and quick actions should be taken to prevent their growth. If necessary, the maximum length and depth of the transverse cracks in the base metal of the top flange that could be tolerated could be calculated in a separate project.

Fatigue Potential

The strain gage data showed that there will be one primary stress cycle on the box girder each time the stress cycles for each bridge opening-closing sequence. The highest recorded stress was 41 MPa (5.87 ksi) at the top flange strain gages. The strain plots in Figure 25 show the live load strain reversal from tension to compression during the opening cycle. The dead load stress state is unknown. It can be assumed that when the dead load is superimposed with the live load that the top and bottom flanges will always be in tension and compression, respectively. Therefore, the entire live load stress cycle is assumed to contribute to fatigue. Live load stress cycles caused by vehicular traffic are insignificant and can be ignored.

Calculations of the potential for fatigue crack growth for existing cracks are shown in the Appendix. Based on the measured stress range, it will take 386,000 bridge openings to cause a crack to grow 25 mm (1 in) larger. If the bridge is opened an average of once a day, it will take more than 1,000 years for this to occur. Closing will cause a second primary stress cycle, resulting in two primary cycles for the structure. Therefore, it can be concluded that fatigue is not a serious concern for bridge opening.

CONCLUSIONS

- Through the use of different NDE methods, more than 200 transverse and longitudinal cracks were discovered in the north girder (fabricator, Vincennes Steel, Vincennes, Indiana) and 7 cracks were discovered in the south girder (fabricator, Stupp Brothers Bridge and Iron Co., St. Louis, Missouri).

- The tests in June-October 1996 and April 1997 showed that delayed crack initiation and propagation are still taking place.

- The possibility of unique, rare, and very long-term delayed cracking (cold or hydrogen-induced cracking) is supported by the results of the hydrogen content analysis, residual stress measurements, and macro- and microstructure metallography and fractography.

- There is strong evidence that a susceptibility to hydrogen-induced cracking of the weld metal in the north girder developed during fabrication. Cracking occurred as a result of the combination of this susceptibility, the presence of hydrogen in the weld and base metal, and residual stresses.

- The great number of cracks detected in the welds of the north girder, coupled with the very long total crack length, shows that these welds have been and still are inordinately susceptible to cold cracking.

- Calculations show that the partial penetration groove weld could develop a brittle fracture under the worst conditions, but this occurrence is not likely.

- Calculations show that there is little probability that the cracks will extend in any significant amount because of fatigue during the life of the bridge.

RECOMMENDATIONS

- Inspect the north box girder through MT or ET a minimum of every 6 months during the next 3 years, and repair cracks quickly when found.

- To allow better inspections, do not paint the north box girder.

- Consider the use of a special UT examination technique (phase array or time-of-flight diffraction) and AE monitoring for better detectability of buried root weld cracks propagating in the top flange base metal in the north girder.

ACKNOWLEDGMENTS

The authors thank H. A. Perry, A. W. Nickel, and B. Mayton of VDOT's Materials Division and R. Nelson, P. A. Fuchs, F. Beshah, D. Lamtenzan, D. Richards, and N. Shashidhar of the FHWA for their cooperation and assistance. We thank L. Suominen of AST; R. Boswell of Stress Engineering Services; A. Casler of Aston Metallurgical Services; A. M. Phelps of Sherry Laboratories; and C. Apusen, J. French, D. Alpern, and D. S. Lane of VTRC for their technical support. We thank R. Combs and E. Deasy of VTRC for their great assistance with the graphics and photographs. Thanks are also due to C. S. Napier, Jr., of FHWA; M. J. Abrahams of Parsons, Brinckerhoff, Quade & Douglas, Inc.; G. M. Clendenin, H. A. Perry, and A. W. Nickel of VDOT; and G. R. Allen, M. M. Sprinkel, and P. Massarelli of VTRC for carefully reviewing the work and suggesting improvements. L. Evans edited the report.

REFERENCES

1. Virginia Department of Transportation. 1995. Request for Metallurgical Analysis. Richmond.

2. Roney, V. J. 1997. Extensive Pre-Assembly Radically Cuts Time. *Modern Steel Construction,* No. 2, pp. 28-34.

3. Johnsen, M. R. 1996. An Engineering First Bridges the York River. *Welding Journal,* No. 11, pp. 29-32.

4. Barsom, J. M. 1991. Properties of Bridge Steels. *Highway Structures Design Handbook,* Vol. I, Chap. 3.

5. Miller, D. K. 1991. Welding of Steel Bridges. *Highway Structures Design Handbook,* Vol. I, Chap. 10B.

6. Perry, H. A., Nickel, A. W, and Mayton, B. 1996-1997. Business communications.

7. Lozev, M. G., and Christov, S. 1991. Acoustic Emission Monitoring of Cold Cracks in Low-Alloy Steels. *Proceedings of the First Advanced Engineering Materials Fracture Conference.*

8. Bailey, N., Coe, F. R., Gooch, T. G., Hart, P. H. M., Jenkins, N., and Pargeter, R. J. 1993. *Welding Steels without Hydrogen Cracking.* Abington Publishing, Cambridge, U.K.

9. Cieslak, M. J. 1993. Cracking Phenomena Associated with Welding. *ASM Handbook,* Vol. 6, pp. 88-96. ASM International, Materials Park, Oh.

10. *Bridge Welding Code.* 1988. ANSI/AASHTO/AWS D1.5-88. American Association of State Highway and Transportation Officials, Washington, D.C., and American Welding Society, Miami.

11. American Association of State Highway and Transportation Officials. 1991. *Guide Specifications for Fracture Critical Non-Redundant Steel Bridge Members.* Washington, D.C.

12. Jones, W. F. 1993. Hydrogen-Induced Cracking of Welded Truss Gusset Plates. *Handbook of Case Histories in Failure Analysis.* ASM International, Materials Park, Oh.

13. Fisher, J. W., Kaufmann, E. J., Koob, M. J., and White, G. 1995. Cracking, Fracture Assessment, and Repairs of Green River Bridge, I-26. *Proceedings of the Fourth International Bridge Engineering Conference.*

14. Lozev, M. 1996. *Noncontact Nondestructive Detection and Evaluation of Fatigue Cracks in Steel Bridge Members.* VTRC 96-RP 16. Virginia Transportation Research Council, Charlottesville.

15. Lamtenzan, D., Washer, G., and Lozev, M. G. 1997. *Detection of Cracks in Steel Bridges Using Eddy Current.* The American Society for Nondestructive Testing, Columbus, Oh.

16. Lozev, M. G. 1995. *Testing and Evaluation of a Prototype Portable Acoustic Emission Bridge Monitoring System.* VTRC 95-RP14. Virginia Transportation Research Council, Charlottesville.

17. Boswell, R. S., and Kim, D. S. 1996. *Residual Stress Measurement Results in Refinery Vessels.* PVP, Montreal, Canada.

18. Newman, J. C., and Raju, I. S. 1981. *Stress Intensity Factor Equations for Cracks in Three-Dimensional Finite Bodies.* NASA Technical Memorandum 83200.

19. Barsom, J. M., and Rolfe, S. T. 1987. *Fracture and Fatigue Control in Structures,* 2nd ed., Prentice Hall, 1987.

20. Wright, W. J., and Albrecht, P. 1991. Fatigue Crack Growth Rates in Bridge Steels. *Proceedings of the TRB Third Bridge Engineering Conference.* Transportation Research Board, Washington, D.C.

APPENDIX

FRACTURE MECHANICS ANALYSIS

Stress Intensity Factor for Typical Crack

No exact solutions exist for transverse cracks in the web-to-flange partial penetration groove welds observed in the bridge. This crack can be conservatively approximated as a semi-elliptical surface crack in a finite width plate under tension.[18] The web will provide added restraint to crack opening that is not considered in this analysis. The following results will be conservative.

Crack dimensions are in accordance with Figure A1, and approximations are based on:

- depth of crack, b = 25.4 mm (1.0 in)
- ½ the surface length of crack, a = 25.4 mm (1.0 in)
- thickness of tension flange, t = 76.2 mm (3.0 in)
- width of flange overhanging the web, w = 203.2 mm (8.0 in)
- ½ length of top flange (essentially infinite), h = 6.12 m (249.0 in)
- location around crack profile, $\Phi = 0$ degrees.

$$\frac{b}{a} = 1$$

$$M_1 = 1.13 - 0.09 \cdot \left(\frac{b}{a}\right) \qquad M_1 = 1.04$$

$$M_2 = -0.54 + \frac{0.89}{0.2 + \left(\frac{b}{a}\right)} \qquad M_2 = 0.202$$

$$M_3 = 0.5 - \frac{1}{0.65 + \left(\frac{b}{a}\right)} + 14 \cdot \left(1 - \frac{b}{a}\right)^{24} \qquad M_3 = -0.106$$

$$g(b) = 1 + \left[0.1 + 0.35 \cdot \left(\frac{b}{t}\right)^2\right] \cdot (1 - \sin(\Phi))^2 \qquad g(b) = 1.139$$

$$f_\Phi = \left[\left(\frac{b}{a}\right)^2 \cdot \cos(\Phi)^2 + \sin(\Phi)^2\right]^{\frac{1}{4}} \qquad f_\Phi = 1$$

$$f_W(b) = \sec\left(\frac{\pi \cdot a}{2 \cdot W}\sqrt{\frac{b}{t}}\right)^{\frac{1}{2}} \qquad f_W(b) = 1.003$$

$$F_s(b) = [M_1 + M_2 \cdot (\frac{b}{t})^2 + M_3 \cdot (\frac{b}{t})^4] \cdot g(b) \cdot f_\Phi \cdot f_W(b) \qquad F_s(b) = 1.212$$

$$E_k = [1 + 1.464 \cdot (\frac{b}{a})^{1.65}]^{\frac{1}{2}} \qquad E_k = 1.57$$

$$\frac{F_s(b)}{E_k} = 0.77$$

$$K_I(\sigma,b) = \sigma \frac{\sqrt{\pi \cdot b}}{E_k} \cdot F_s(b)$$ *Stress intensity factor caused by applied loading.*

Note: These equations are valid only for $b/a \le 1$. Different equations are required for $b/a > 1$.

Fracture Potential

For fracture, the conservative assumption is that the stress at the crack tip is equal to the yield stress. Research has shown that residual stresses can reach this magnitude locally at weldments.

$\sigma = 552$ MPa (80 ksi) *Assumed actual yield stress.*

$K_I(\sigma,b) = 120$ MPa $\cdot$ $m^{1/2}$ (109 ksi-$in^{1/2}$) *Stress intensity at crack due to dead load and residual stress.*

CVN = 62 J (46 ft-lb) *Lowest toughness measured in weld and HAZ.*

$T = -18°$ C (0° F)

The two-stage Barsom-Rolfe correlation[19] gives:

$T_{shift} = 215 - 1.5\sigma$ (valid for temperature in °F and stress in ksi) $\qquad T_{shift} = 35°$ C (95° F)

$$K_{Id} = \sqrt{5 \cdot CVN \cdot 30000000} \cdot \left(\frac{1}{1000}\right) \qquad K_{Id} = 91 \text{ MPa} \cdot m^{1/2} \text{ (83 ksi-in}^{1/2})$$

$K_{Ic} = K_{Id}$ at $T_{static} = T - T_{shift}$ $\quad T_{static} = -70°$ C (−95° F)

The extreme temperature for AASHTO zone II is −34° C (−30° F). This temperature is 36° C (65° F) higher than the temperature where material toughness can be estimated. The toughness at −34° C (−30° F) will be higher than that calculated above.

Data collected by Wright and Albrecht for A852 steel show an upper shelf toughness of about 102 J (75 ft-lb).[20] (See Figure A2.) Starting at the temperature where CVN = 62 J (46 ft-lb), if we shift the temperature +36° C (+65° F) to the right, the data show that the toughness will be on the upper shelf. Therefore, it is reasonable to assume CVN = 102 J (75 ft-lb) at −34° C (−30° F).

CVN = 102 J (75 ft-lb) *Assumed material resistance.*

$K_{Id} = \sqrt{5 \cdot CVN \cdot 30000000} \cdot \left(\frac{1}{1000}\right)$ $\quad K_{Id} = 116\ \text{MPa} \cdot \text{m}^{½}$ (106 ksi-in^{½})

$K_{Ic} = K_{Id}$

$FS = \frac{K_{Ic}}{K_I(\sigma, b)}$ $\quad$ FS = 0.968 *Factor of safety against brittle fracture.*

This analysis indicates that brittle fracture is a possibility if temperatures approaching the lower bound for zone II occur.

Fatigue Potential

$\Delta\sigma$ = 41 MPa (5.87 ksi*)* *Maximum measured stress range during bridge opening. Stress range due to traffic loading is insignificant. Two stress cycles of this magnitude occur each opening.*

$\Delta K_{eff} = K_I(\Delta\sigma, b)$

$\Delta K_{eff} = 8.8\ \text{MPa} \cdot \text{m}^{½}$ (8 ksi-in^{½}) *Stress intensity factor range.*

The fatigue crack growth rate threshold is about 4.4 MPa · m^{½} (4 ksi-in^{½}) for this steel. Therefore, some fatigue crack growth will be expected attributable to opening and closing of the bridge.

$da/dN = 3.75 \cdot 10^{-10} \cdot \Delta K_{eff}^{\,3.528}$ *Fatigue crack growth rate measured for A572, A588, and A852 structural steel under a high dead load.*[20]

$$N = \int_{b}^{b+1} \frac{1}{3.75 \cdot 10^{-10} \cdot K_I(\Delta[\ ,A)^{3.528}}\, dA$$ *Rearranging and integrating.*

$N = 7.717 \cdot 10^{5}$ *Number of cycles required to grow the crack 2.54 cm (1 in).*

$N_o = 2$ $N_o = 3.859 \cdot 10^5$ *Number of bridge openings required to produce 25.4 mm (1 in) of fatigue crack growth from existing defects.*

$N_y = 365$ $N_y = 1.057 \cdot 10^3$ *Years to obtain 25.4 mm (1 in) of crack growth, assuming one opening per day.*

The stress intensity factor range attributable to bridge opening is 8.8 MPa $\cdot$ $m^{1/2}$ (8 ksi-$in^{1/2}$). The threshold for fatigue crack growth is about 4.4 MPa $\cdot$ $m^{1/2}$ (4 ksi-$in^{1/2}$). Therefore, fatigue crack growth is possible but will be extremely slow. Assuming one bridge opening per day, it will take more than 1,000 years to grow the crack 25 mm (1 in) long.

TABLES

Table 1. Summary of ET Results

Crack Indication No.	Direction	Location in Weld	Position on South Girder
1	Longitudinal	Toe	In S-1 to north web weld, 3251 mm down from top flange
2	Longitudinal	Toe	In S-2 to north web weld, 654 mm up from bottom flange
3	Longitudinal	Toe	In S-2 to north web weld, 990 mm up from bottom flange
4	Longitudinal	Toe	In S-2 to north web weld, 1270 mm down from top flange
5	Longitudinal	Toe	In S-7 to north web weld, 419 mm down from top flange
6	Longitudinal	Toe	In S-8 to north web weld, 978 mm down from top flange
7	Longitudinal	Toe	In S-8 to bottom flange weld, 241 mm out from north web
8	Longitudinal	Toe	In S-8 to bottom flange weld,152 mm out from north web
9	Longitudinal	Toe	In S-8 to bottom flange weld, 140 mm out from north web
10	Transverse	Crown	In S-8 to south web weld, 140 mm up from bottom flange
11	Longitudinal	In web	In south web between S-7 and S-3, 13 mm up from bottom flange
12	Longitudinal	Toe	In S-7 to south web weld, 89 mm down from top flange
13	Longitudinal	Toe	In bottom flange to north web weld between D-1 and D-2, 267 mm from D-2
14	Longitudinal	Toe	In D-2 to north web weld, 883 mm down from top flange
15	Longitudinal	Toe	In D-3 to bottom flange weld, 476 mm in from north web
16	Longitudinal	Toe	In D-4 to south web weld, 1499 mm up from bottom flange
17	Longitudinal	Toe	In D-4 to north web weld, 2006 mm up from bottom flange
18	Longitudinal	Crown	In D-5 to south web weld, 152 mm up from bottom flange

S = stiffener, D = diaphragm.

Table 2. Summary of NDE Inspection

March–October 1995

WELDS	Weld Length (m)	Total Cracks				Transverse Cracks				Longitudinal Cracks			
		North Girder		South Girder		North Girder		South Girder		North Girder		South Girder	
		Length (m)	%	Length (m)	%	Length (m)	%	Length (m)	%	Length (m)	%	Length (m)	%
Web-to-Top Flange	24.400	6.660	27.500	/	/	2.850	11.900	/	/	3.810	15.570	/	/
Web-to-Bottom Flange	48.800	14.060	28.900	/	/	6.200	12.700	/	/	7.860	16.180	/	/
Web & Flange-to Stiffeners & Diaphragms	137.700	92.18	66.900	0.050	0.040	9.700	7.000	0.025	0.020	82.480	59.900	0.025	0.020
Total	210.900	113.000	53.600	0.050	0.040	18.900	8.900	0.025	0.020	94.200	44.660	0.025	0.020

June-August 1996

WELDS	Weld Length (m)	Total Cracks				Transverse Cracks				Longitudinal Cracks			
		North Girder		South Girder		North Girder		South Girder		North Girder		South Girder	
		Length (m)	%	Length (m)	%	Length (m)	%	Length (m)	%	Length (m)	%	Length (m)	%
Web-to-Top Flange	24.400	8.100	33.000	/	/	2.200	9.000	/	/	6.000	25.000	/	/
Web-to-Bottom Flange	48.800	1.900	3.900	0.006	0.010	0.500	1.000	0.006	0.010	0.900	1.800	/	/
Web & Flange-to Stiffeners & Diaphragms	137.700	5.500	4.000	0.012	0.009	2.500	1.800	0.006	/	3.000	2.200	0.012	0.009
Total	210.900	15.500	7.300	0.018	0.009	5.200	2.500	0.006	0.010	9.900	4.700	0.012	0.009

April 1977

WELDS	Weld Length (m)	Total Cracks				Transverse Cracks				Longitudinal Cracks			
		North Girder		South Girder		North Girder		South Girder		North Girder		South Girder	
		Length (m)	%	Length (m)	%	Length (m)	%	Length (m)	%	Length (m)	%	Length (m)	%
Web-to-Top Flange	24.40	0.38	1.60	/	/	0.38	1.60	/	0.00	0.00	0.00	/	/
Web-to-Bottom Flange	48.80	3.79	7.80	/	/	1.06	2.20	/	2.73	5.50	1.10	/	/
Web & Flange-to Stiffeners & Diaphragms	137.70	1.35	1.00	/	/	1.35	1.00		0.00	0.00	0.00	/	/
Total	210.90	5.60	10.40	/	/	2.90	4.80	/	2.70	5.50	1.10	/	/

% (crack length/weld length x 100).

Table 3. Top Flange, Top Surface, and X-Ray Residual Stress Measurements at Midspan (MPa)

Measurement Point	Longitudinal Direction	Transverse Direction
1	47.9 ± 18.1	-
2	32.1 ± 11.5	25.1 ± 11.3
3	18.5 ± 0.0	48.9 ± 7.5
4	12.4 ± 0.0	-1.1 ± 6.8
5	39 ± 9.8	53.7 ± 7.7
6	4.9 ± 11.4	6.2 ± 8
7	31.1 ± 14.2	25.6 ± 16.7
8	24.4 ± 7.2	-9.7 ± 10.3
9	11.3 ± 10.6	17.7 ± 9.8
10	60.6 ± 15	-8.3 ± 5.5
11	98.5 ± 12.1	-

Points 1 and 11 are 127 mm (5 in) from the edge. The step point is 127 mm (5 in).

Table 4. Average Grain Size Summary, ASTM Grain Size No. G

Core, Girder	Base Metal-Flange	Base Metal-Web	Base Metal-Stiffener	HAZ-1	Weld	HAZ-2
Core 3, North Girder	-	10, 10, 10	-	11, 11, 12	8.4, 9, 10	-
Core 4, North Girder	8, 10	-	-	6, 6, 6	8, 8.4	-
Core A, North Girder	10	10	-	5-10	-	3-10
Core H, North Girder	-	10	10	4-10	-	3-10
Core K, North Girder	10	10	-	4-10	-	4-10
Core 1, South Girder	-	-	-	-	-	-
Core 2, South Girder	9	-	-	5, 5, 8	8.4, 8.4, 8.4	-

Table 5a. Weld Metal Chemical Composition (%)

	North Girder						South Girder				AWS A5.23
Element	Core 3		Core 4	Core A	Core H	Core K	Core 1			Core 2	
	Outside Weld 1	Outside Weld 2	Weld 1	Weld 1	Weld 1	Weld 1	Outside Weld 1	Outside Weld 2	Inside Weld 1	Weld 1	
Carbon	0.08	0.1	0.07	0.06	0.07	0.05	0.08	0.09	0.07	0.05, 0.06	0.10 max
Manganese	1.35	1.54	1.49	1.65	1.23	1.52	1.23	1.32	1.04	1.37, 1.40	0.90-1.80
Phosphorus	0.014	0.017	0.014	0.009	0.017	0.015	0.017	0.015	0.011	0.011, 0.016	0.030 max
Sulfur	0.008	0.006	0.006	<0.005	0.009	<0.005	0.012	0.01	0.014	0.007, 0.009	0.04 max
Silicon	0.4	0.046	0.39	0.49	0.35	0.43	0.36	0.41	0.24	0.37, 0.43	0.80 max
Nickel	1.25	1.41	1.65	1.49	1.69	1.5	1.36	0.94	1.47	1.29, 1.55	1.40-2.10
Chromium	0.21	0.19	0.08	0.12	0.14	0.1	0.16	0.38	0.09	0.11, 0.23	0.35 max
Molybdenum	0.25	0.34	0.38	0.36	0.28	0.36	0.29	0.19	0.31	0.30, 0.35	0.25-0.65
Copper	0.15	0.02	0.11	0.19	0.2	0.2	0.07	0.21	0.02	0.12, 0.15	0.30 max
Vanadium	0.02	0.02	0.009	0.01	0.01	0.01	0.015	0.033	0.009	0.011, 0.019	-
Titanium	0.01	<0.01	<0.005	-	<0.01	-	0.008	<0.005	0.005	<0.005	0.03 max
Aluminum	0.01	0.02	0.005	0.018	<0.008	0.015	0.005	0.021	<0.005	0.008, 0.018	-
Zirconium	<0.01	<0.01	0.007	-	<0.01	-	0.006	0.005	<0.005	<0.005, 0.007	-
CE	0.56	0.57	0.59	0.63	0.55	0.58	0.53	0.58	0.46	0.52, 0.60	

CE = C + (Mn + Si)/6 + (Cr + Mo + V)/5 + (Ni + Cu)/15.

Table 5b. Base Metal Chemical Composition (%)

	North Girder										South Girder		A852/A852A
Element	**Core 3**		**Core 4**		**Core A**		**Core H**		**Core K**		**Core 1**	**Core 2**	
	Web	**Stiffener**	**Web**	**Flange**	**Web**	**Flange**	**Web**	**Stiffener**	**Web**	**Flange**	**Stiffener**	**Flange**	
Carbon	0.14, 0.15	0.16	0.16	0.15, 0.16	0.16	0.16	0.12	0.16	0.1	0.14	0.14	0.14	0.19 max
Manganese	1.05, 1.11	1.1	0.94	1.01, 1.08	0.99	0.99	1.05	1.09	1.04	1.04	0.98	0.99	0.80-1.35
Phosphorus	0.022, 0.023	0.016	0.021	0.019, 0.021	0.015	0.015	0.022	0.014	0.018	0.014	0.012	0.014	0.035 max
Sulfur	0.006, 0.011	0.014	0.014	0.01, 0.013	0.09	0.08	0.008	0.012	0.005	0.008	0.011	0.011	0.04 max
Silicon	0.46, 0.48	0.49	0.37	0.43, 0.5	0.35	0.35	0.4	0.33	0.4	0.36	0.36	0.32	0.20-0.65
Nickel	0.18, 0.21	0.18	0.19	0.19, 0.2	0.29	0.29	0.3	0.32	0.29	0.31	0.31	0.28	0.50 max
Chromium	0.57	0.6	0.51	0.5, 0.54	0.54	0.54	0.6	0.58	0.6	0.53	0.54	0.5	0.40-0.70
Molybdenum	0.05	0.05	0.01	0.01	0.05	0.05	0.05	0.05	0.05	0.05	0.01	0.01	-
Copper	0.28, 0.3	0.31	0.28	0.28, 0.27	0.29	0.29	0.3	0.2	0.22	0.31	0.28	0.29	0.20-0.40
Vanadium	0.04	0.07	0.032	0.059, 0.067	0.05	0.05	0.04	0.05	0.033	0.05	0.05	0.045	-
Titanium	<0.01	0.01	<0.005	0.006	-	-	<0.01	<0.01	-	-	<0.005	<0.005	-
Aluminum	0.02	0.02	0.016	0.02, 0.028	0.026	0.025	0.048	0.042	0.033	0.033	0.017	0.03	0.02-0.1
Zirconium	<0.01	<0.01	<0.005	<0.005	-	-	<0.05	<0.01	-	-	<0.005	<0.005	-
CE	0.55, 0.58	0.60	0.52	0.54, 0.58	0.55	0.55	0.54	0.57	0.51	0.54	0.52	0.51	

$CE = C + (Mn + Si)/6 + (Cr + Mo + V)/5 + (Ni + Cu)/15$.

Table 6a. Weld Metal Hydrogen Content, ppm (ml/100 g)

	North Girder						South Girder			
Labs	Core 3		Core 4	Core A	Core H	Core K	Core 1			Core 2
	Outside Weld 1	Outside Weld 2					Outside Weld 1	Outside Weld 2	Inside Weld 1	
Sherry Lab	-	-	-	6 (5.3)	6 (5.3)	3 (2.7)	-	-	-	-
Aston	1.15 (1.02)	0.06 (0.05)	-	-	-	-	-	-	-	-
Spectro	-	-	1.4 (1.24)		-	-	2.73, 2.77	1.56, 1.84	1.64, 1.79	1.1, 1.4
							(2.43, 2.46)	(1.39, 1.64)	(1.46, 1.59)	(0.98, 1.25)
Metal Analysis	-	-	-	-	-	-	-	-	-	-
Lukens Steel	-	-	-	0.3 (0.27)	0.3 (0.27)	0.4 (0.36)	-	-	-	-

1 ppm = 0.89 mml/100 g. No information is available about the method and accuracy used at Lukens Steel Co.

Table 6b. Base Metal Hydrogen Content, ppm (ml/100 g)

	North Girder										South Girder	
Labs	Core 3		Core 4		Core A		Core H		Core K		Core 1	Core 2
	Web	Stiffener	Web	Flange	Web	Flange	Web	Stiffener	Web	Flange	Stiffener	Flange
Sherry Lab					3 (2.7)	7 (6.23)	6 (5.3)	5 (4.45)	2 (1.78)	2 (1.78)		2 (1.78)
Aston	1.08 (0.96)	5.14 (4.6)										
Spectro			1.8 (1.6)	0.9, 2.5							1.9 (1.7)	3.1 (2.8)
				(0.8, 2.2)								
Metal Analysis						6 (5.3)	2, 7			3 (2.7)		
							(1.78, 6.23)					
Lukens Steel						0.2 (0.18)	0.3 (0.27)	0.2 (0.18)	0.2 (0.18)		0.3 (0.27)	0.6 (0.53)

1 ppm = 0.89 ml/100 g. No information is available about the method and accuracy used at Lukens Steel Co.

Table 7. Tensile Test Results for Top Flange Base Metal at Room Temperature

	North Girder		South Girder
Properties	**Core A**	**Core K**	**Core 2**
Tensile Strength, MPa [ksi]	678	567, 592, 656	645
	[98.3]	[82.2, 85.8, 95.1]	[93.5]
Yield Strength, MPa [ksi]	559	420, 445, 556	506
	[81]	[60.9, 64.5, 80.6]	[73.4]
Elongation, %	30	31, 35, 26	29

Table 8. Charpy V-Notch Results, J (ft-lb)

	North Girder							South Girder	
	Core 3	Core 4			Core A	Core H	Core K	Core 2	
Labs	Weld	Weld	HAZ	Top Flange	Top Flange	Web	Top Flange	Weld	Top Flange
Sherry Lab						140, 176 at -7°C	197, 201 at -7°C		
						(104, 130 at +20°F)	(146, 149 at +20°F)		
				120, 146, 148 at -18°C	143, 150, 180 at -23°C	98, 209, 217 at -23°C	154, 209, 230 at-23°C		163, 177, 208 at -23°C
				(89, 108, 110 at 0°F)	(106, 111, 133 at -10°F)	(73,155, 161 at -10°F)	(114, 155, 170 at -10°F)		(121, 131, 154 at -10°F)
Aston	76 at -23°C								
	(56 at -10°F)								
FHWA		110 at -18°C		112, 123 at -18°C					62, 90 at -18°C
		(81 at 0°F)		(83, 91 at 0°F)					(46, 67 at 0°F)

ASSHTO Zone 2 requirement for base metal is 48 J (35 ft-lb) at -7°C (20°F). AASHTO toughness requirement for weld metal with matching strength is minimum 41 J (30 ft-lb) at -32°C (-25°F).

Table 9. Hardness Test Results at Room Temperature

Core, Girder	Parameter	Base Metal-Flange	Base Metal-Web	Base Metal-Stiffener	HAZ-1	Fusion-1	Weld	Fusion-2	HAZ-2
Core 3, North Girder	Microhardness	208, 228, 240 HK	-	-	231, 236, 250 HK	283, 293, 319 HK	277, 286, 287 HK	-	-
		(192, 212, 227 HV)	-	-	(216, 222, 239 HV)	(273, 283, 311 HV)	(292, 274, 277 HV)	-	-
	Hardness	-	-	-	68, 69, 70 HRN	-	69,70 HRN	-	-
		-	-	-	(/, 238, 242 HV)	-	(238, 242 HV)	-	-
Core 4, North Girder	Microhardness	238, 241 HK	-	-	245, 265 HK	285, 307 HK	254, 271, 305 HK	-	-
		(225, 228 HV)	-	-	(233, 253, HV)	(273, 302 HV)	(242, 259, 295 HV)	-	-
	Hardness	-	-	-	71 HRN	-	71, 72, 75 HRN	-	-
		-	-	-	(254 HV)	-	(254, 265, 302 HV)	-	-
Core A, North Girder	Microhardness	208, 209, 210 HV	213, 219, 227 HV	-	230, 243, 273 HV	255, 256, 261 HV	258, 262, 263 HV	265, 269, 280 HV	229, 230, 234 HV
	Hardness	92.5, 93, 93 HRB	93, 94, 94.5 HRB	-	100, 100, 100 HRB	-	99, 100, 100 HRB	-	93, 94, 94.5 HRB
		(200 HV)	(205 HV)	-	(240 HV)	-	(234, 240, 240 HV)	-	(200, 205, 213 HV)
Core H, North Girder	Microhardness	-	218, 223, 228 HV	211, 219, 271 HV	280, 281, 283 HV	257, 260, 269 HV	230, 240, 241 HV	234, 242, 252 HV	229, 233, 252 HV
	Hardness	-	95, 95, 95 HRB	95, 95, 95 HRB	17, 19, 24 HRC	-	19, 19, 20 HRC	12, 12, 13 HRC	-
		-	(210 HV)	(210 HV)	(<238 HV)	-	(<238, 238 HV)	(<238 HV)	-
Core K, North Girder	Microhardness	194, 202, 209 HV	215, 215, 220 HV	-	224, 234, 236 HV	231, 236, 246 HV	240, 246, 262 HV	277, 281, 282 HV	265, 278, 278 HV
	Hardness	90, 91.5, 92.5 HRB	93, 94, 94 HRB	-	100, 100, 100 HRB	98, 100, 100 HRB	95, 97.5, 99 HRB	99, 100, 100 HRB	96.5, 98, 100 HRB
		(190 HV)	(205 HV)	-	(240, 240, 240 HV)	(228, 240, 240 HV)	(210, 226, 234 HV)	(234, 240, 240 HV)	(218, 228, 240 HV)
Core 1, South Girder	Microhardness	-	-	-	-	-	-	-	-
	Hardness	-	-	-	-	-	-	-	-
Core 2, South Girder	Microhardness	230 HK (215 HV)	-	-	239 HK (226 HV)	-	240, 282 HK	-	-
		-	-	-	-	-	(227, 270 HV)	-	-
	Hardness	-	-	-	-	-	73 HRN (275 HV)	-	-

HV = Vickers hardness number; HRB = Rockwell B hardness number; HRC = Rockwell C hardness number; HRN = Rockwell superficial hardness number; HJ = Knoop hardness number; (200 HV) = converted Vickers hardness number.

FIGURES

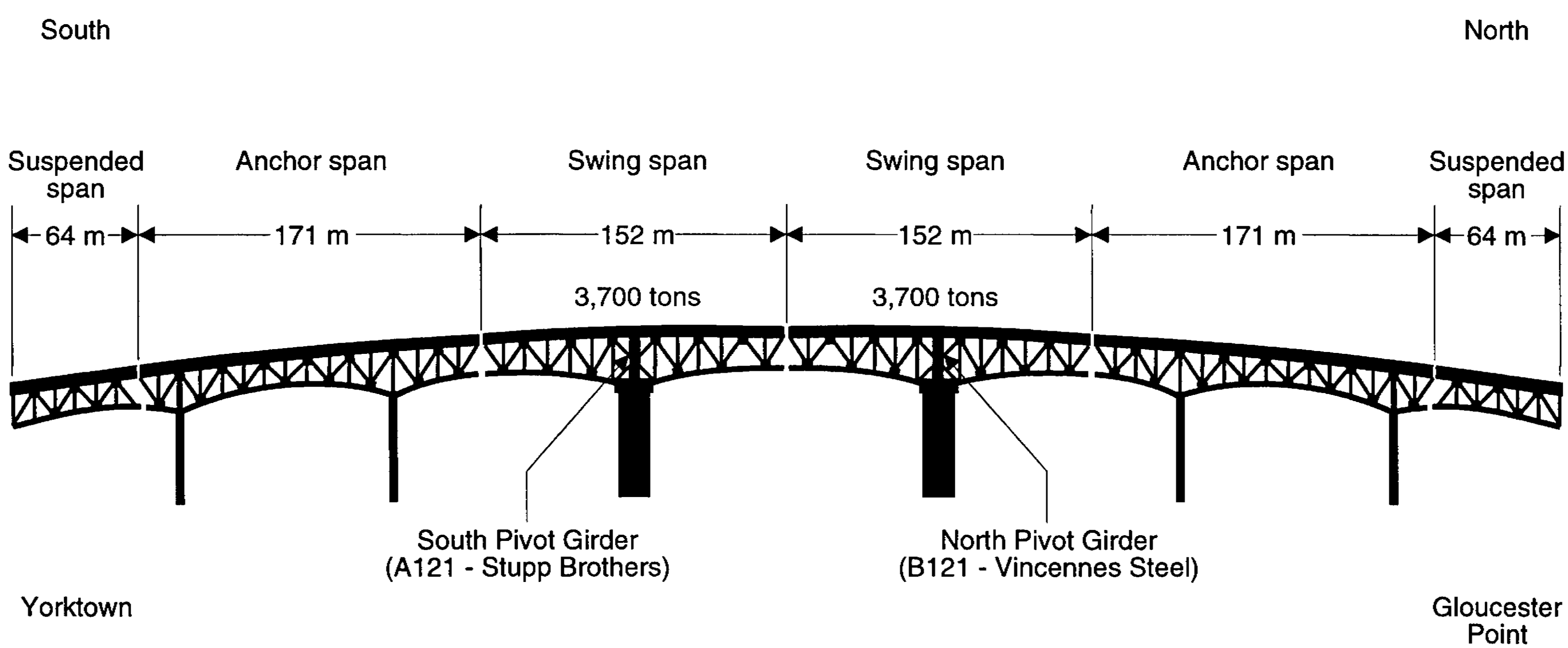

Figure 1. Elevation Looking West for the George P. Coleman Bridge.

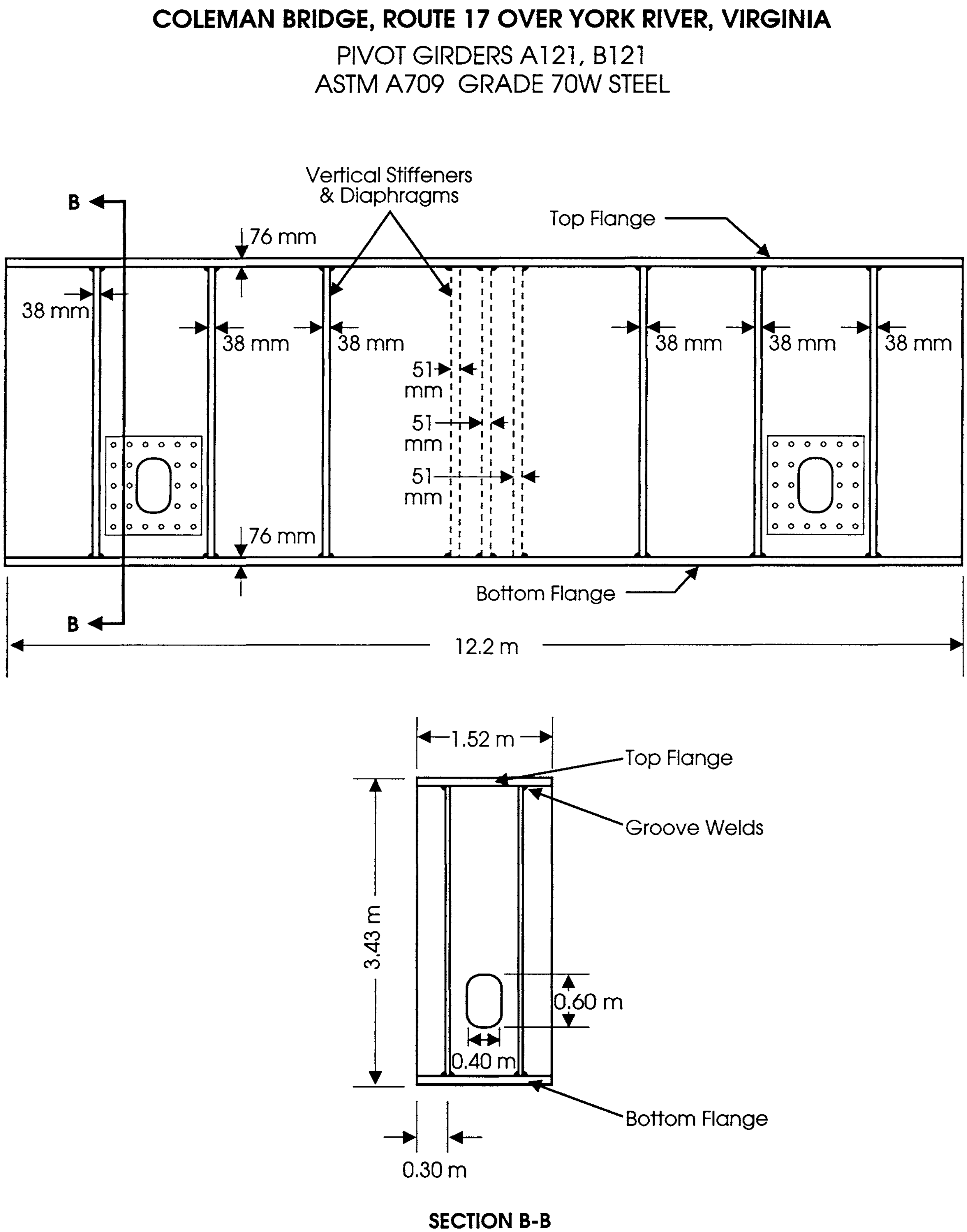

Figure 2. Box Sketch and Typical Details.

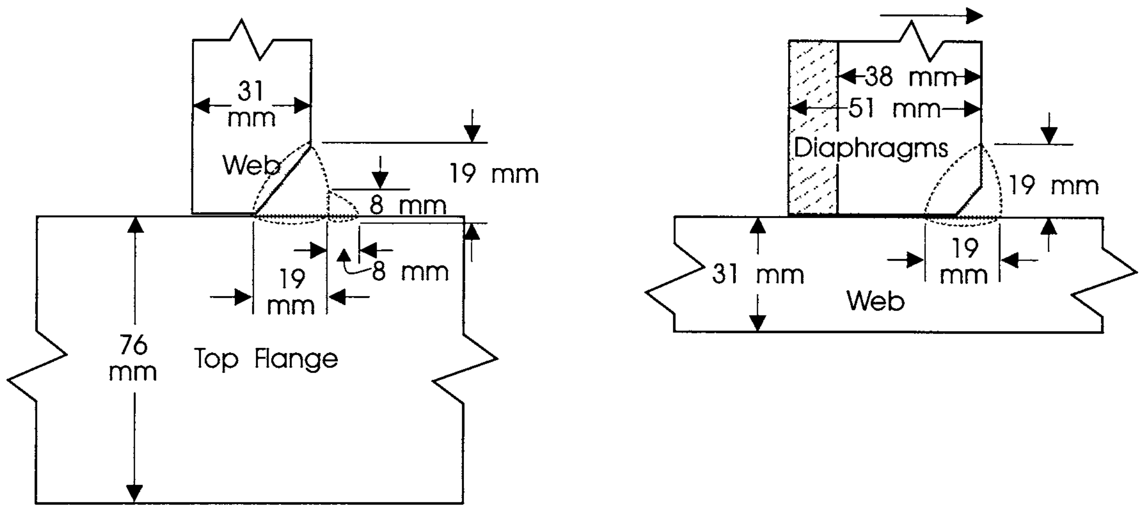

a) Web-to-top flange and web-to-diaphragms single bevel groove welds

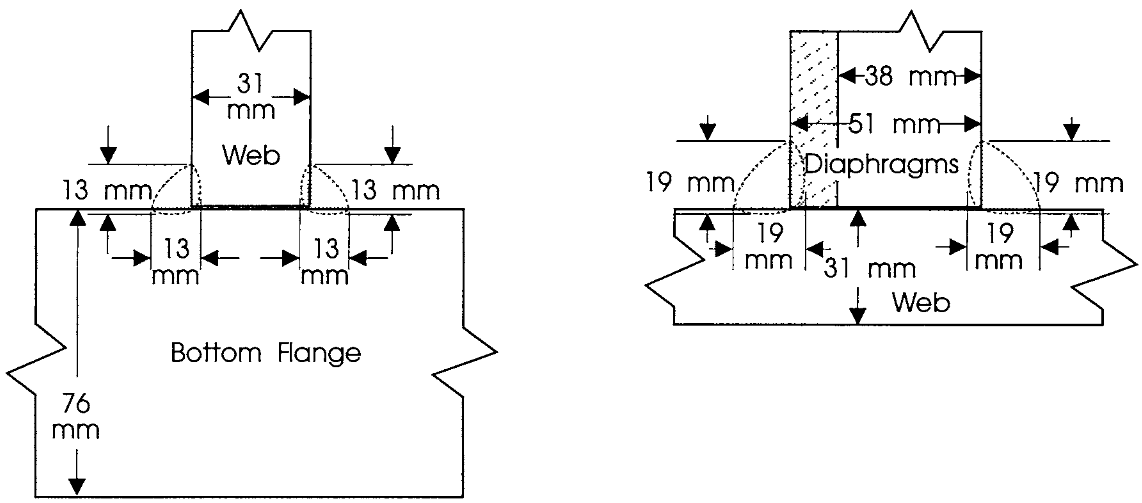

b) Web-to-bottom flange and web-to-stiffeners (diaphragms) fillet welds

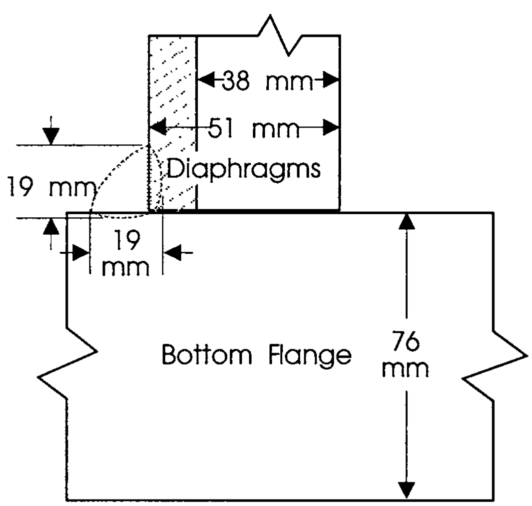

c) Bottom flange-to-diaphragms fillet welds

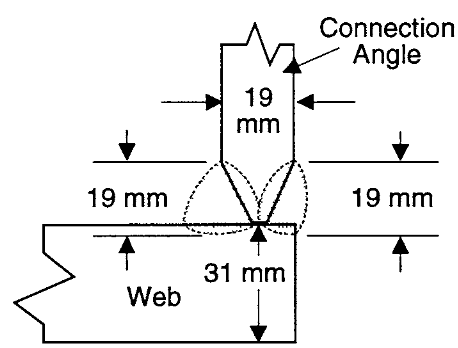

(d) Web-to-connection angle welds

Figure 3. Weld Sketches.

Figure 4. Typical MT Transverse and Longitudinal Indications, June 1996 MT.

(a) location A

(b) location AT

(c) location R

(d) locations AK and AL

(e) location AB

(f) locations G and H.

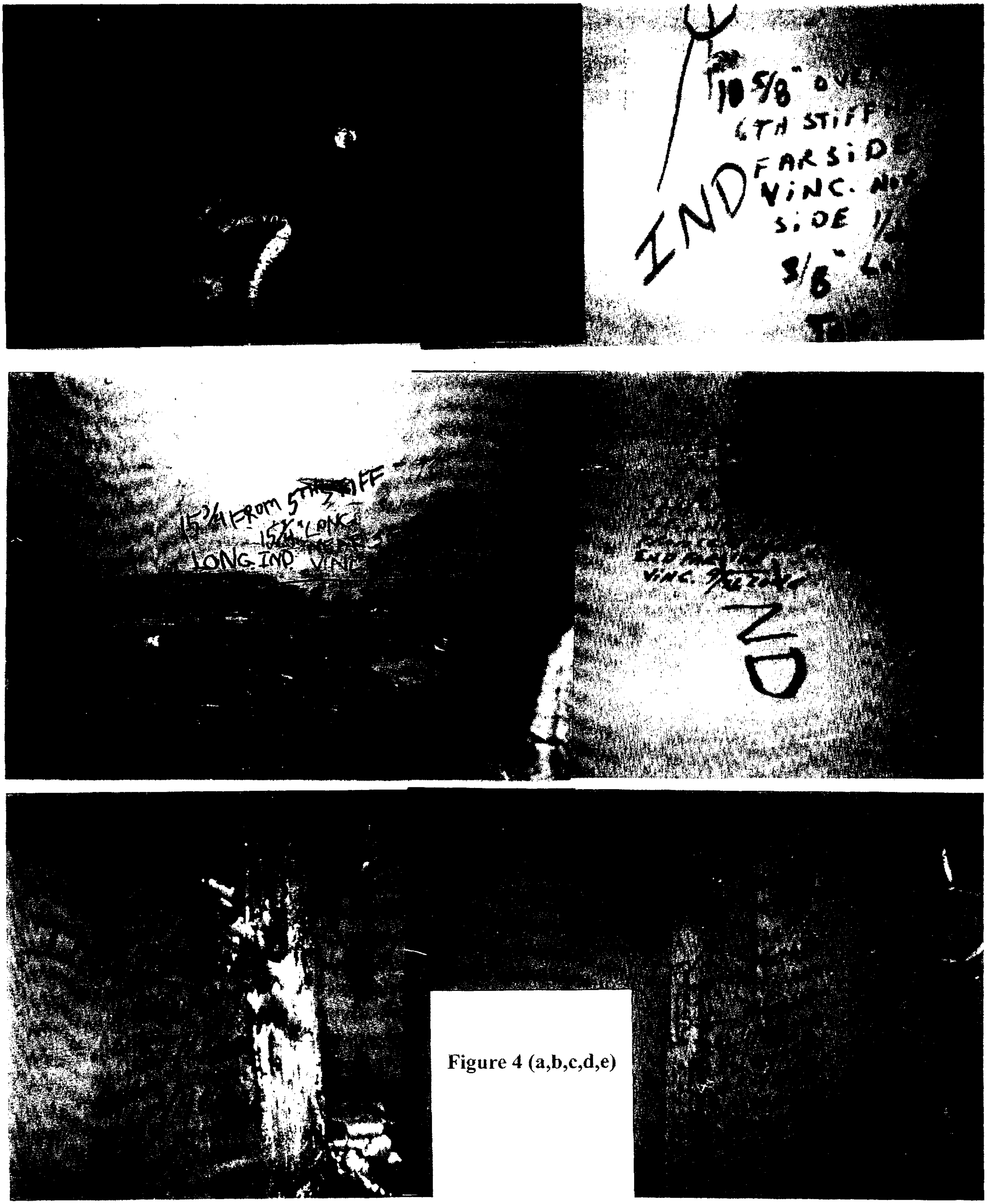

Figure 4 (a,b,c,d,e)

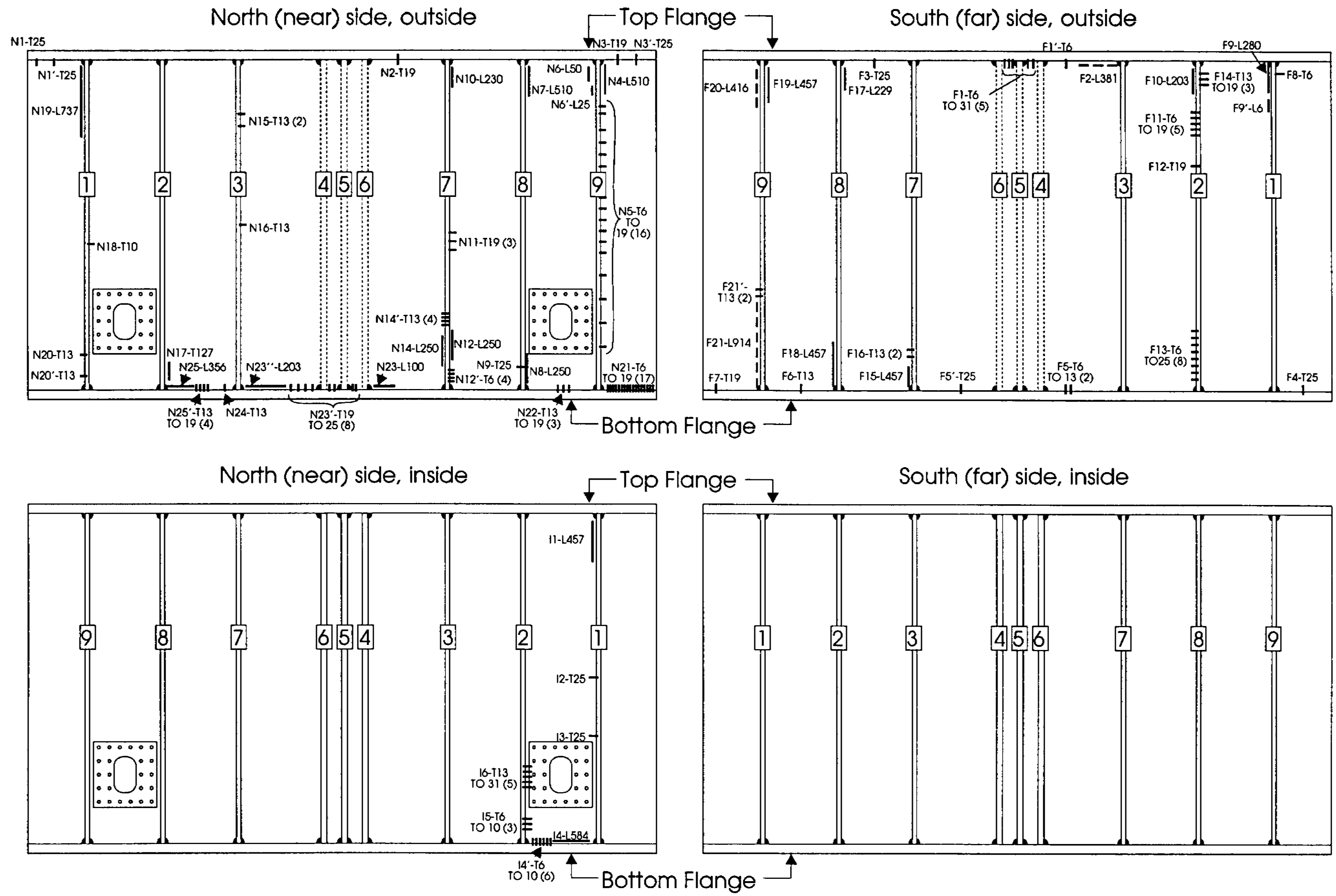

Note: A1-T15 (2) = Location (letter & number), type (T-transverse, L-longitudinal), length (in millimeters) & (n) number of cracks

Figure 5. North Girder, MT Inspection, March 1995.

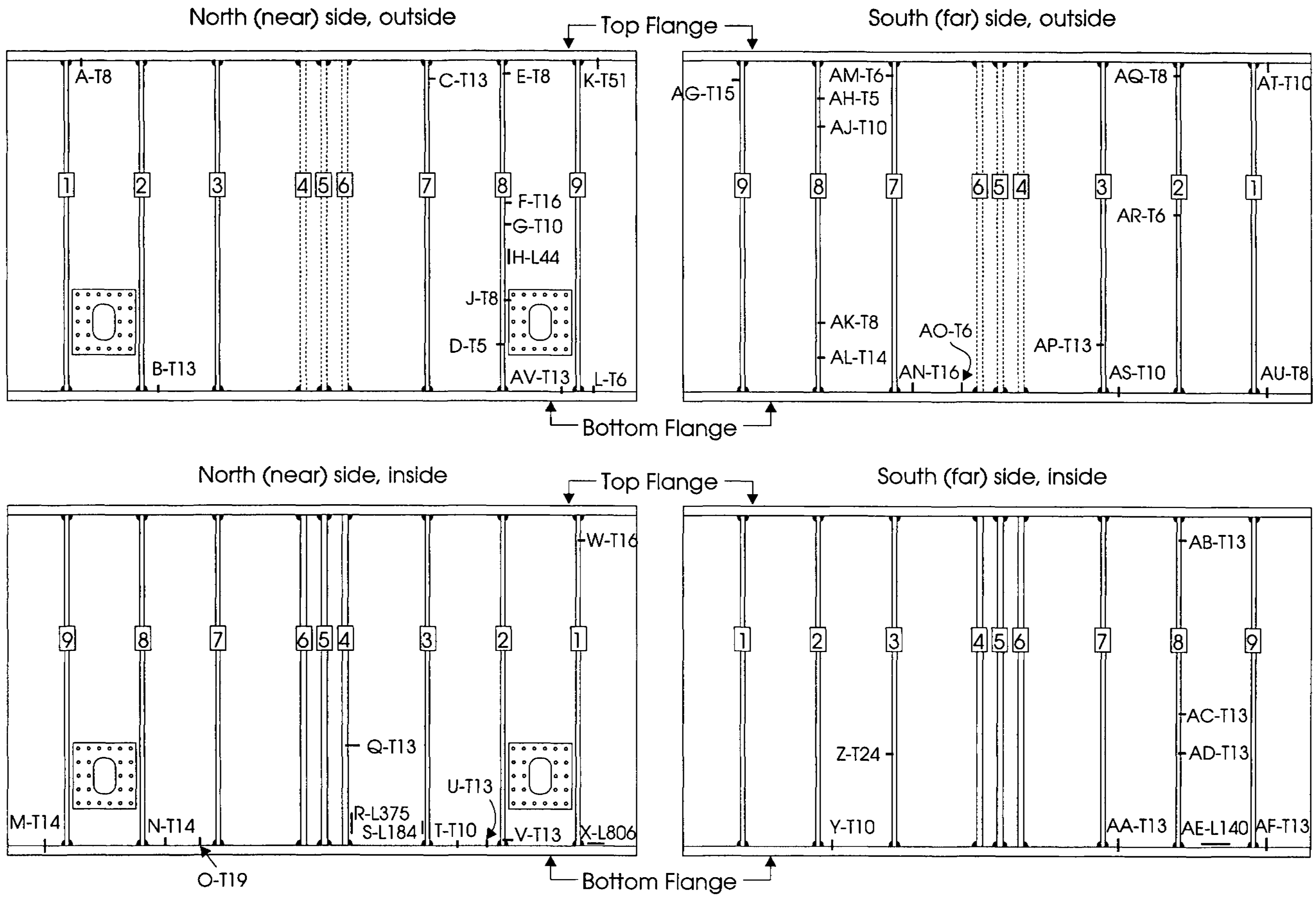

Note: A-T15 = Location (letter), type (T-transverse, L-longitudinal) & length (in millimeters).

Figure 6. North Girder, MT Inspection, June 1996.

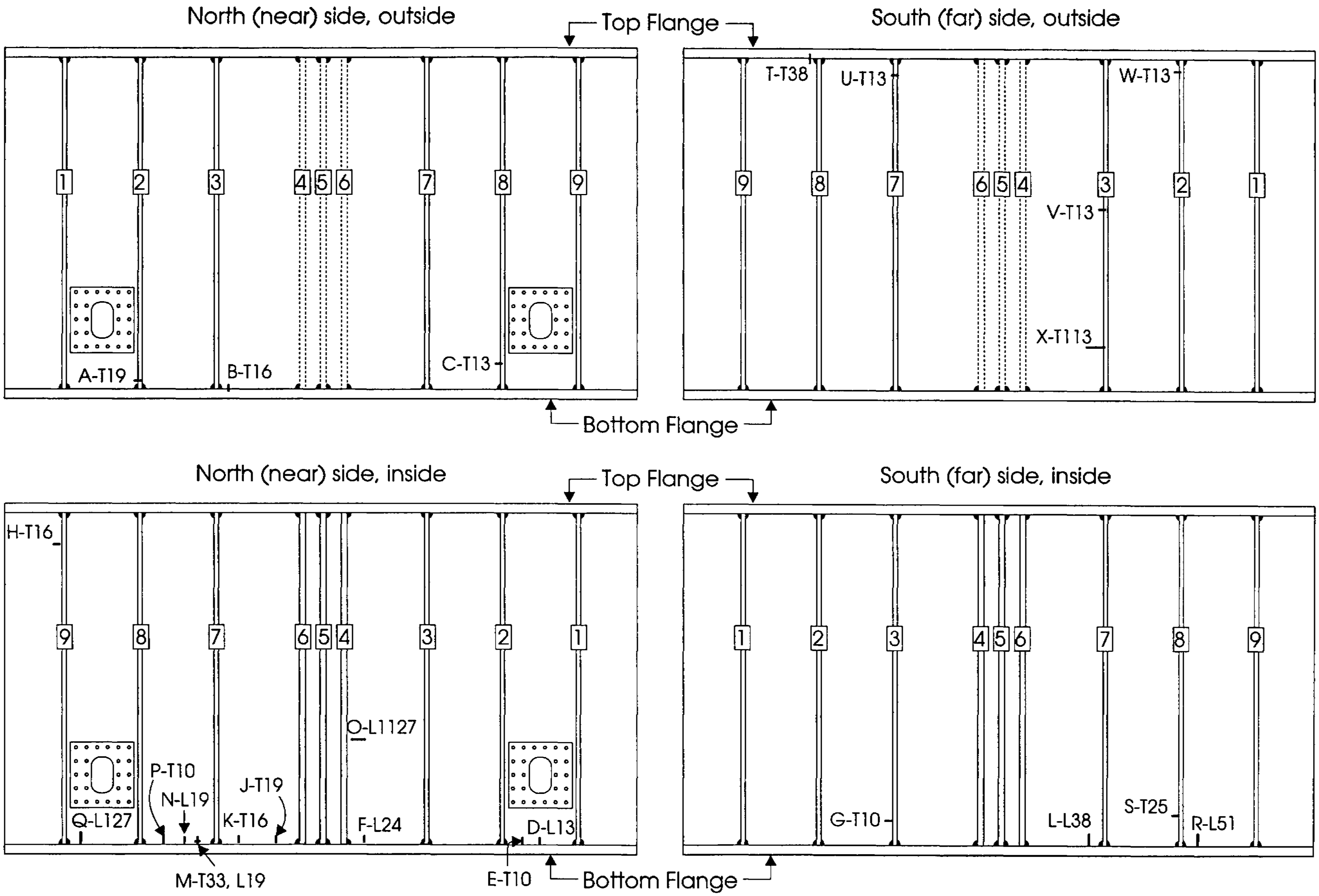

Note: A-T15 = Location (letter), type (T-transverse, L-longitudinal) & length (in millimeters).

Figure 7. North Girder, MT Inspection, April 1997.

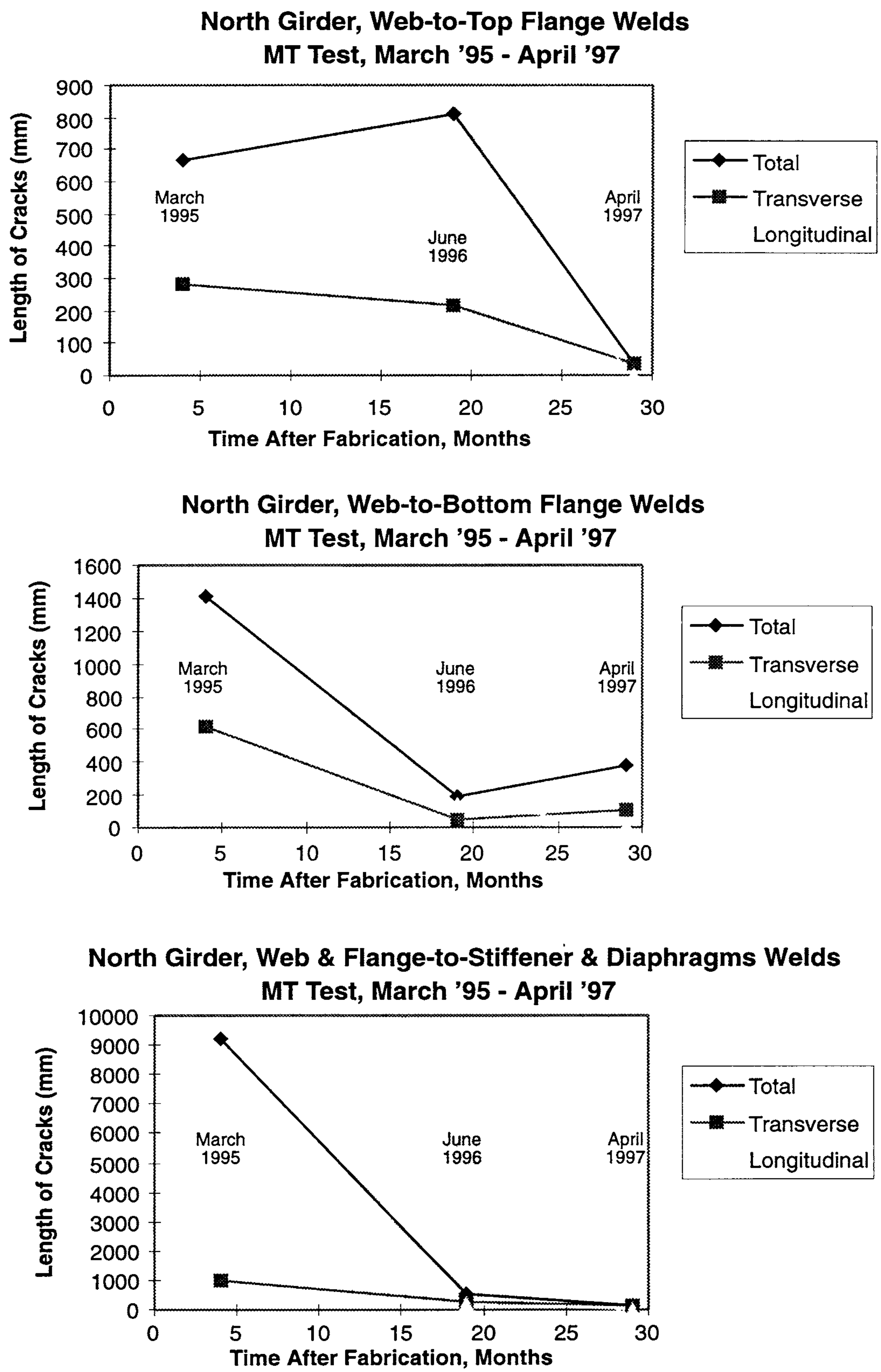

Figure 8. Distribution of Number of Cracks vs. Time After Fabrication.

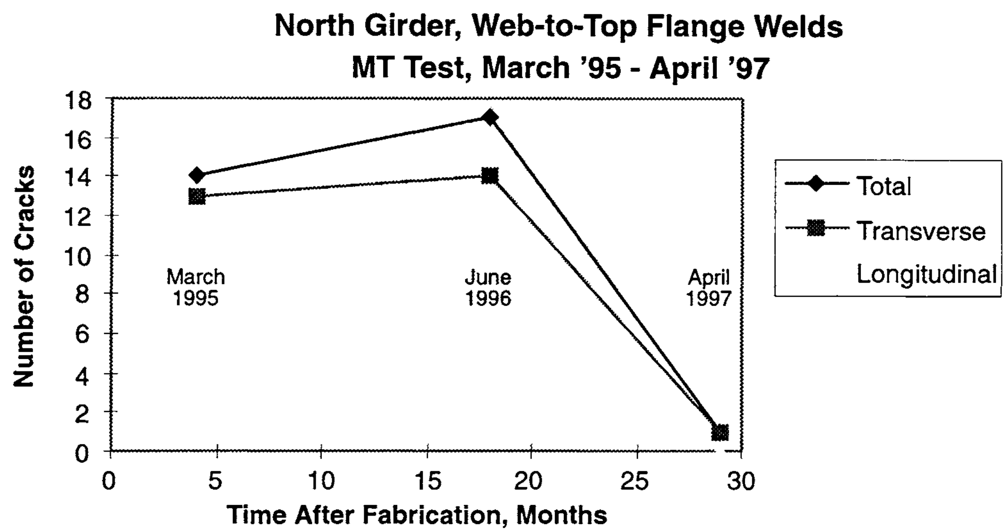

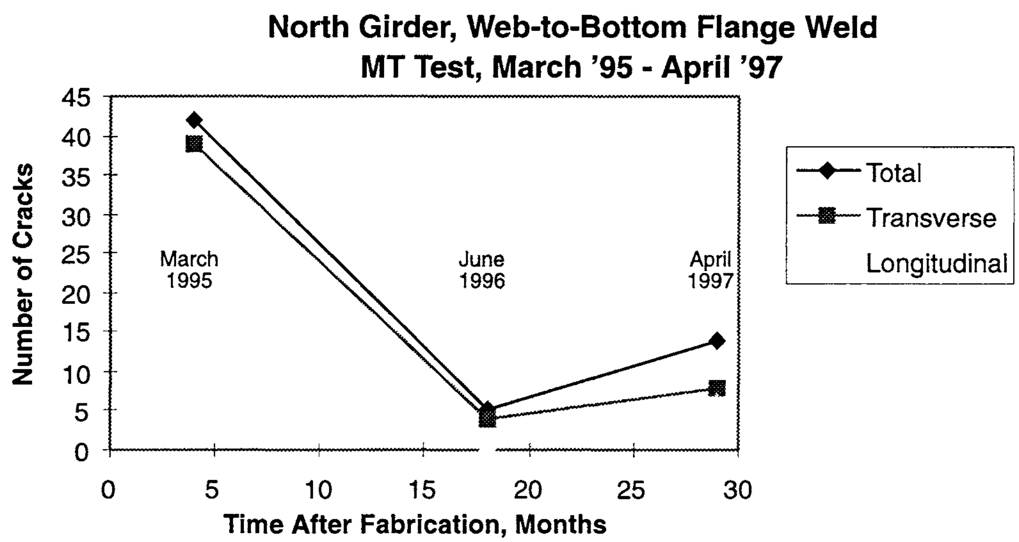

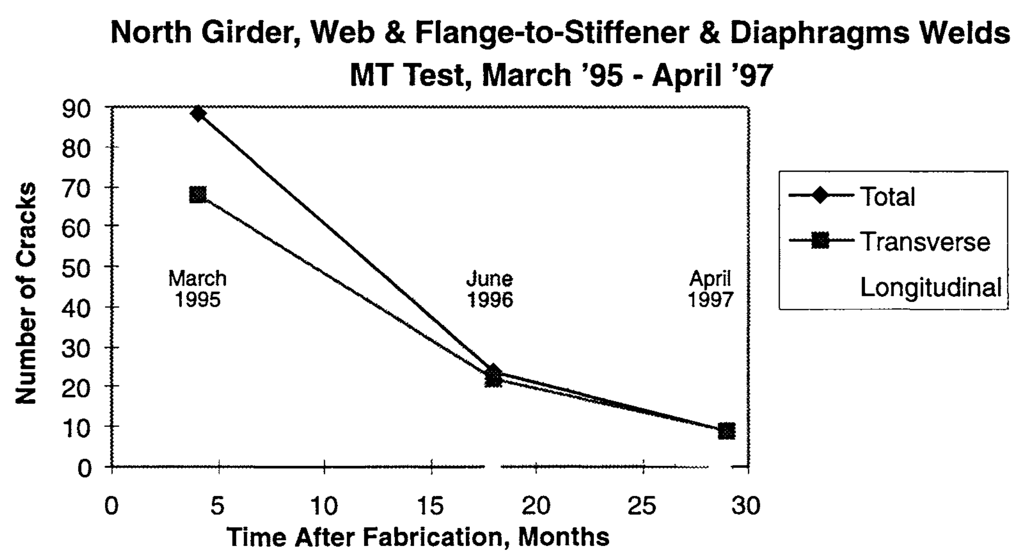

Figure 9. Distribution of Length of Cracks vs. Time After Fabrication.

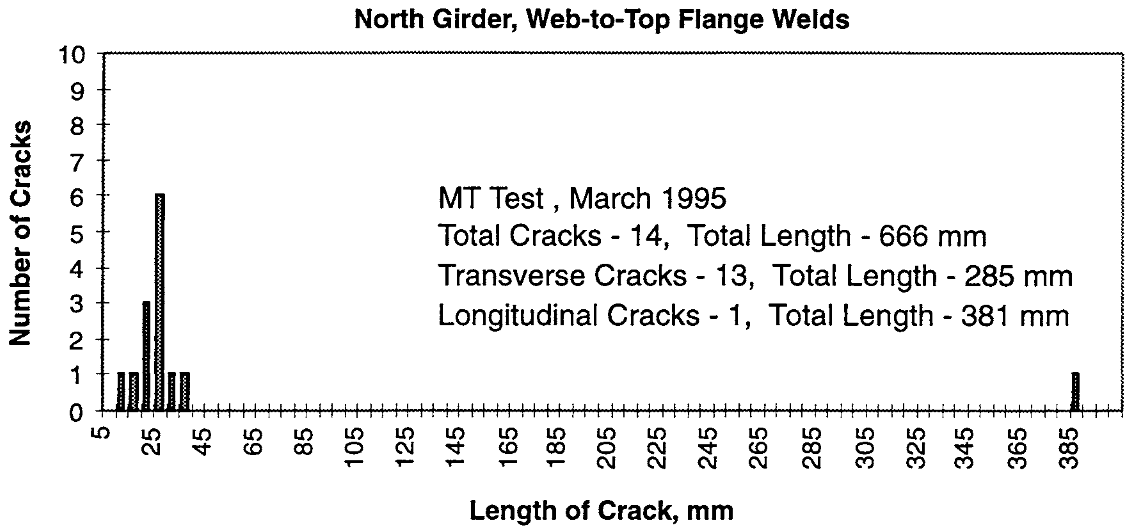

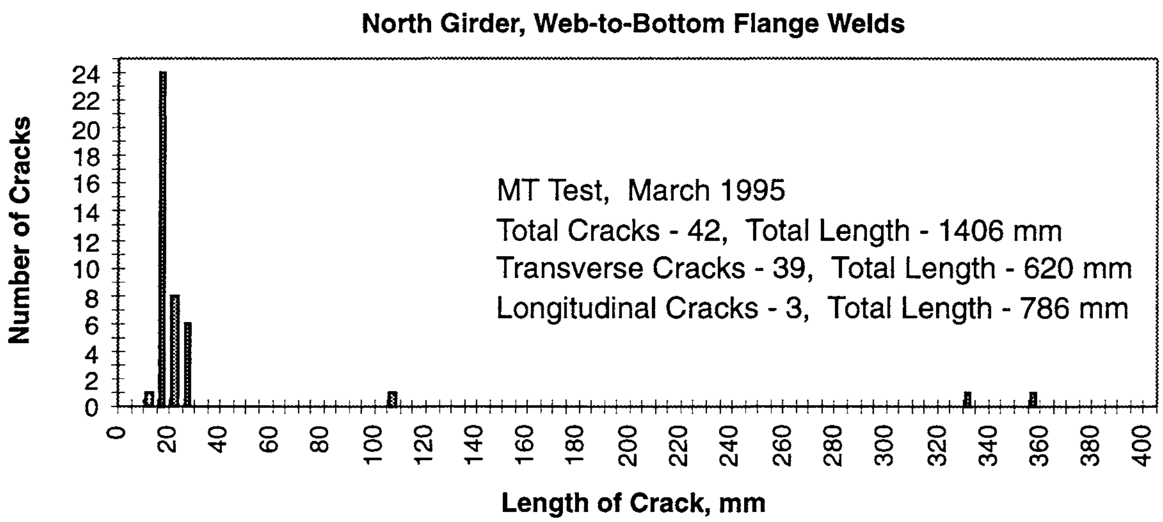

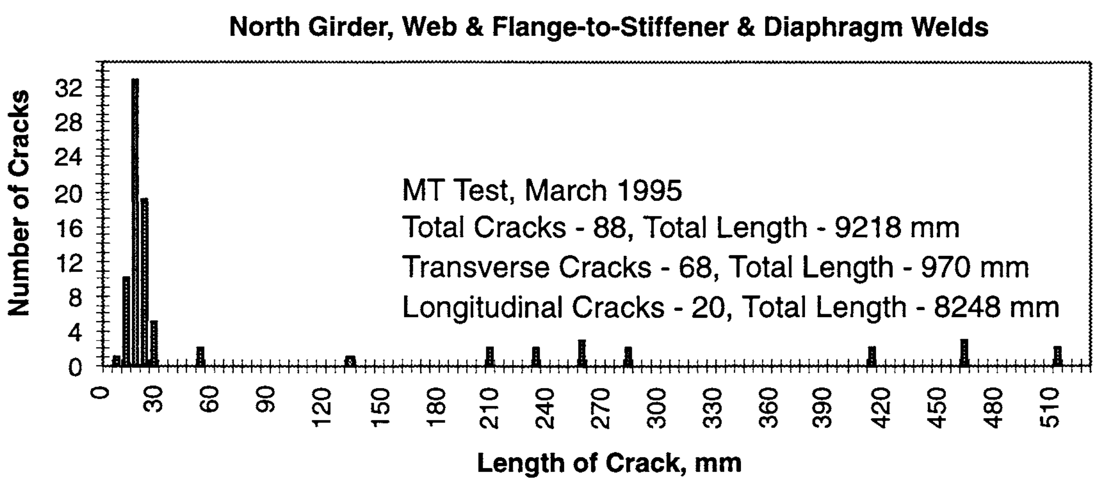

Figure 10. Distribution of Number of Cracks vs. Length of Crack, March 1995.

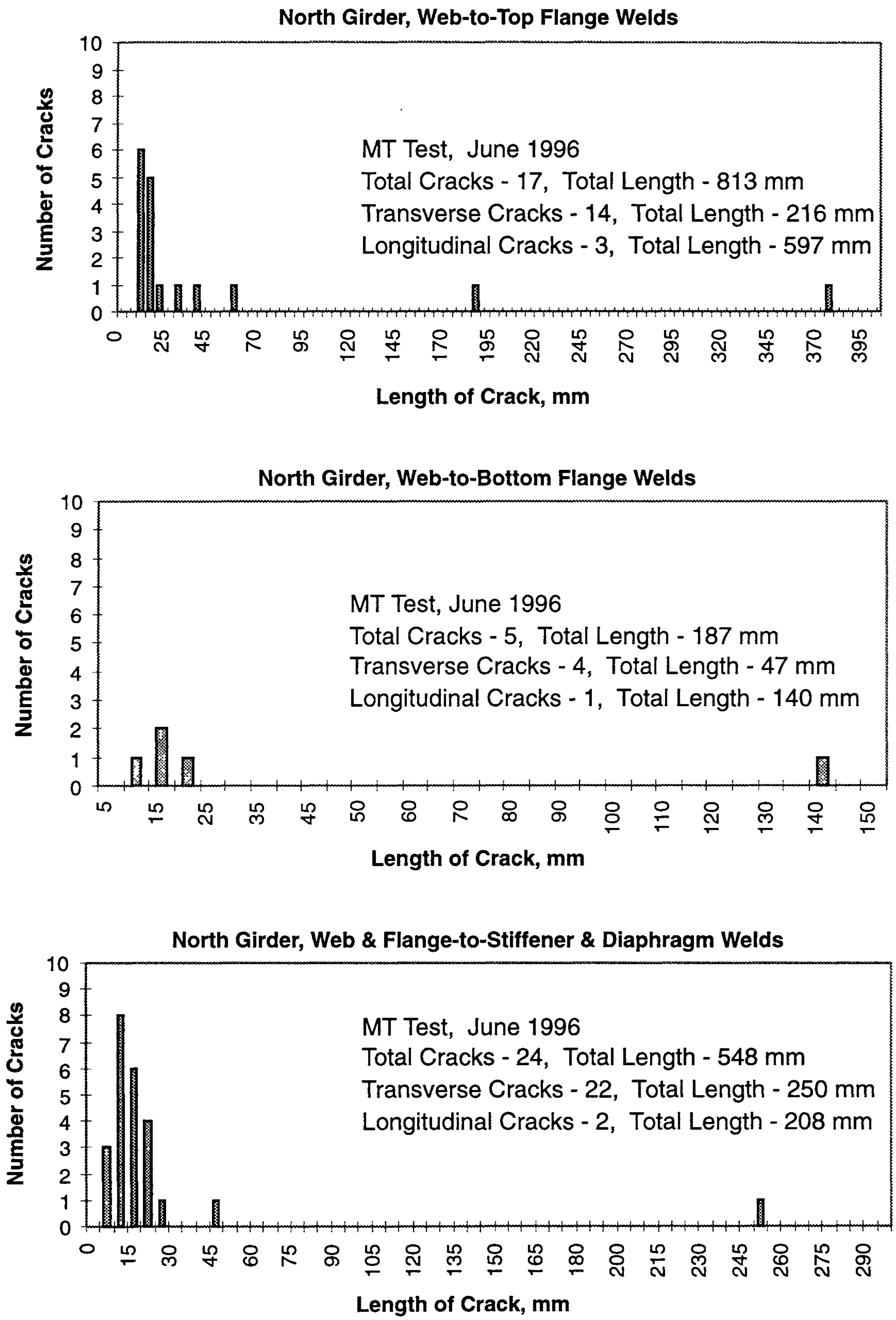

Figure 11. Distribution of Number of Cracks vs. Length of Crack, June 1996.

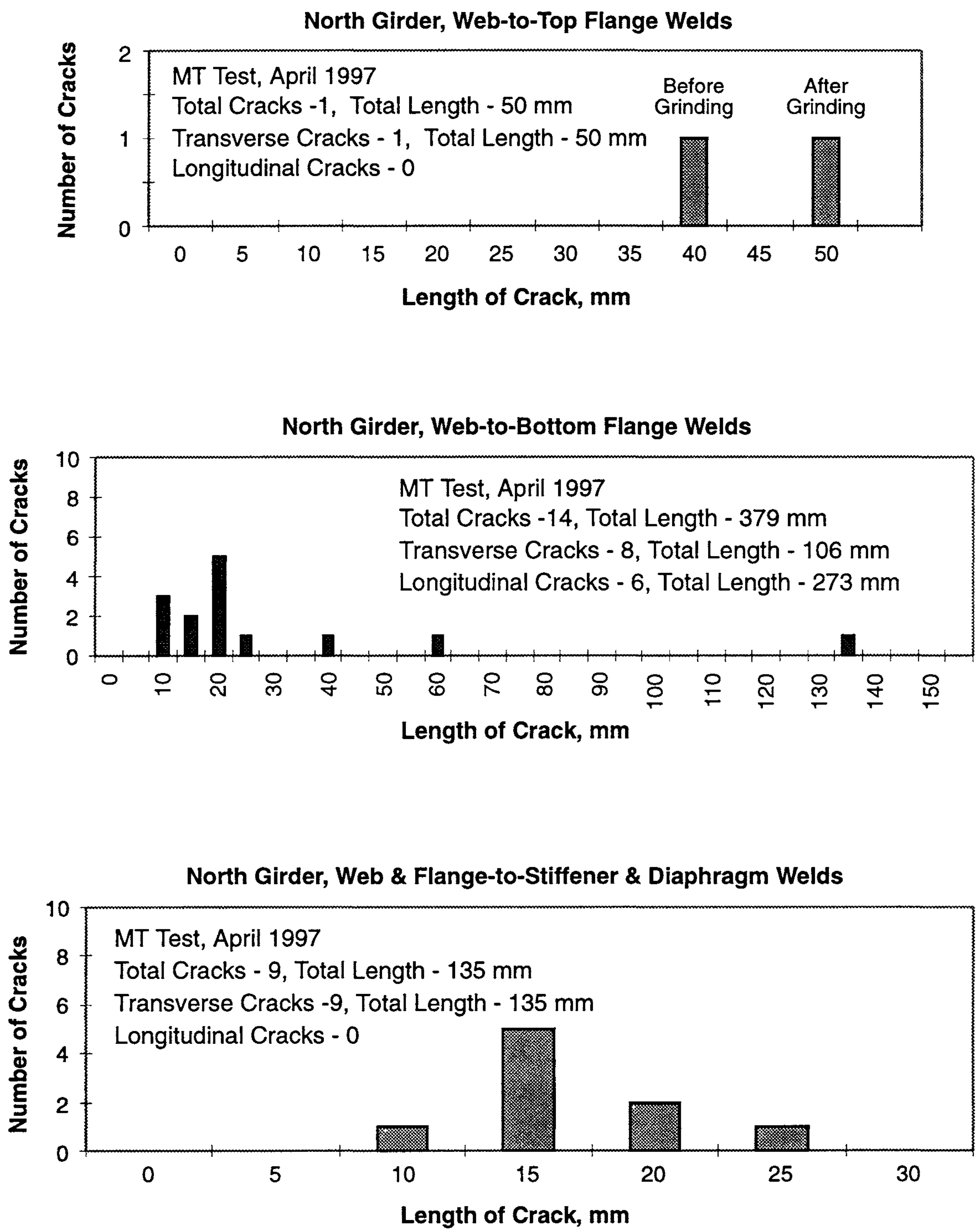

Figure 12. Distribution of Number of Cracks vs. Length of Crack, April 1997.

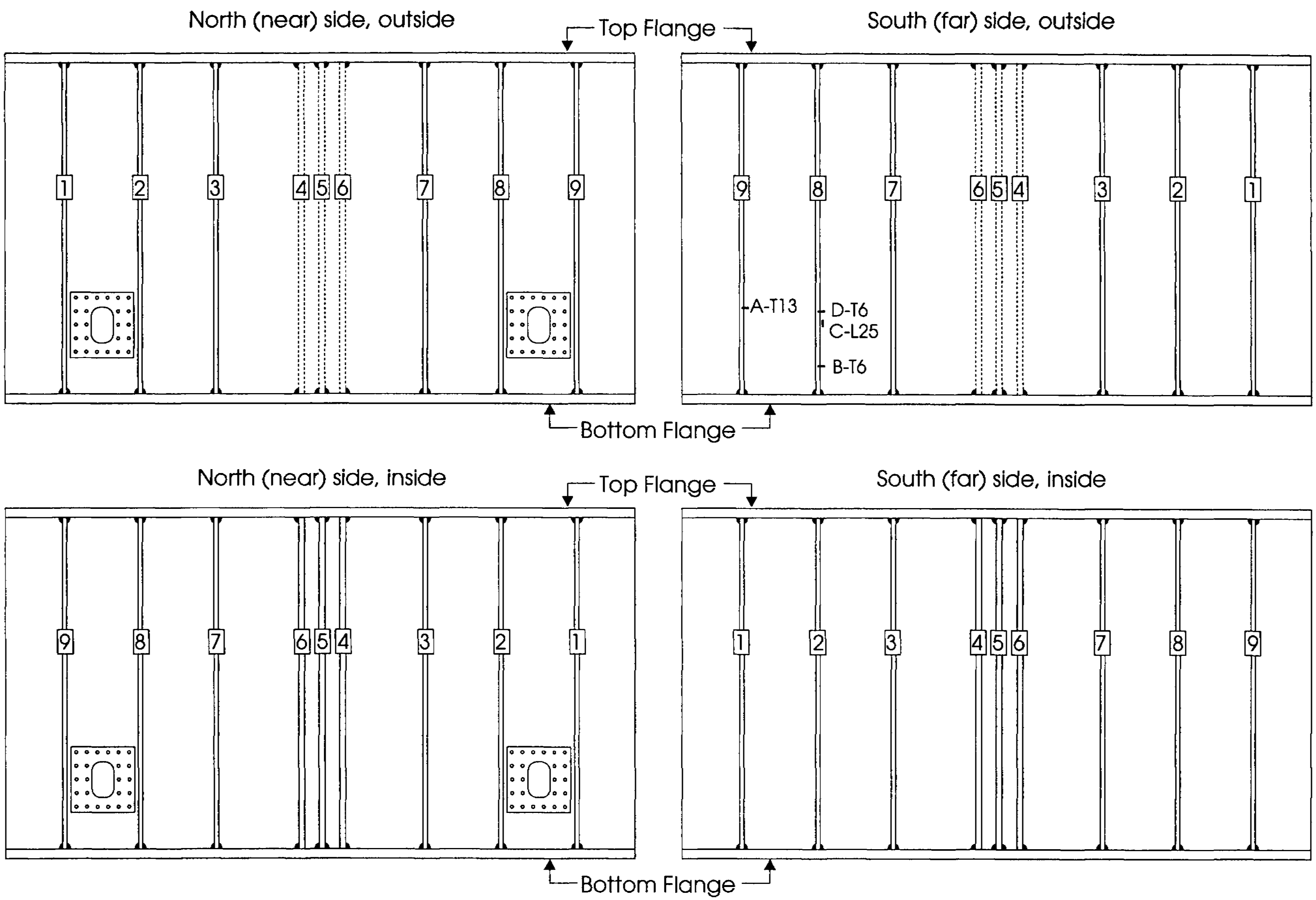

Note: A-T15 = Location (letter), type (T-transverse, L-longitudinal) & length (in millimeters).

Figure 13. South Girder, MT Inspection, June-October 1995.

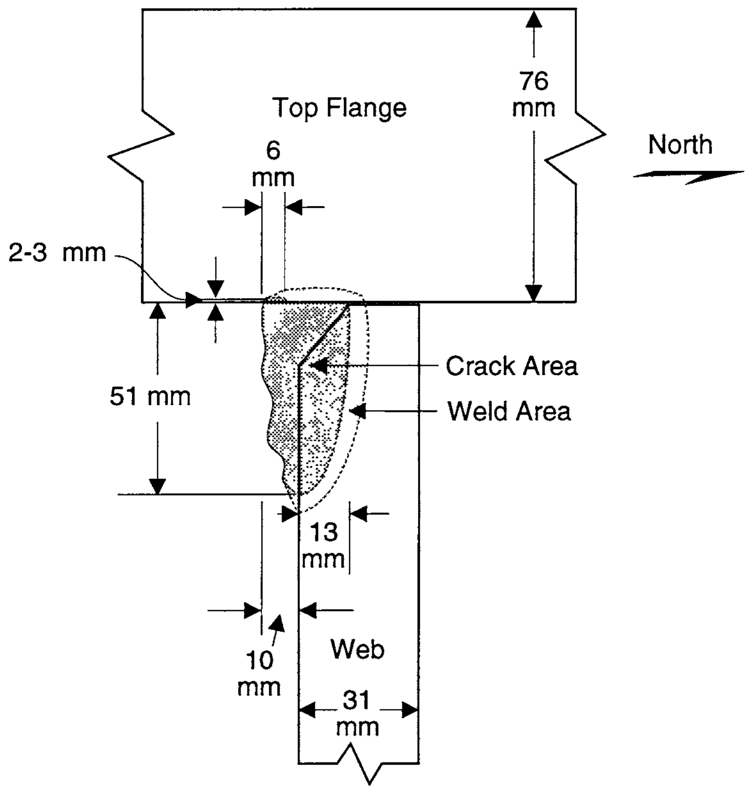

Figure 14. Projected Crack Geometry.

Figure 15. Radiographs for Cracks at Location A, June 1996 MT Results.

Figure 16. Equipment for Blind Hole-Drilling Strain-Gage Residual Stress Measurements at Groove Web-to-Top Flange Weld.

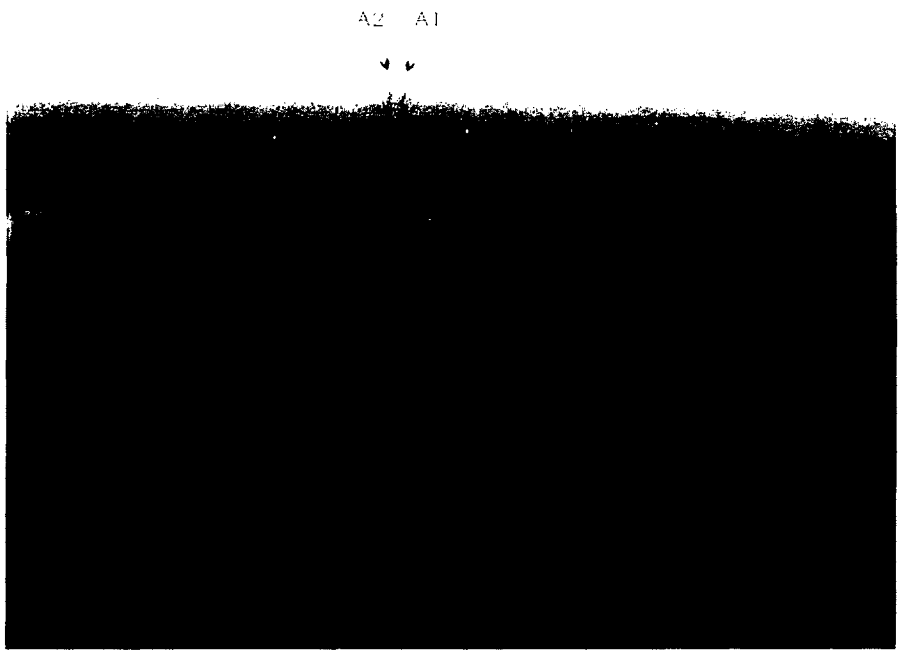

Figure. 15

Figure. 16

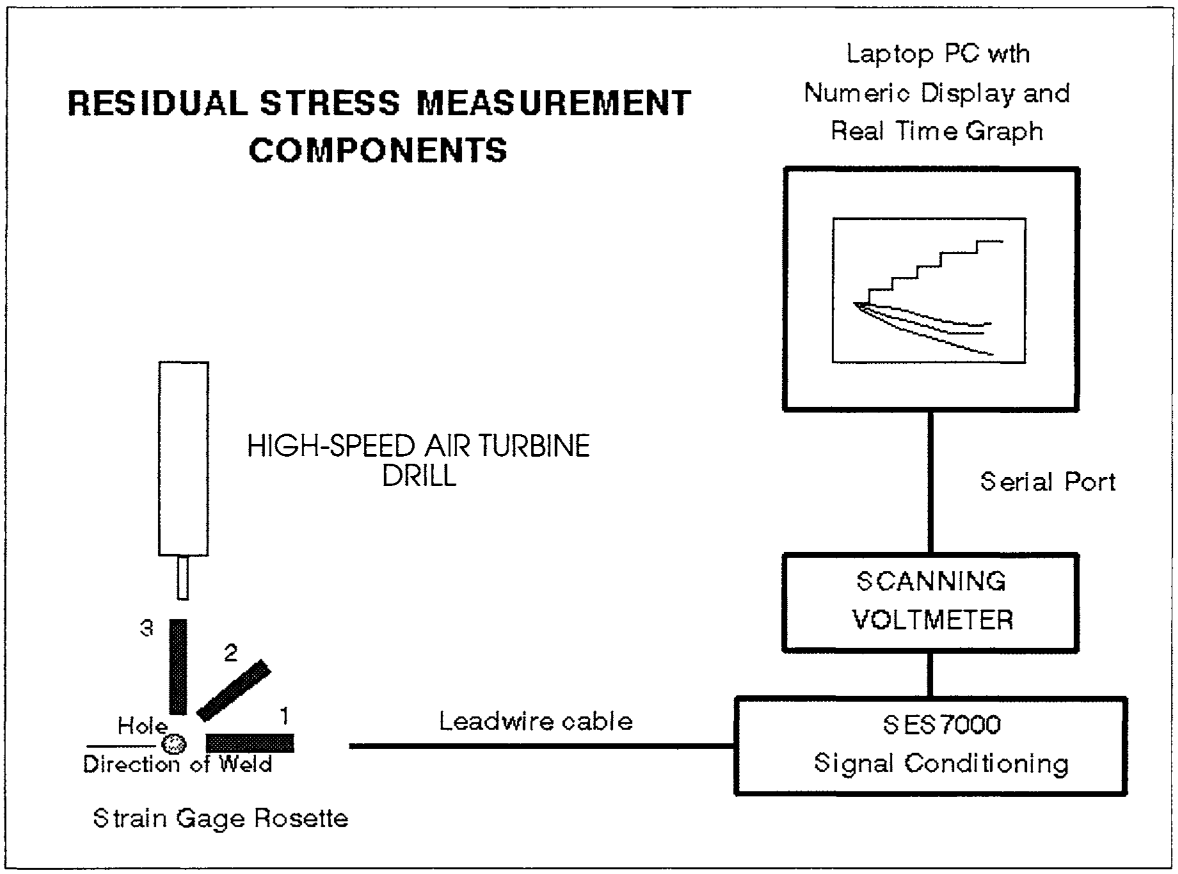

Figure 17. High-Speed Blind Hole Drilling Residual Stress Measurement Components

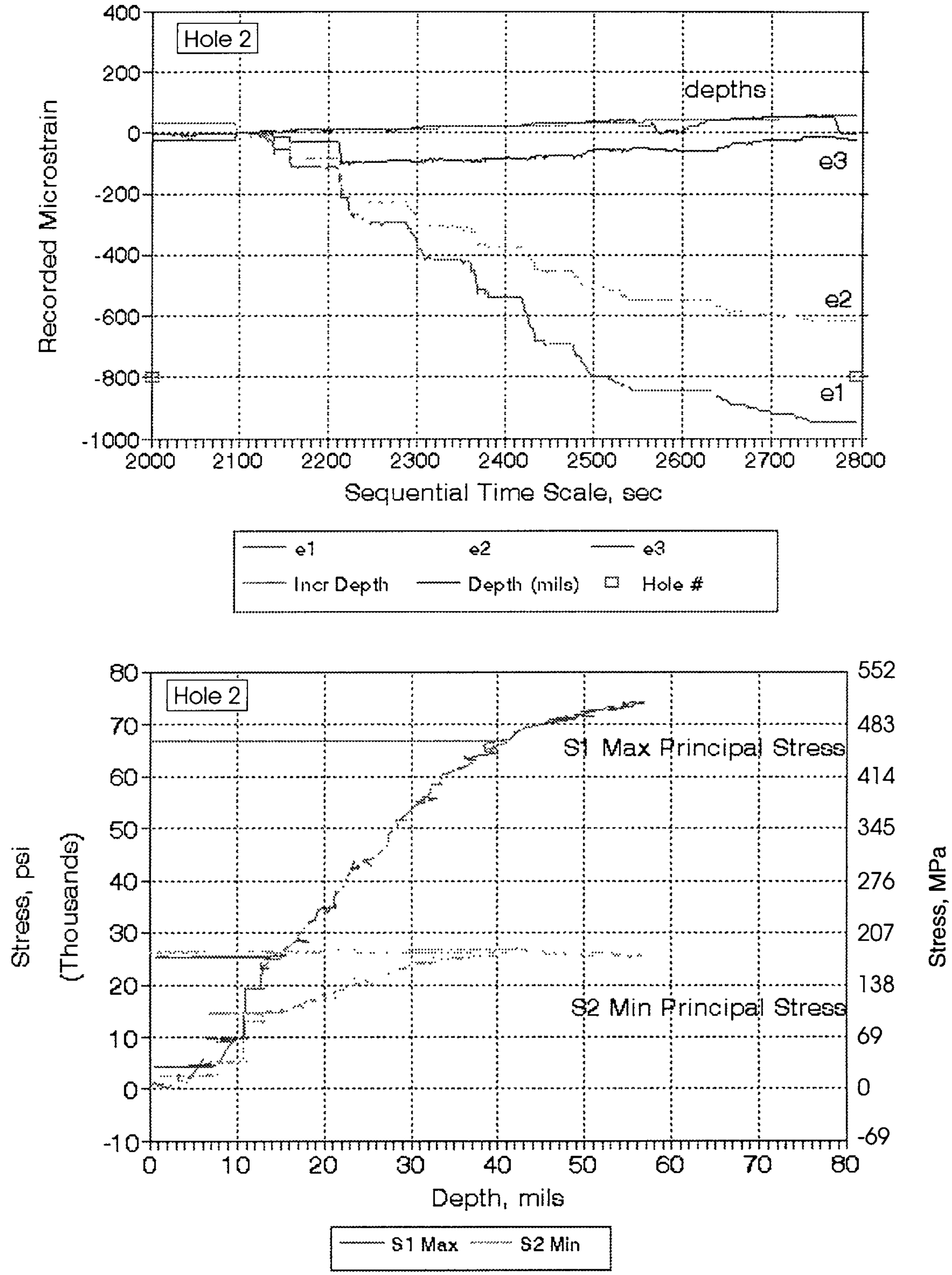

Figure 18. Microstrain vs. Elapsed Time and Stress vs. Depth for Hole 2.

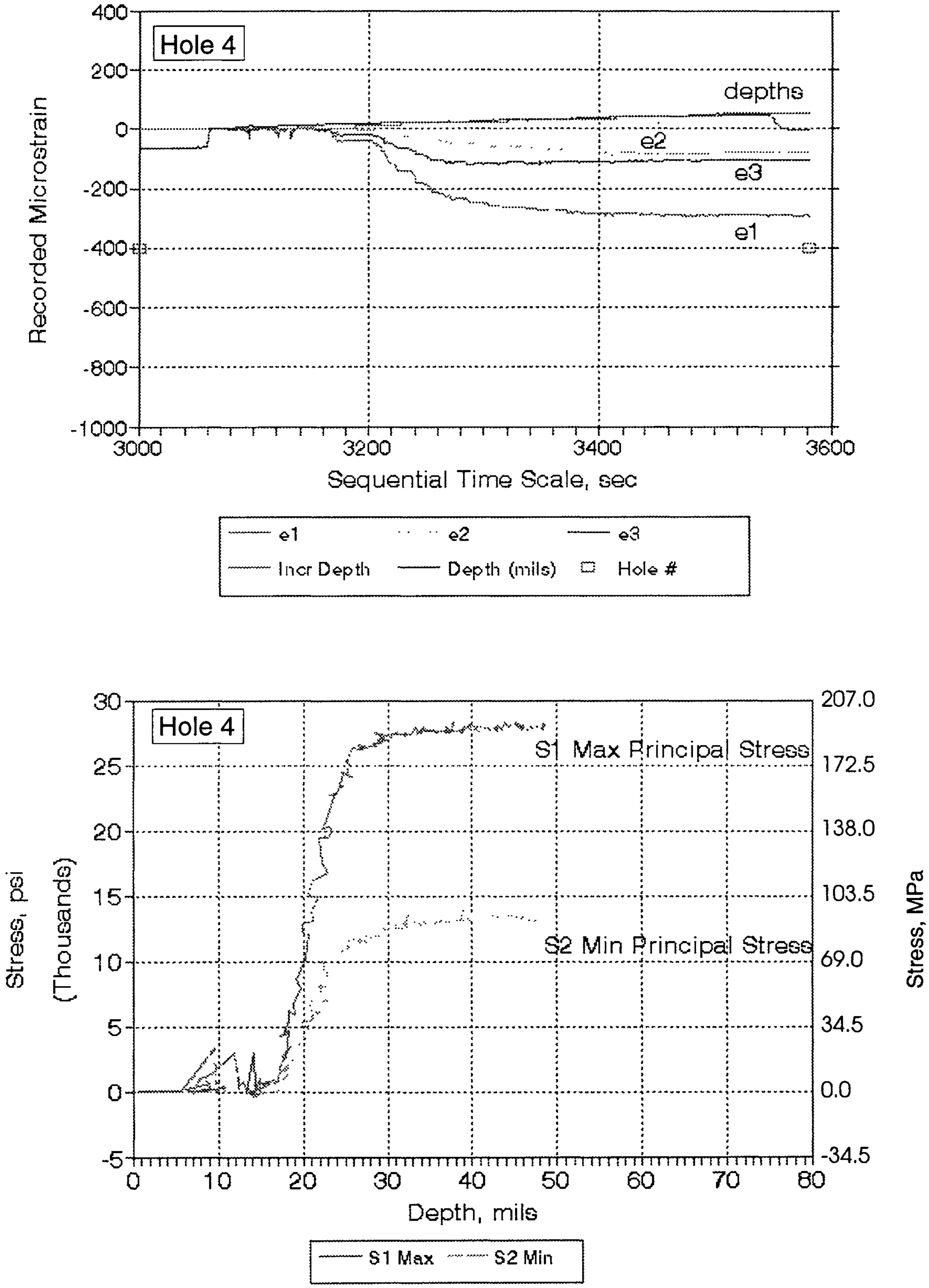

Figure 19. Microstrain vs. Elapsed Time and Stress vs. Depth for Hole 4.

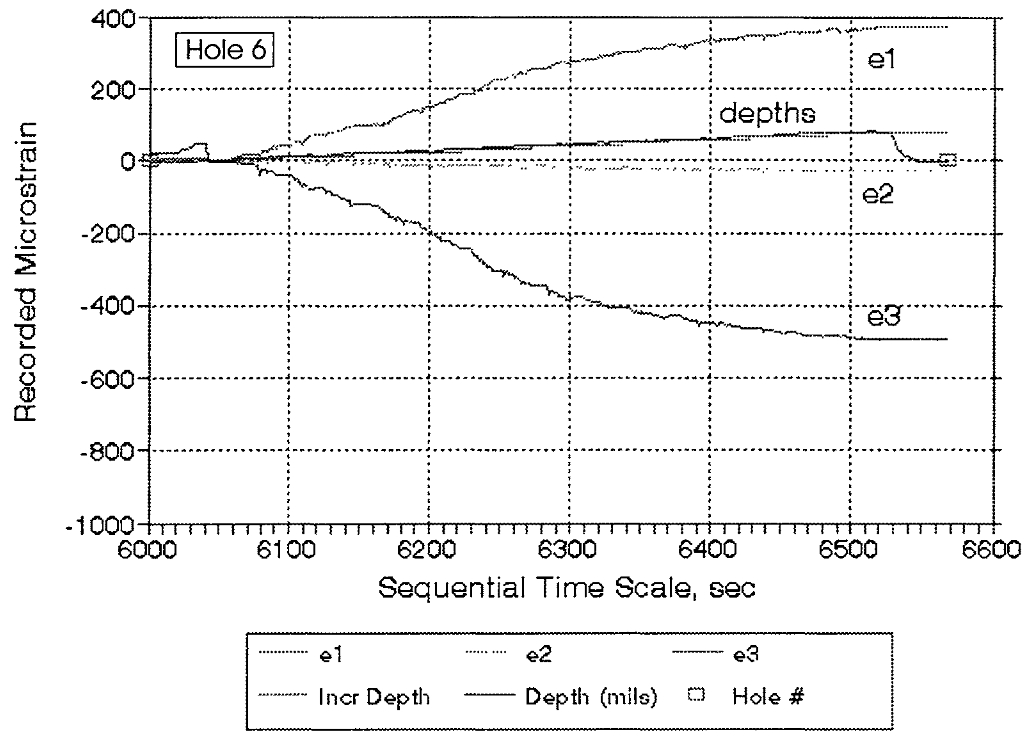

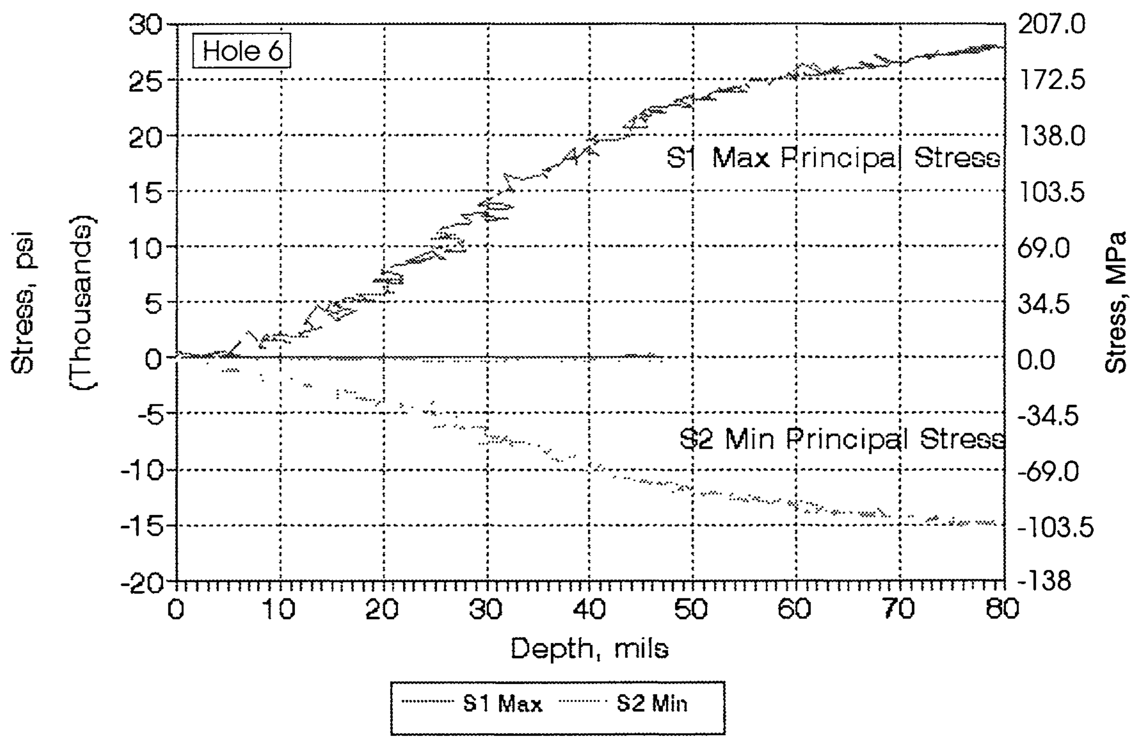

Figure 20. Microstrain vs. Elapsed Time and Stress vs. Depth for Hole 6.

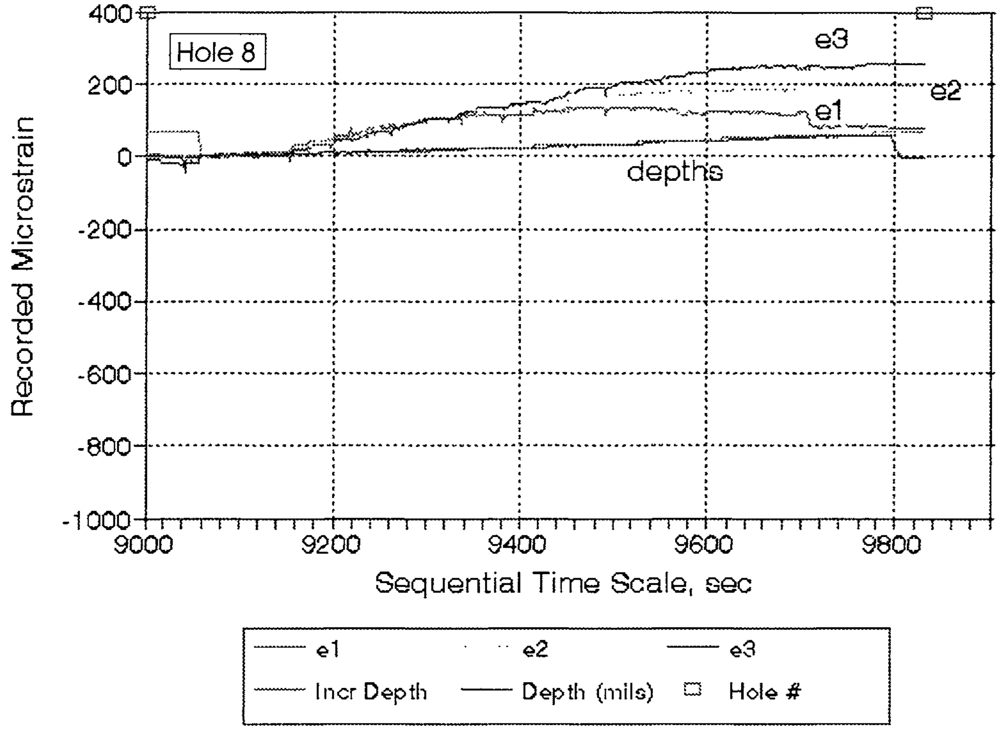

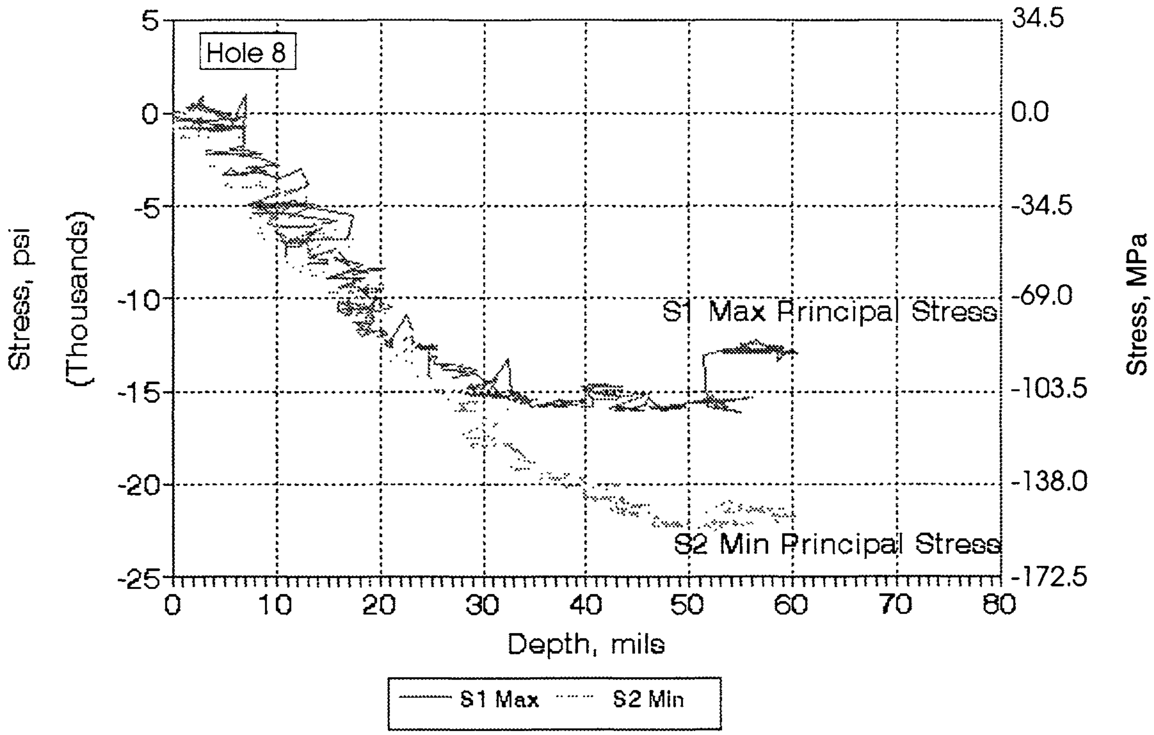

Figure 21. Microstrain vs. Elapsed Time and Stress vs. Depth for Hole 8.

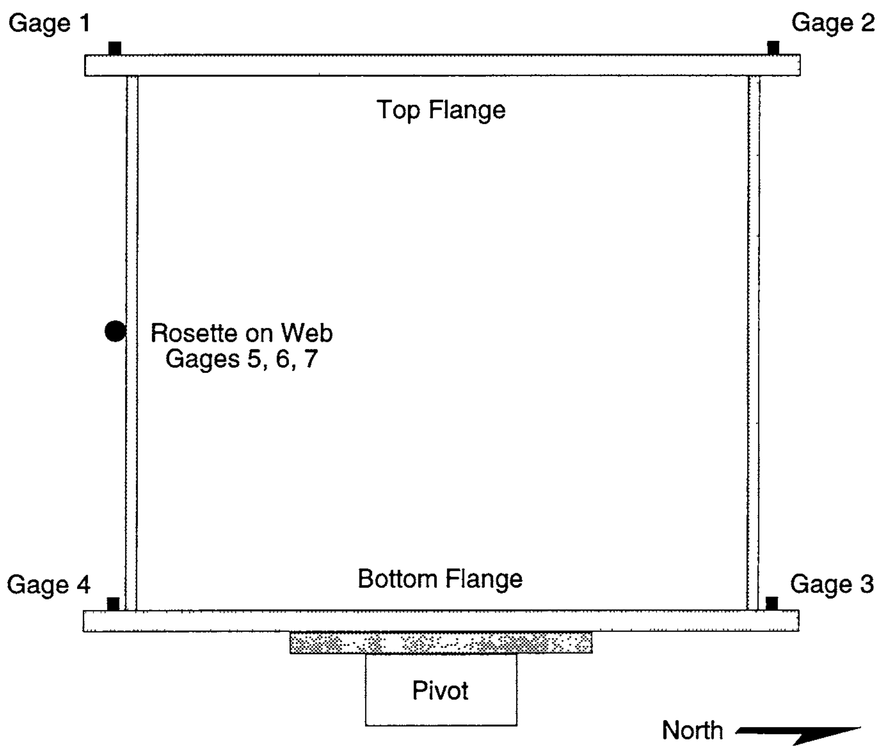

Figure 22. Box Girder Section at Midspan with Strain Gages for applied Stress Measurements.

Figure 23. Setup for Applied Stress Measurements.

(a) strain gages on top flange of box girder

(b) strain gages on bottom flange of box girder

(c) closeup of rosette gage at midheight of web

(d) receiver node connected to laptop computer.

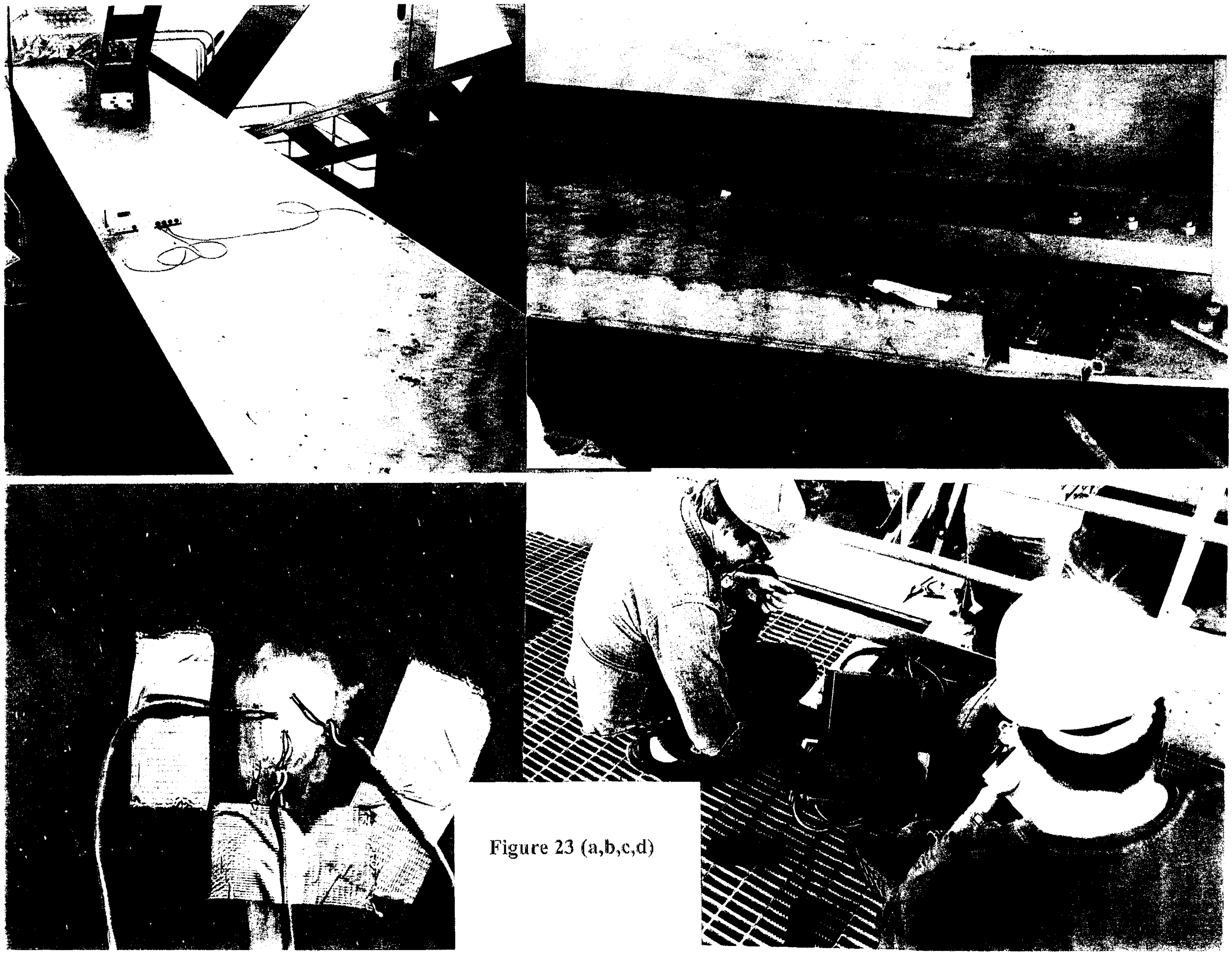

Figure 23 (a,b,c,d)

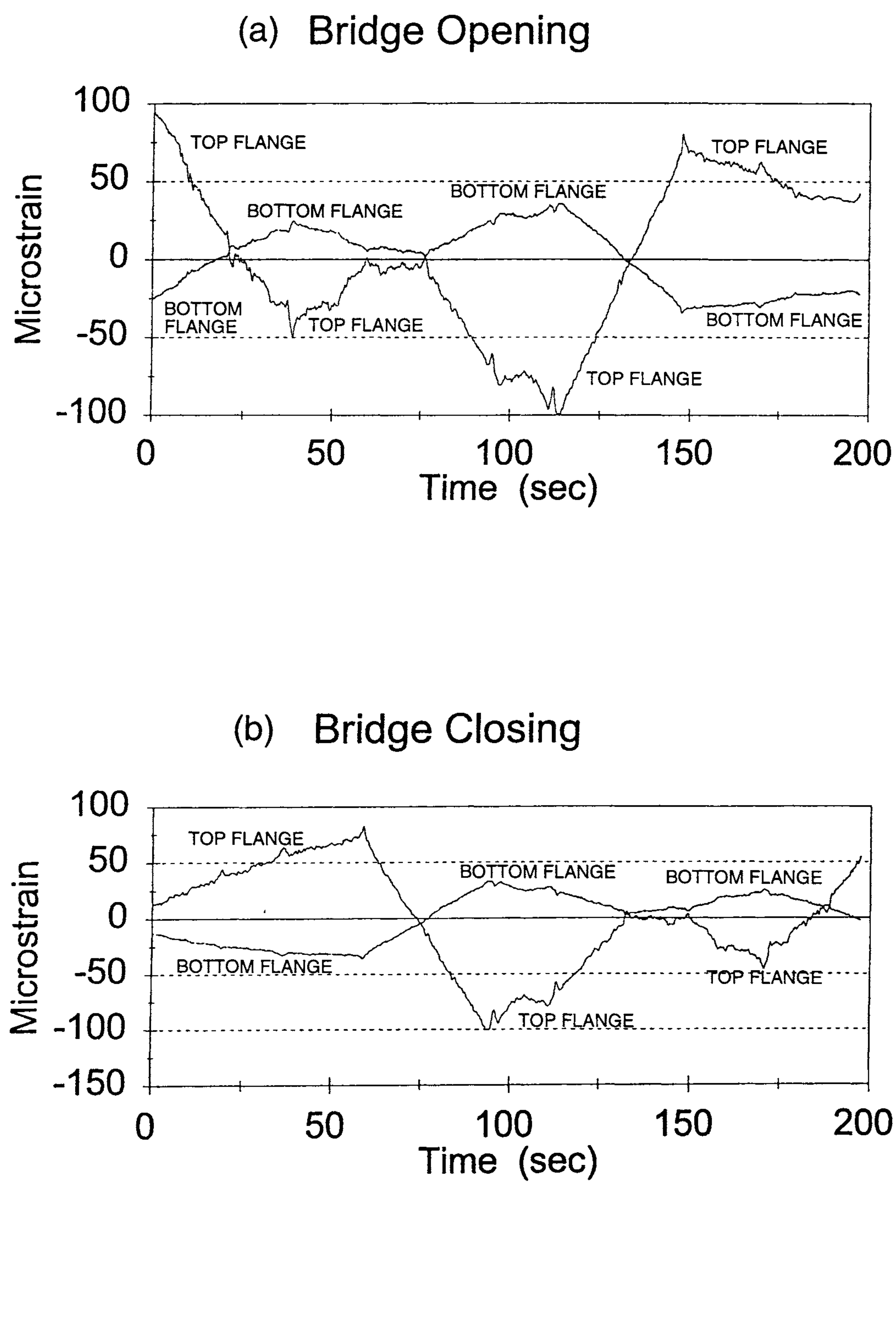

Figure 24. Average Strain in Top and Bottom Flange During Bridge Opening and Closing.

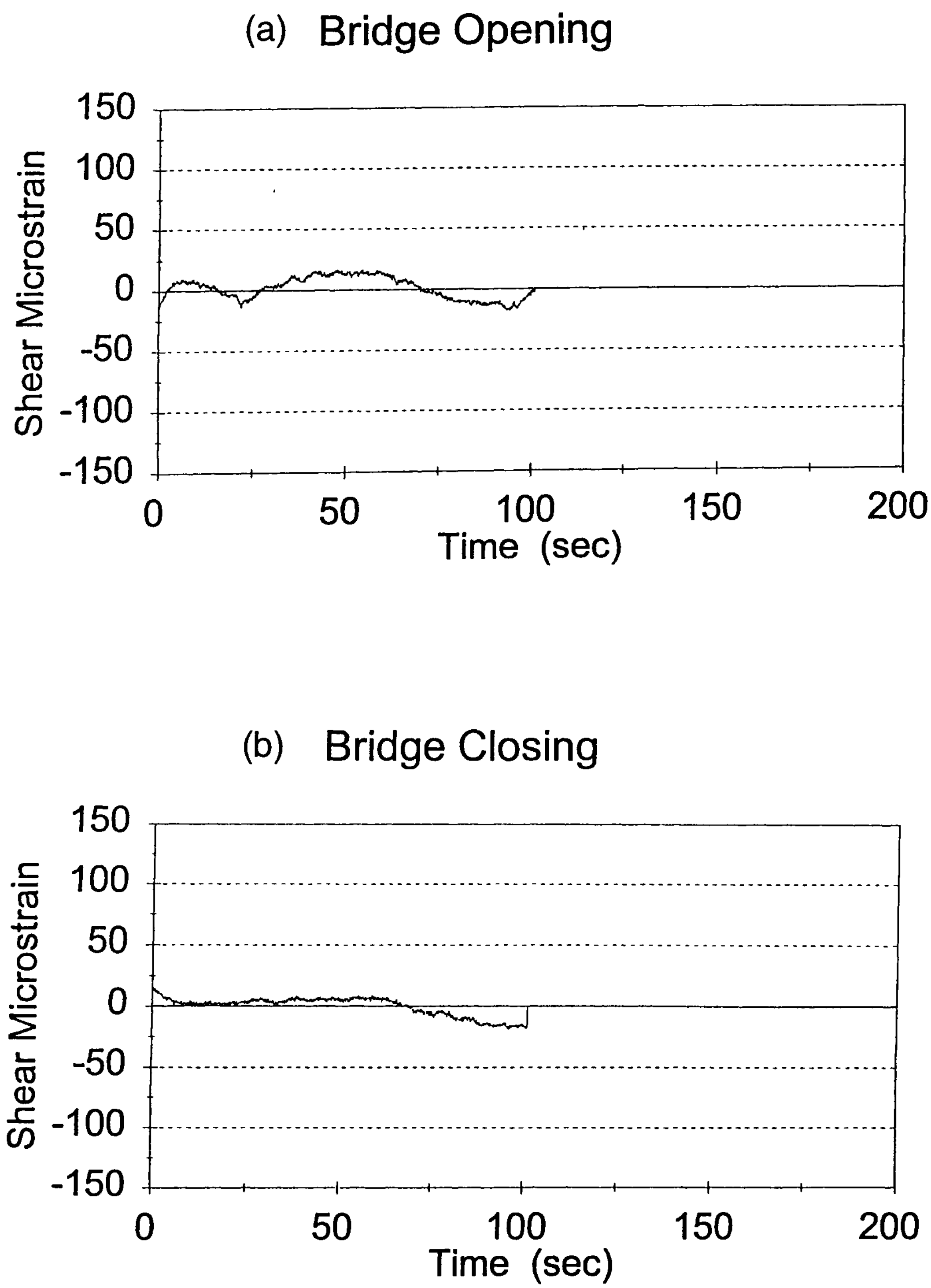

Figure 25. Shear Strain at Center of Web During Bridge Opening and Closing.

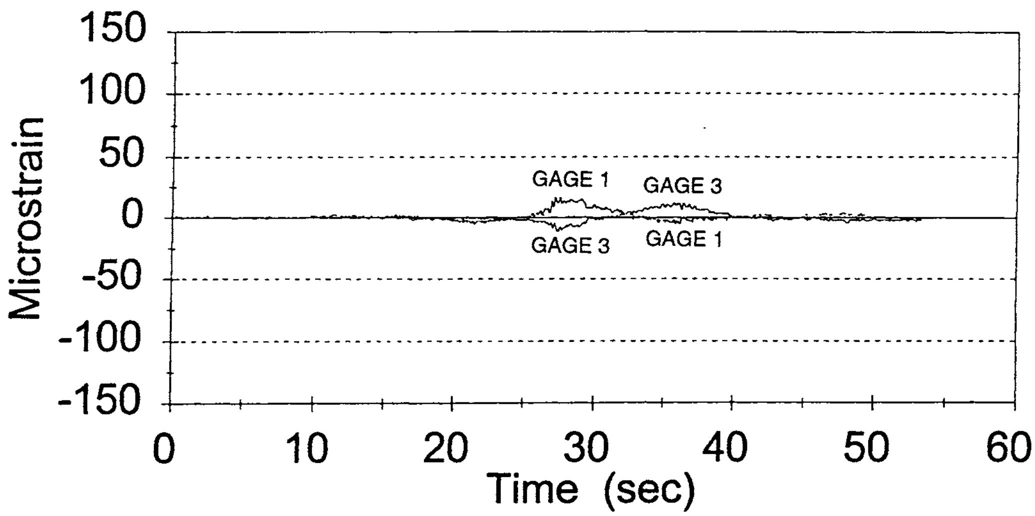

Figure 26. Live Load Strain Data for Two Trucks of Unknown Weight.

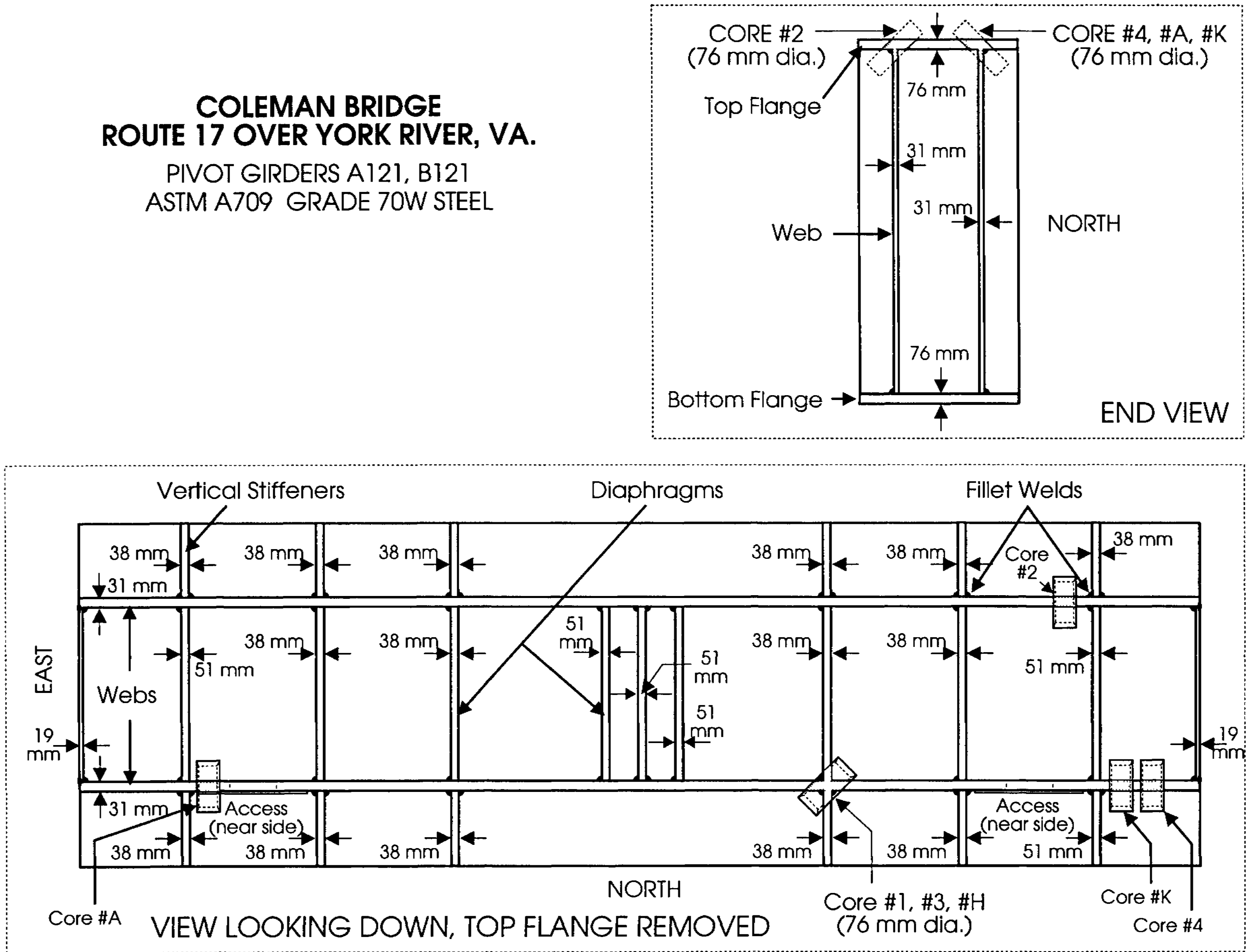

Figure 27. Locations of the Cores in the Pivot Girders.

Figure 28. General View of Cores 1, 2, 3, 4, A, H, and K.

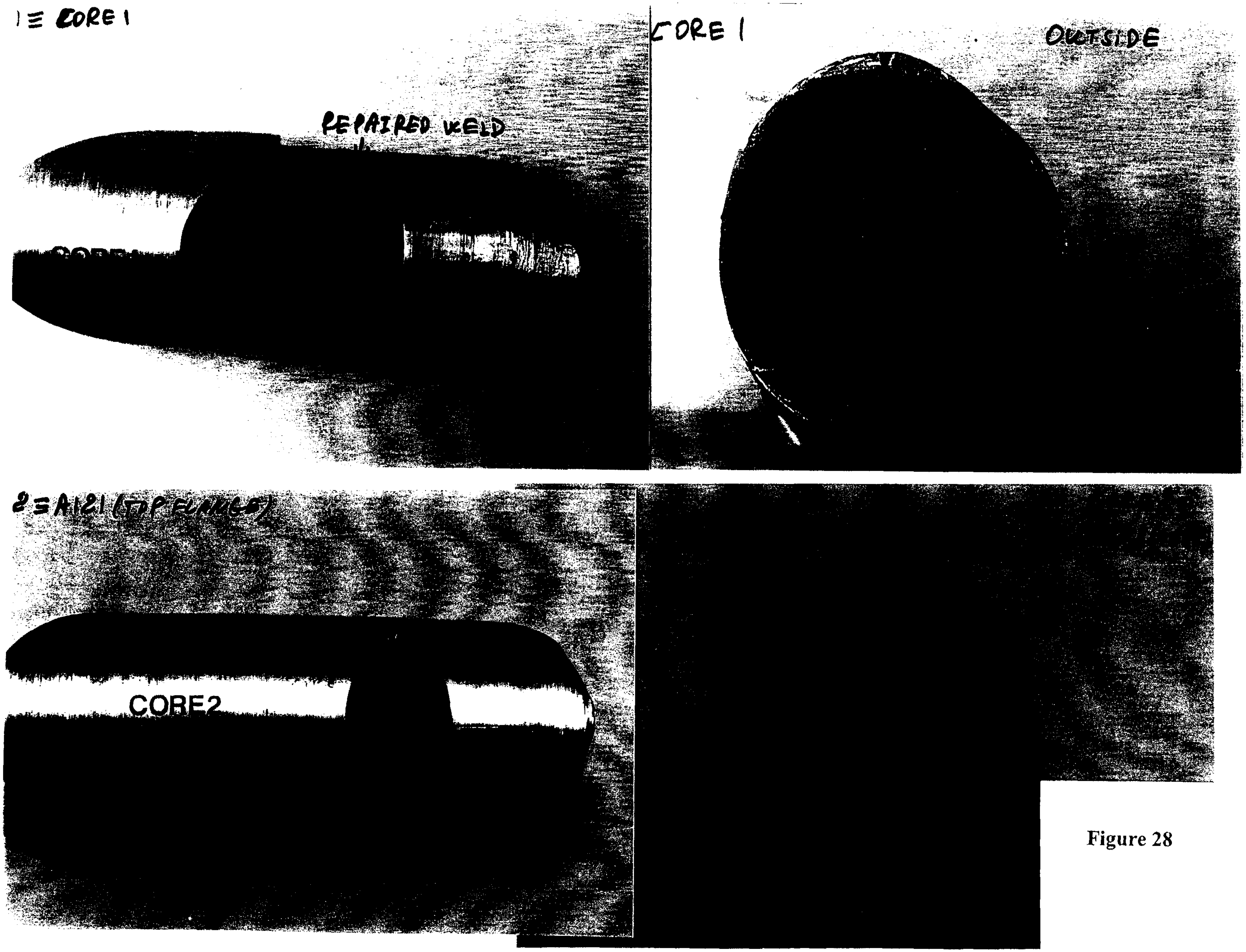

Figure 28

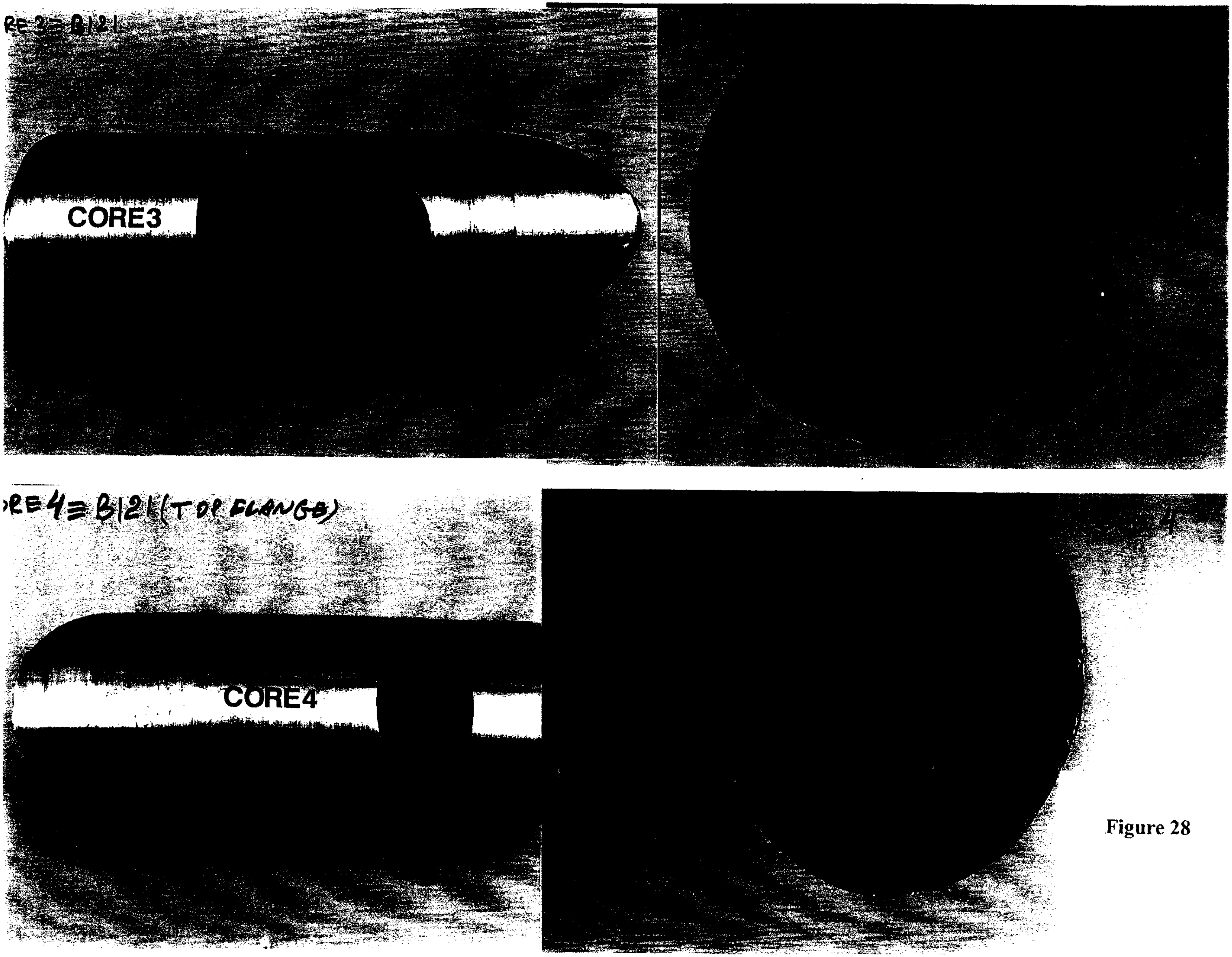

Figure 28

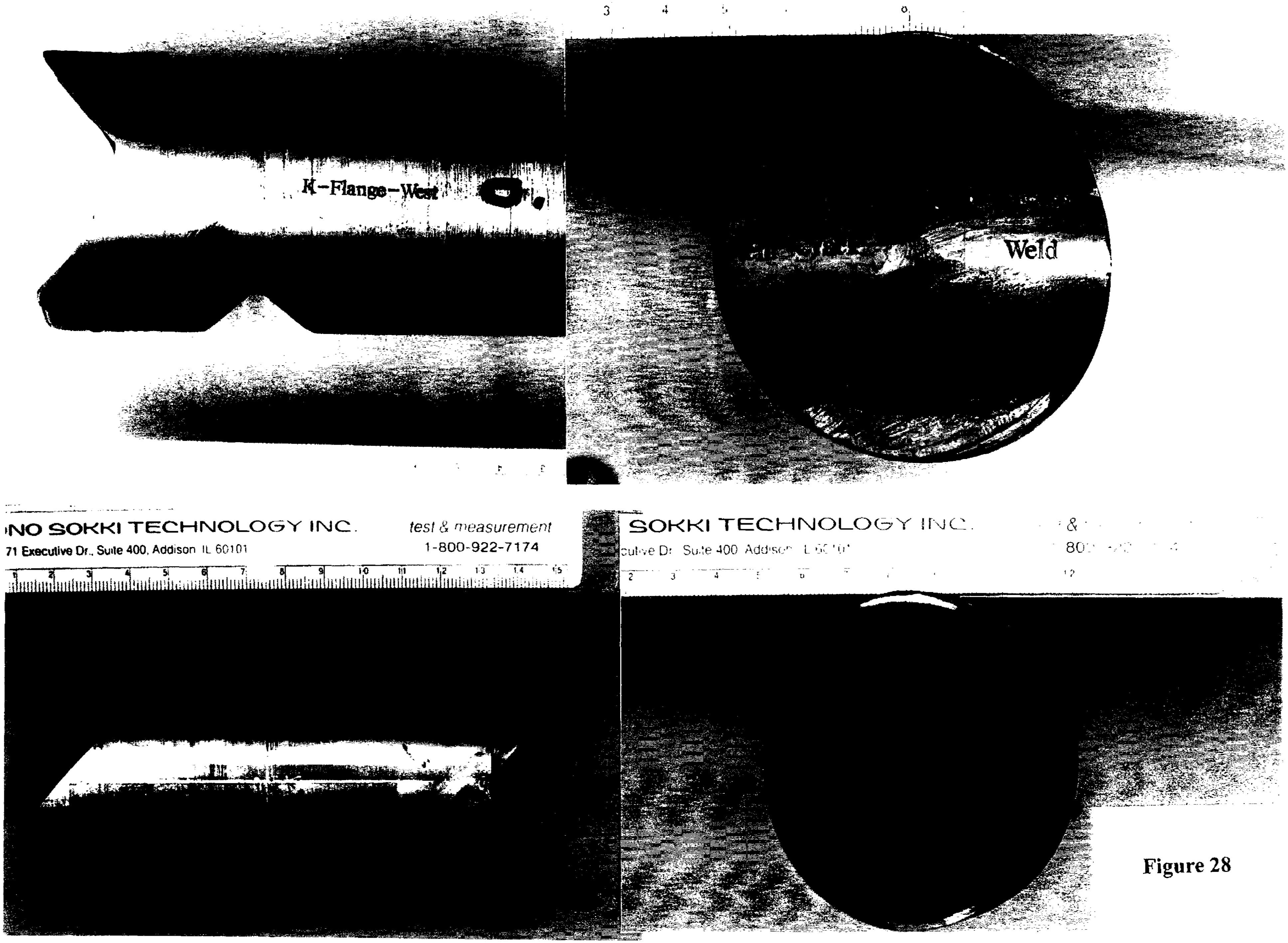
K-Flange-West
Weld
NO SOKKI TECHNOLOGY INC.
test & measurement
71 Executive Dr., Suite 400, Addison IL 60101
1-800-922-7174
SOKKI TECHNOLOGY INC.

Figure 28

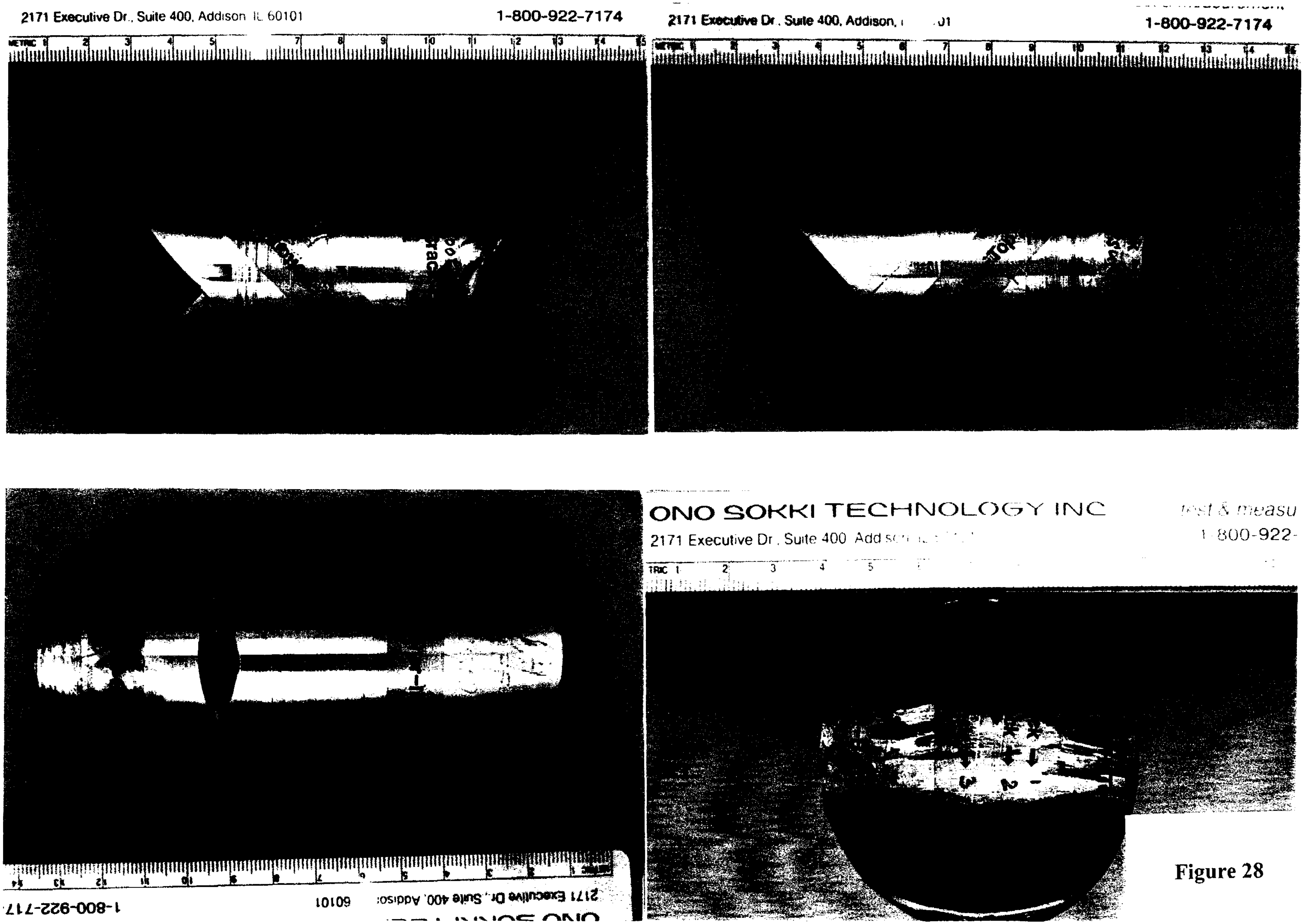
2171 Executive Dr., Suite 400, Addison IL 60101
1-800-922-7174
2171 Executive Dr., Suite 400, Addison,
1-800-922-7174
ONO SOKKI TECHNOLOGY INC
2171 Executive Dr., Suite 400, Addiso
60101
1-800-922-717

Figure 28

Figure 29. Radiographs.

(a) core A

(b) core K.

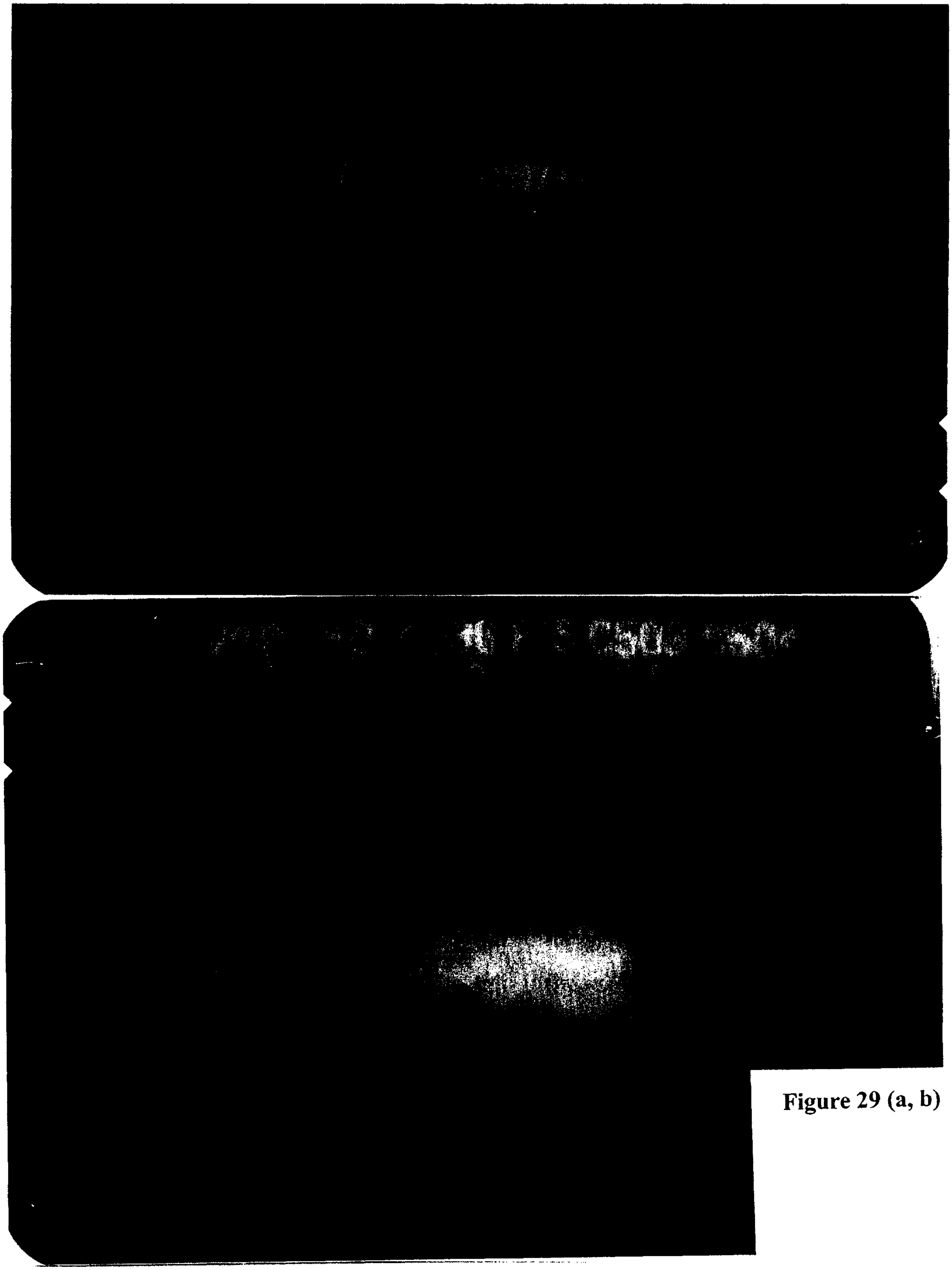

Figure 29 (a, b)

Figure 30. Crack Initiation Sites.

(a) longitudinal root crack in core H (1.3x)

(b) crack root of root crack in core H (200x)

(c) crack tip of root crack in core H (200x)

(d) metallurgical microstructure (tempered martensite and acicular ferrite) at crack tip of root crack in core H (1000x)

(e) longitudinal root cracks in core 4 (70x)

(f) weld-through longitudinal crack in core H (1.3x)

(g) crack root of weld-through crack in core H (200x)

(h) metallurgical microstructure (tempered martensite and acicular ferrite) at crack root of weld-through crack in core H (1000x)

(i) crack tip of weld-through crack in core H (200x)

(i) metallurgical microstructure (tempered martensite and acicular ferrite) at crack tip of weld-through crack in core H (1,000x).

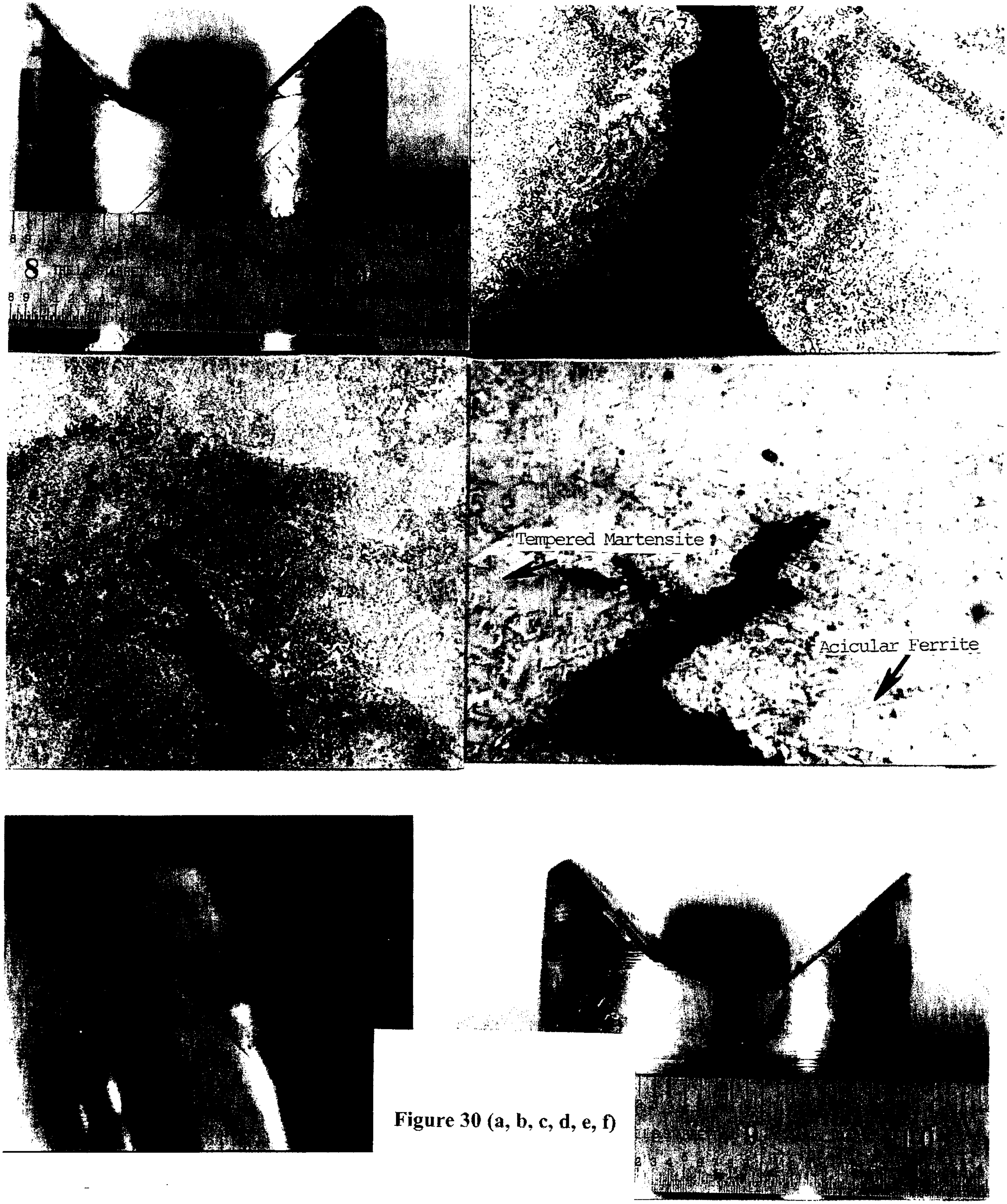

Figure 30 (a, b, c, d, e, f)

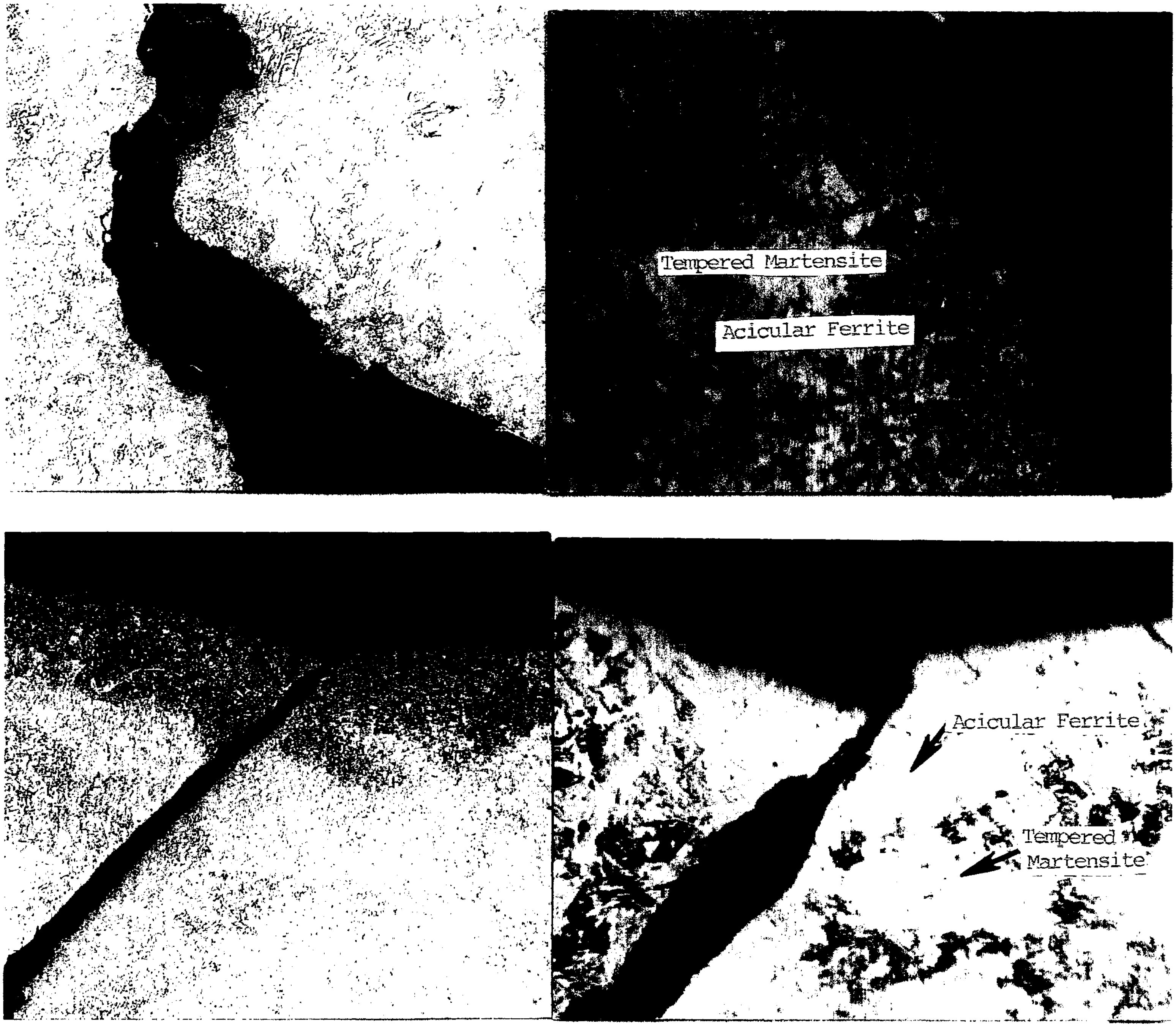

Figure 30 (g, h, i, j)

Figure 31. Fine Surface-Breaking Crack in Core 3.

(a) digital image of crack at higher magnification

(b) metallurgical microstructure of weld metal in cracked area (polygonal ferrite with lower bainite/martensite) (500x).

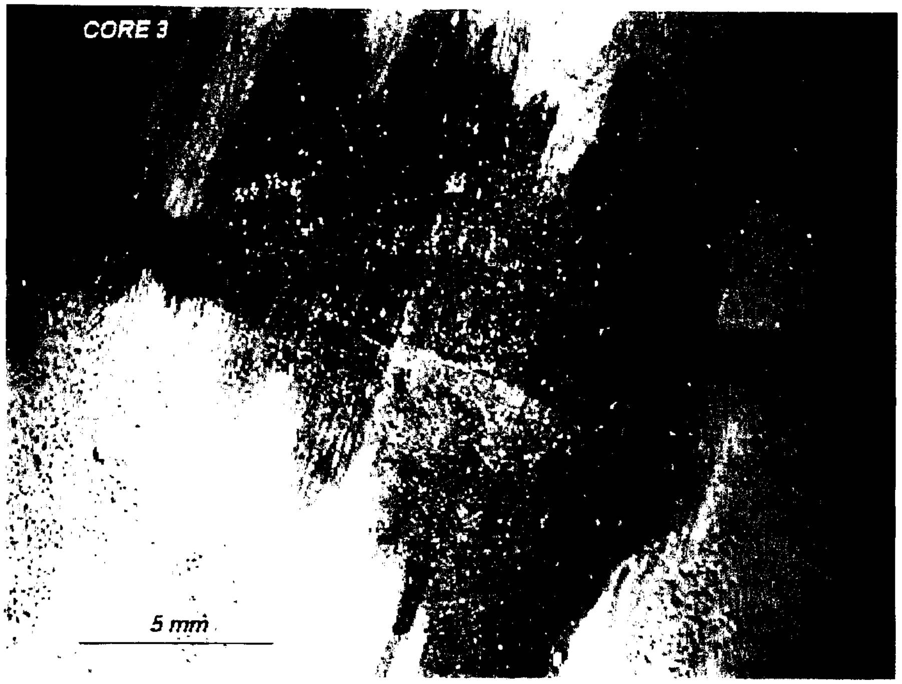

a)

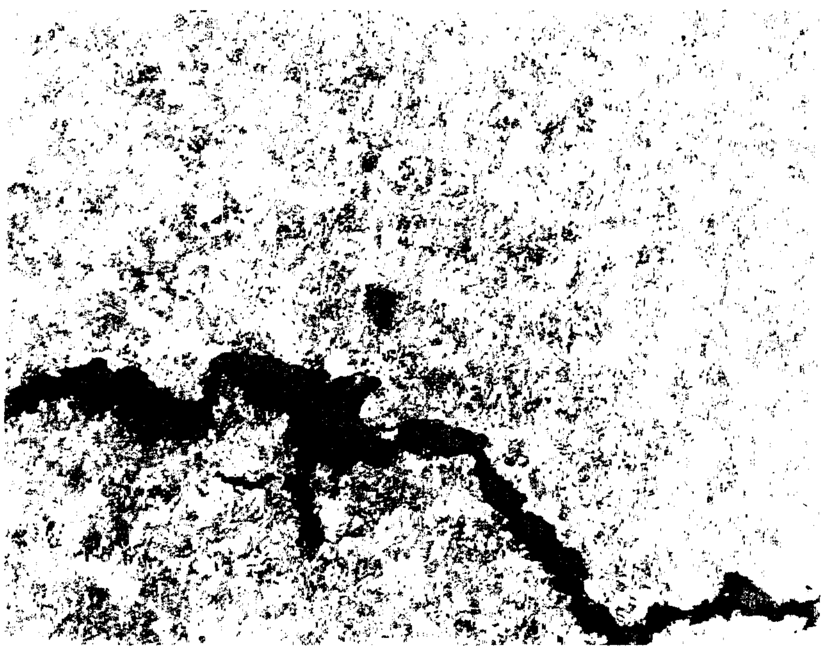

b)

Figure 31

Figure 32. Macro-Micro Examination of Weld-Through Transverse Crack A1 Detected in Core A.

(a) fractography of exposed fracture surface (0.35x)

(b) micrometallography of crack propagating in base metal of top flange (50x)

(c) projected crack path (200x)

(d) metallurgical microstructure (tempered martensite and acicular ferrite) at crack tip (1000x).

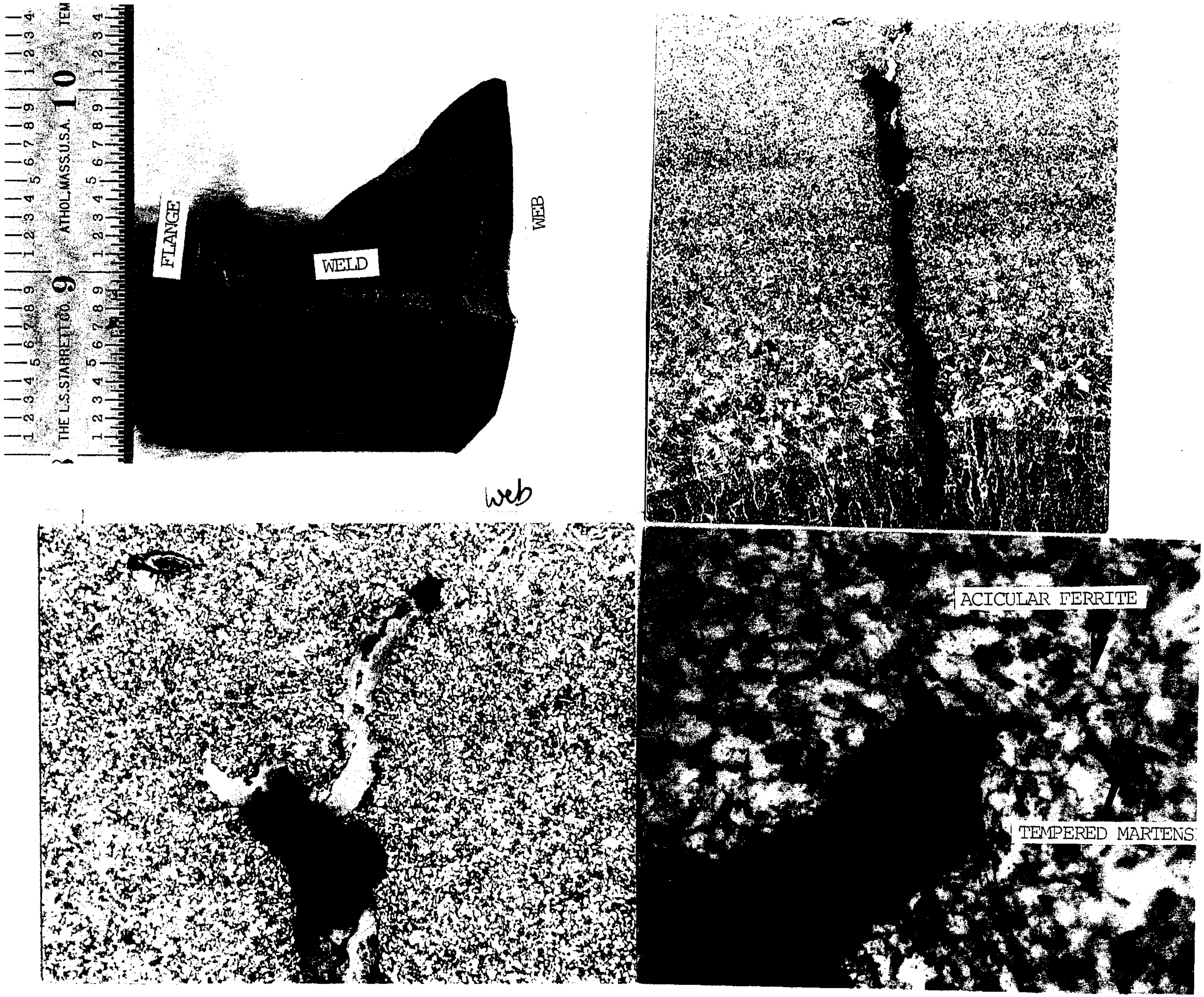

Figure 32 (a, b, c, d)

Figure 33. Macro-Micro Examination of Weld-Through Transverse Crack Detected in Core A.

(a) fractography of exposed fracture surface (1.6x)

(b) fractography of features characteristic of ductile tensile overload

(c) fractography of intergranular appearance (35x)

(d) fractography of intergranular facets (2000x).

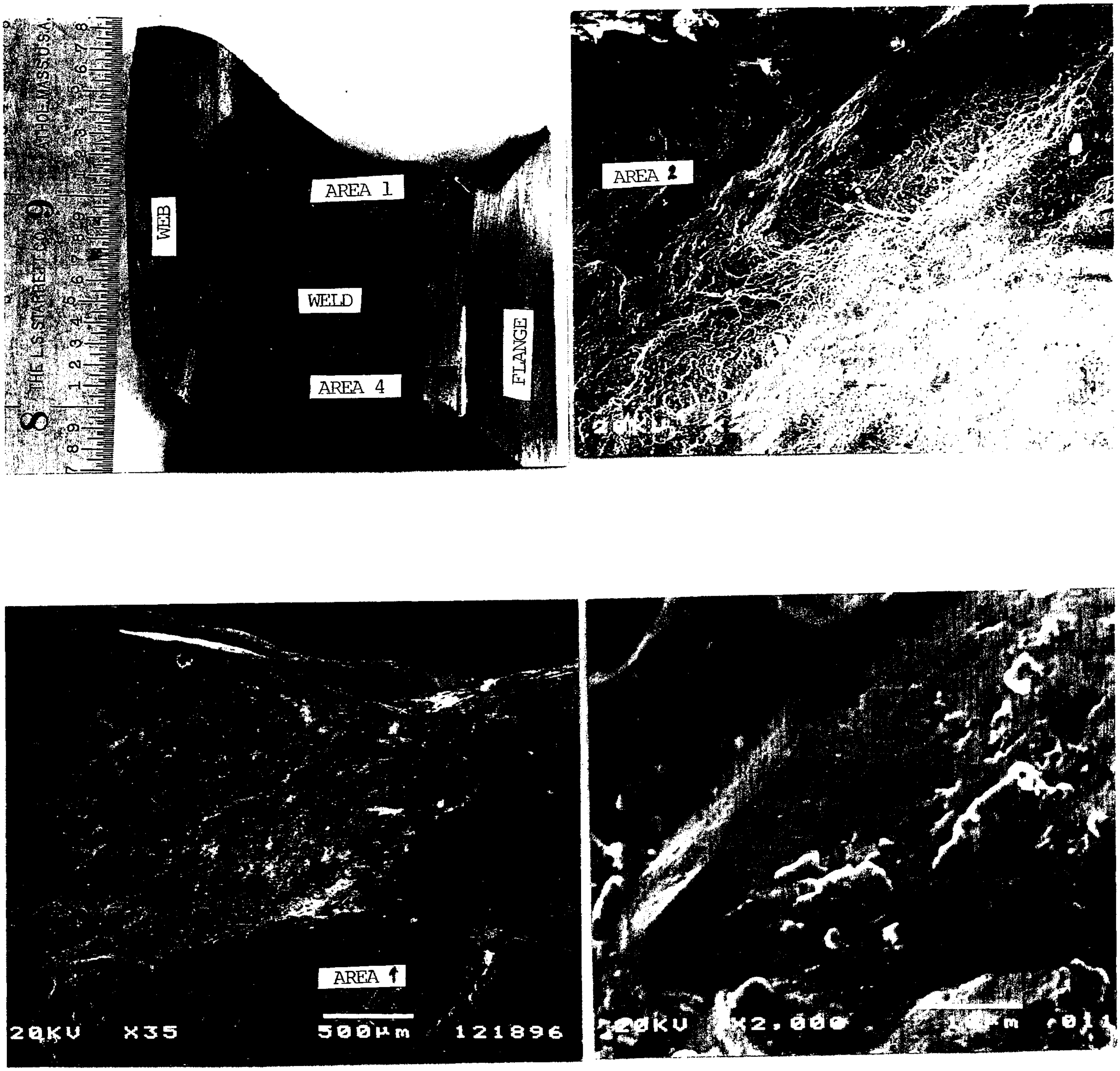

Figure 33 (a, b, c, d)

Figure 34. Fractography of Ductile Tearing and Quench Cracking Features in Exposed Fracture Surface of Cores H and A.

(a) crack 1 in core H (350x)

(b) crack 2 in core H (1000x)

(c) near root of crack A1 in core A (500x)

(d) near tip of crack A1 in core A (500x).

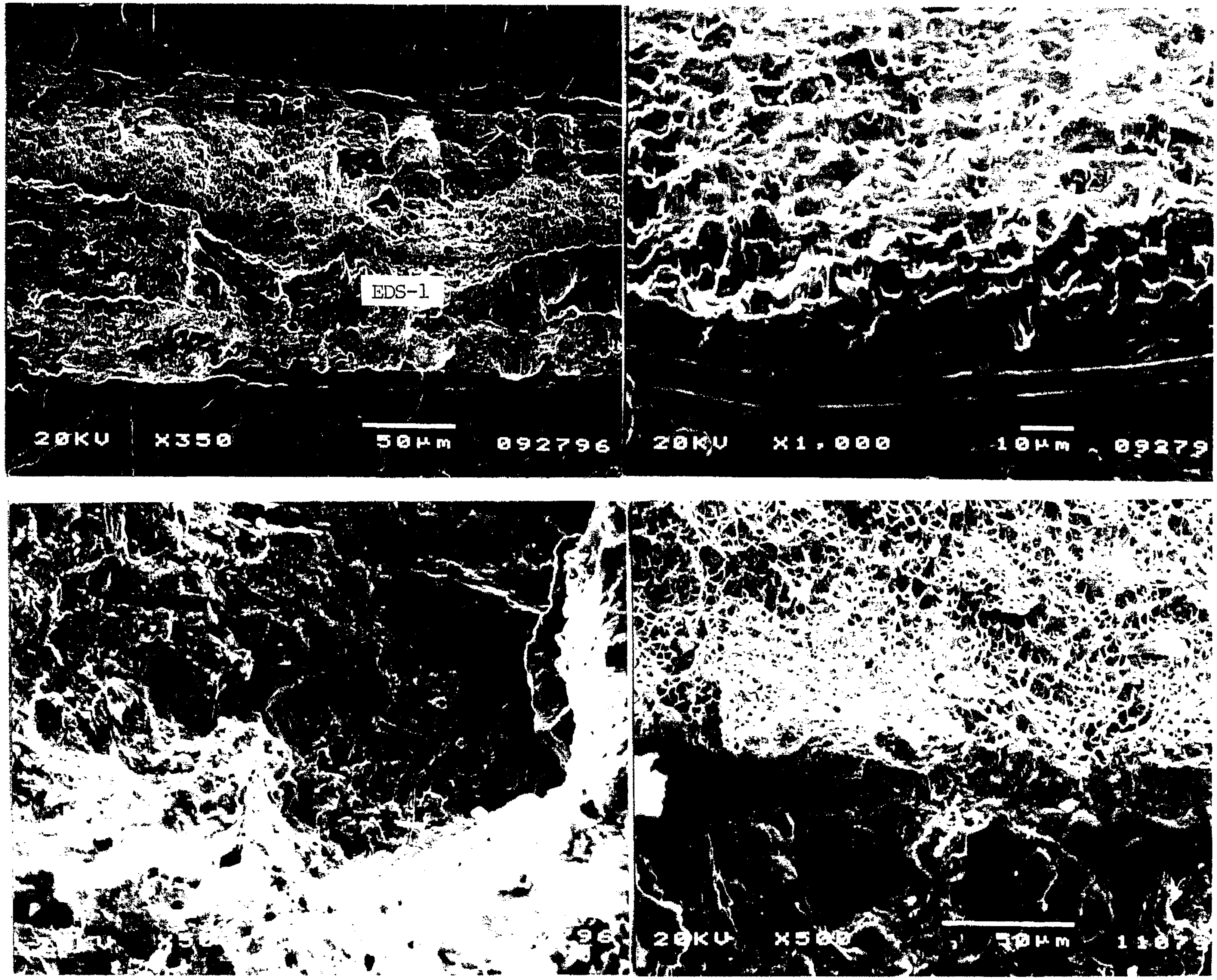

Figure 34 (a, b, c, d)

Figure 35. Fractography of Small Inclusions in Surface of Weld and Base Metal CVN Samples.

(a) weld metal CVN sample C1, core 4

(b) weld metal CVN sample C2, core 4

(c) base metal CVN sample, core A, locations EDS-1 and EDS-2

(d) base metal CVN sample, core A, location EDS-3.

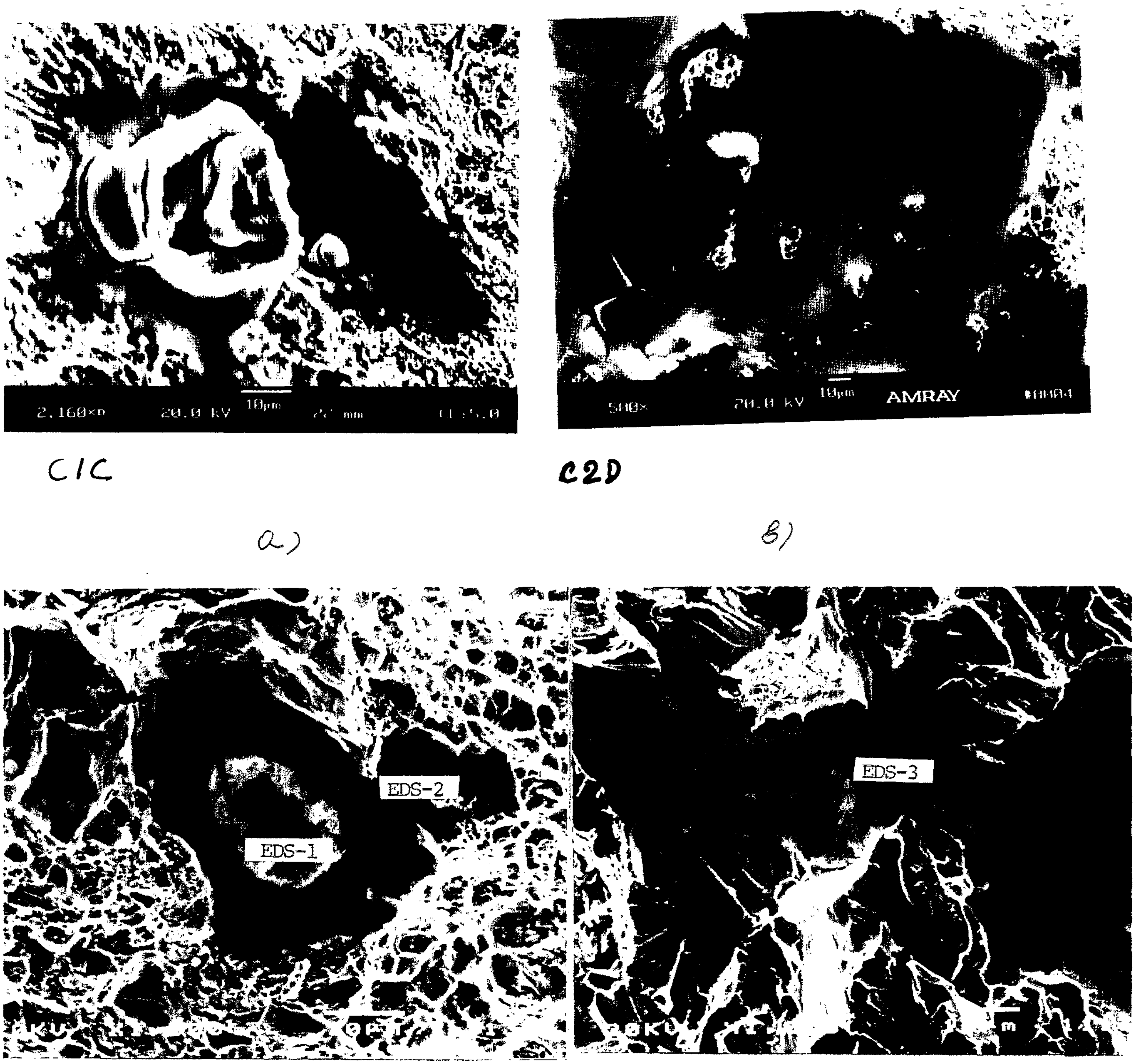
2,160×
20.0 kV
10μm
500×
20.0 kV
10μm
AMRAY
C1C
C2D
a)
b)
EDS-2
EDS-1
EDS-3
c)
d)

Figure 35

Figure 36. Metallurgical Microstructure of Base Metal (top flange, web and stiffener).

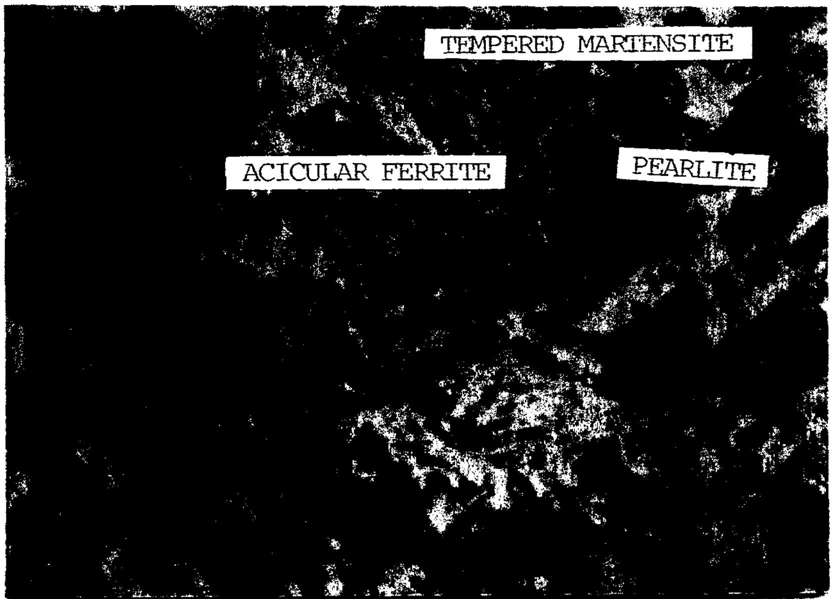

Core A
Top Flange

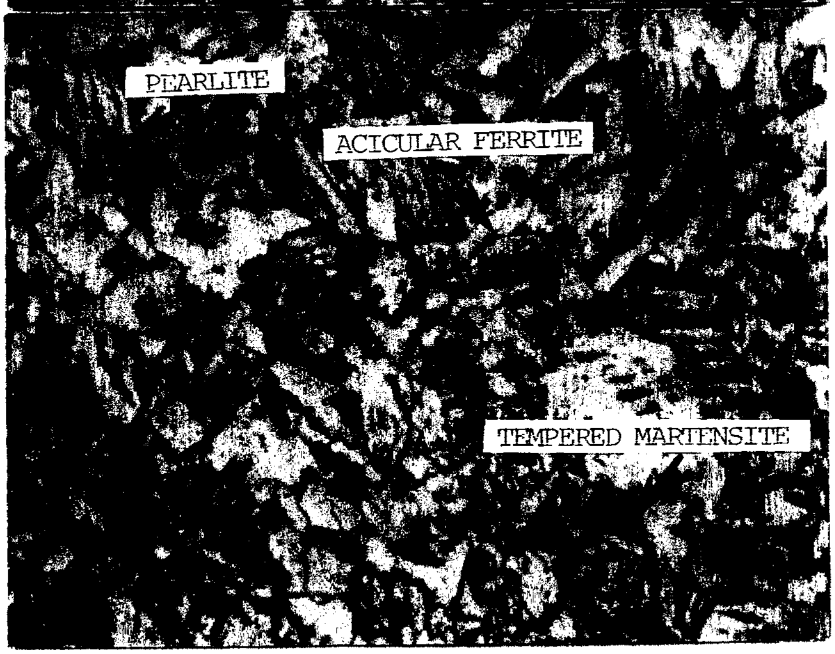

Core A
Web

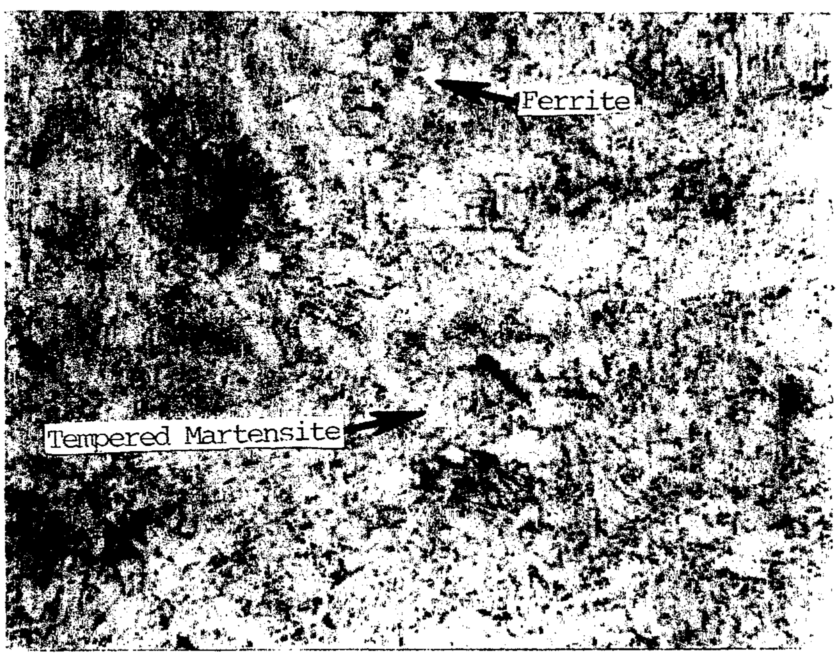

Core K
Stiffener

Figure 36

Figure 37. Metallurgical Microstructure of Weld Metal.

Core 2: Weld metal—columnar dendritic and polygonal grains of lower bainite/martensite with grain boundary ferrite (widmanstaten) and acicular ferrite; fusion zone—equiaxed grains of tempered martensite; HAZ—polygonal grains of lower bainite/martensite.

Core 3: Weld metal—columnar and cellular grains with grain boundary ferrite (widmanstaten) and areas of lower bainite/martensite with acicular ferrite; fusion zone—equiaxed grains of lath martensite; HAZ—polygonal ferrite grains with lower bainite/martensite.

Core 4: Weld metal—columnar dendritic grains with grain boundary ferrite (widmanstaten) and areas of lower bainite/martensite with acicular ferrite; fusion zone—equiaxed grains of tempered martensite; HAZ—polygonal ferrite grains with areas of lower bainite/martensite.

Core A: Weld metal—columnar appearance with acicular ferrite and tempered martensite; fusion zone—columnar appearance with acicular ferrite, widmanstatten ferrite, and tempered martensite; HAZ—acicular ferrite and tempered martensite.

Core K: Weld metal—columnar appearance with acicular ferrite and tempered martensite; fusion zone—columnar appearance with acicular ferrite, widmanstatten ferrite, and tempered martensite; HAZ—acicular ferrite and tempered martensite.

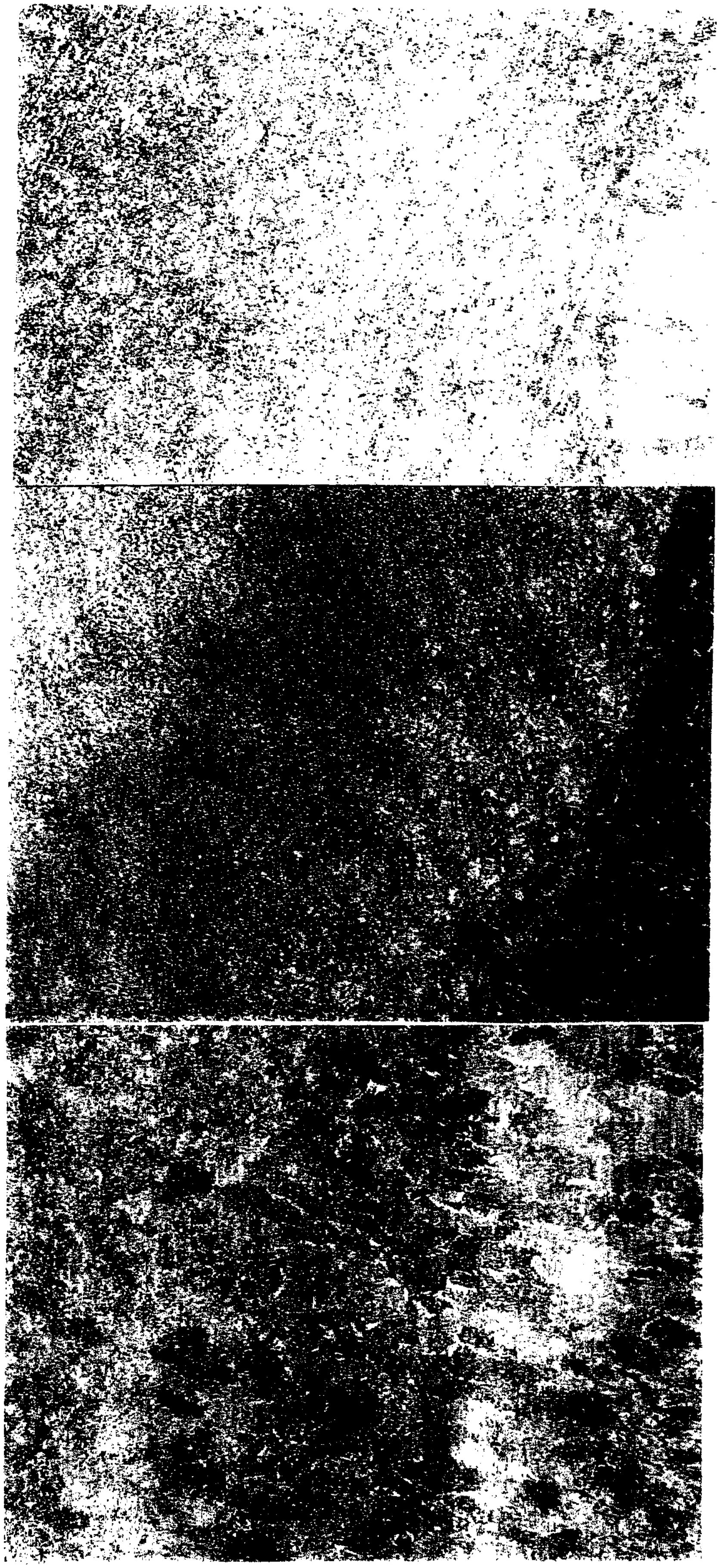

WELD - C4
HAZ
BASE METAL

WELD + HAZ + BASE METAL
C5

WELD - C5

Figure 37

Core 2

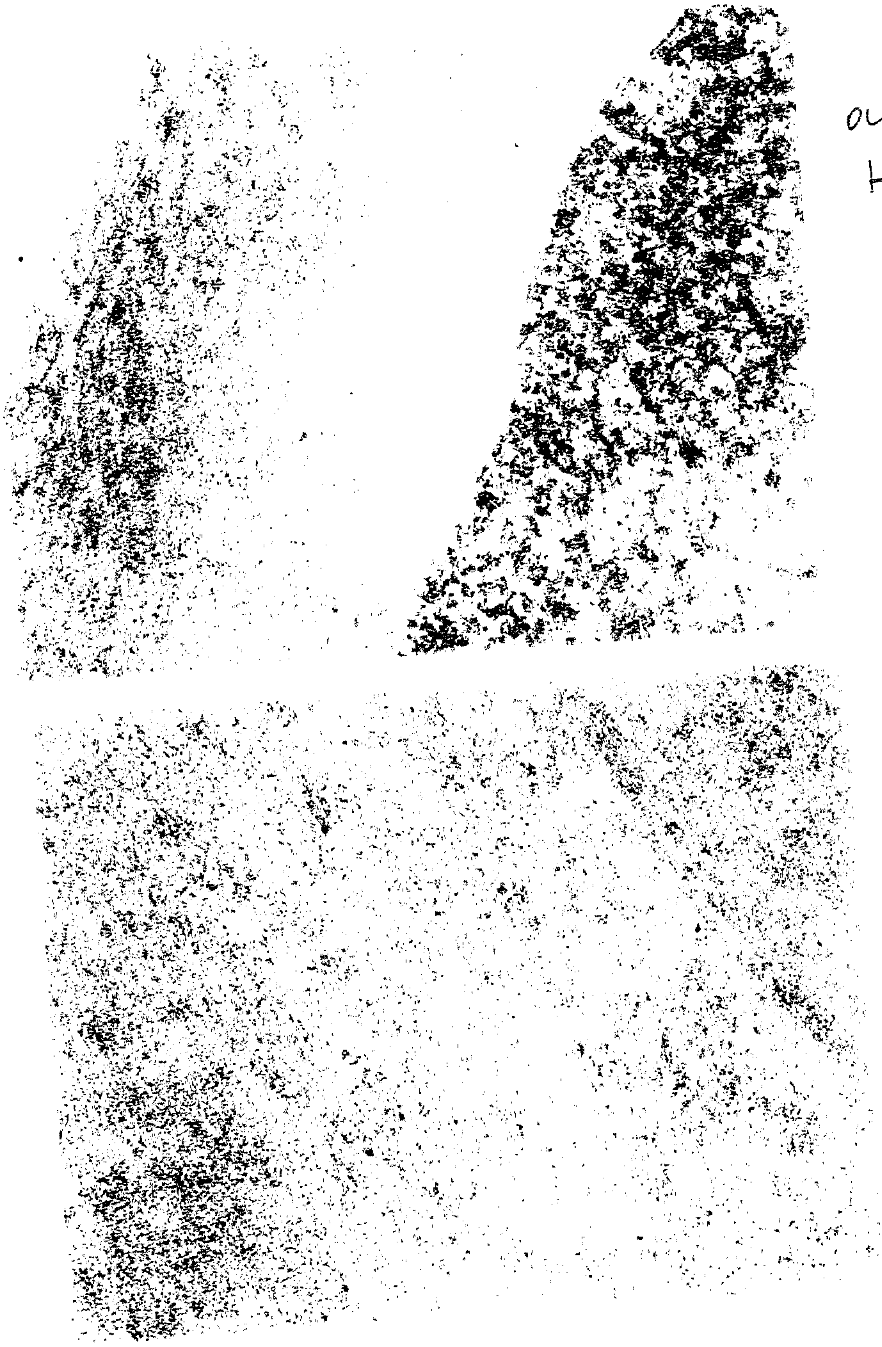

OUTSIDE WELD + HAZ + BASE METAL

INSIDE WELD + HAZ + BASE METAL

Figure 37

Core 3

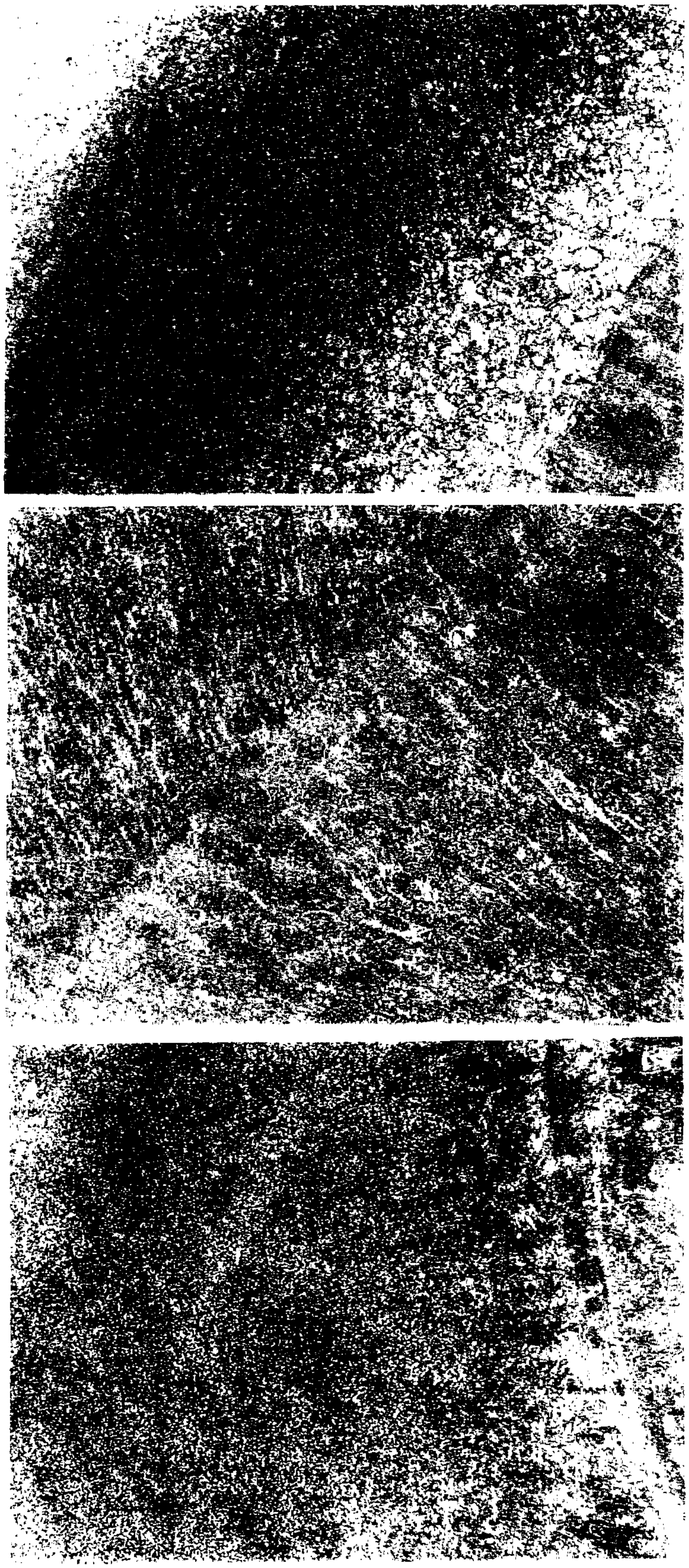

C1 - WELD + HAZ + BASE METAL

C2 - WELD + HAZ

WELD + HAZ + BASE METAL C3

Figure 37

Core 4

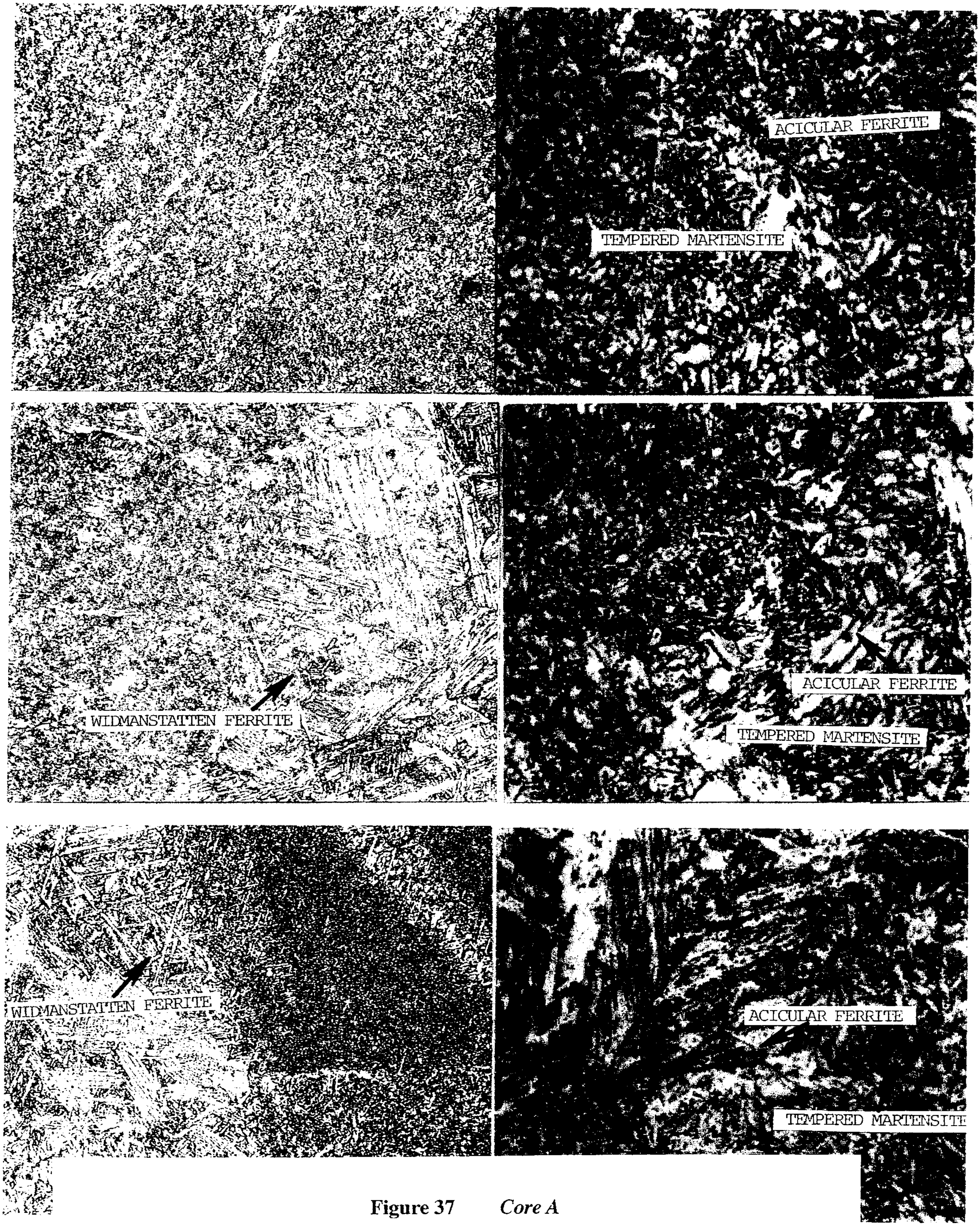

Figure 37 *Core A*

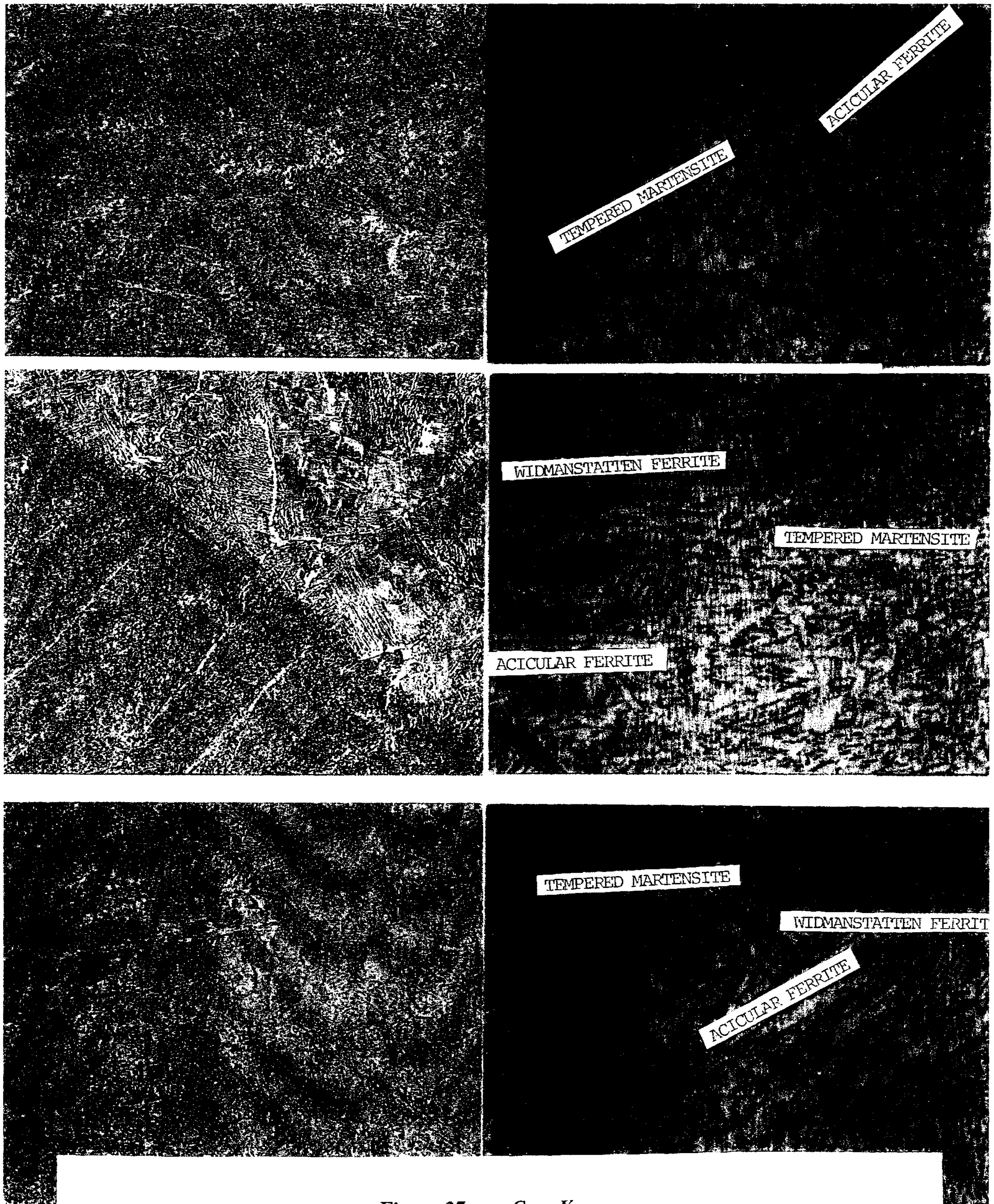

Figure 37 *Core K*

Figure 38. Micrometallography of Intergranular Fracture Bound by Polygonal Ferrite Grains and Tempered Martensite in Weld of Core 3 (100x).

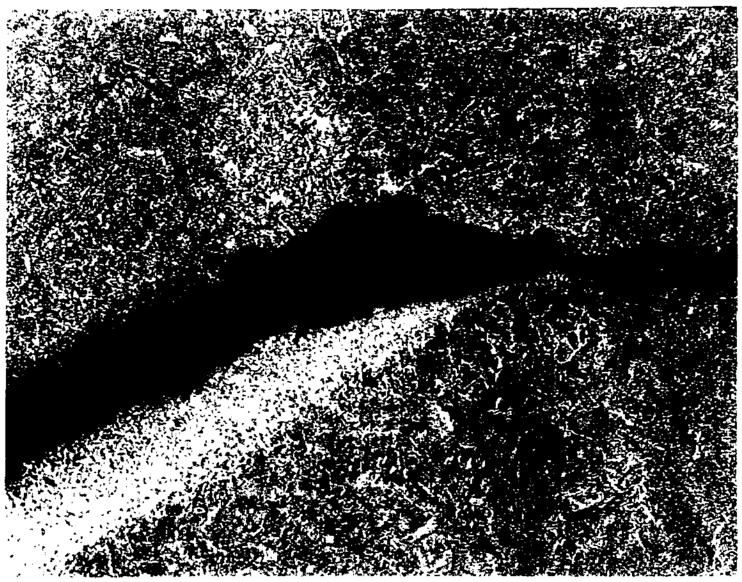

Figure 38

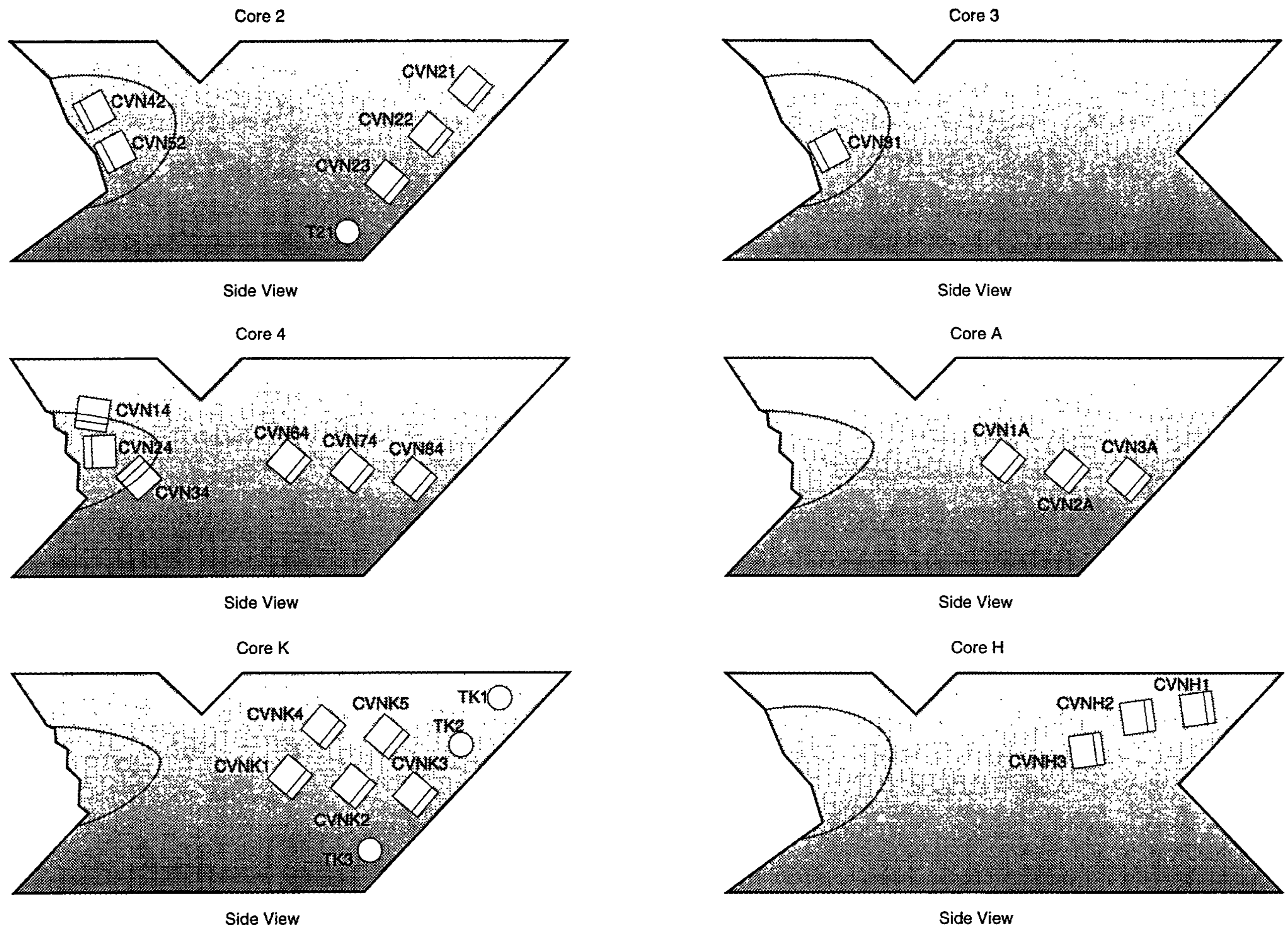

Figure 39. Locations of Test Specimens Fabricated from Cores.

Figure 40. Broken CVN Samples.

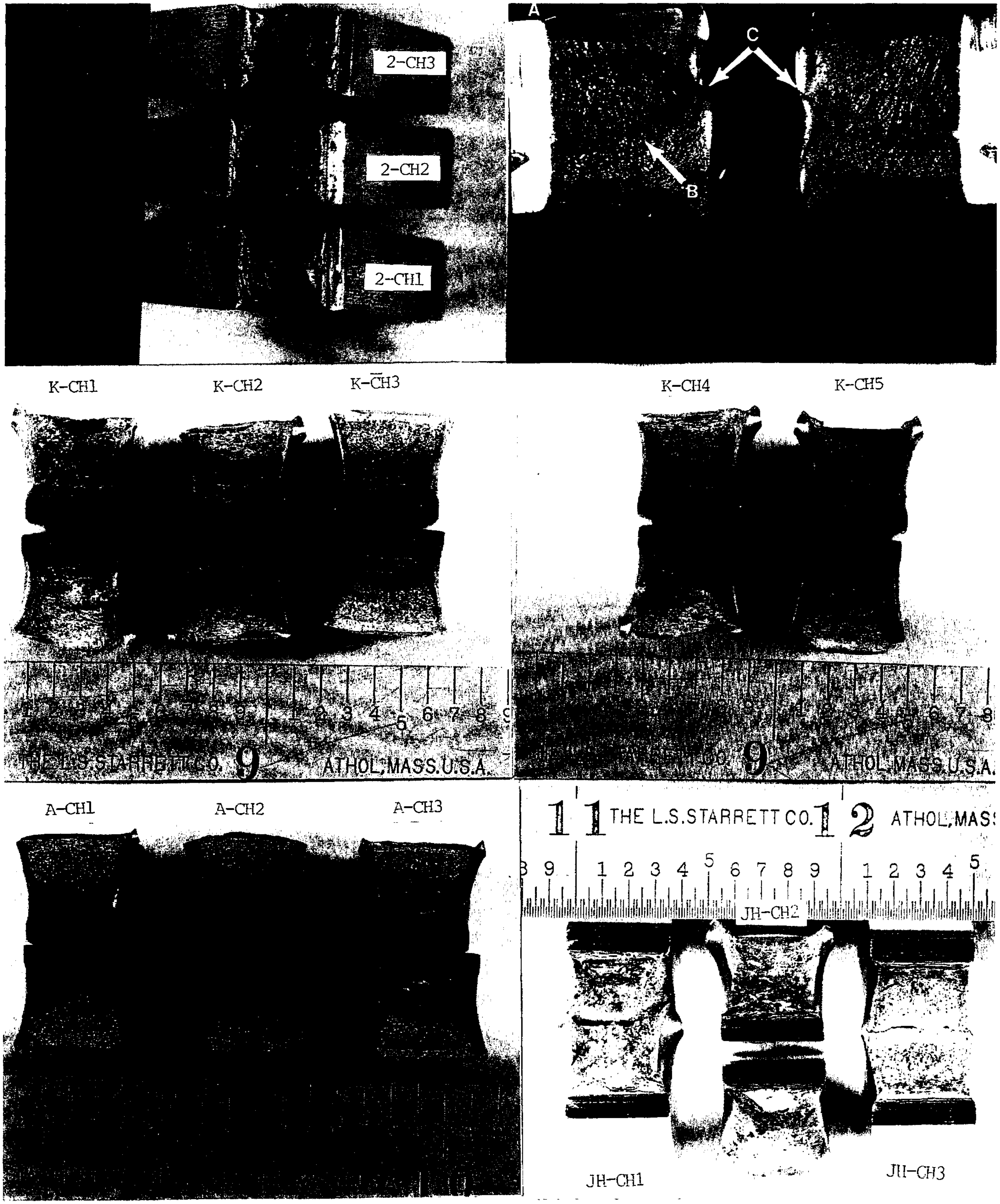
2-CH3
2-CH2
2-CH1
A
C
B
K-CH1
K-CH2
K-CH3
K-CH4
K-CH5
THE L.S.STARRETT CO.
ATHOL, MASS. U.S.A.
A-CH1
A-CH2
A-CH3
THE L.S.STARRETT CO.
ATHOL, MASS
JH-CH2
JH-CH1
JH-CH3

Figure 40

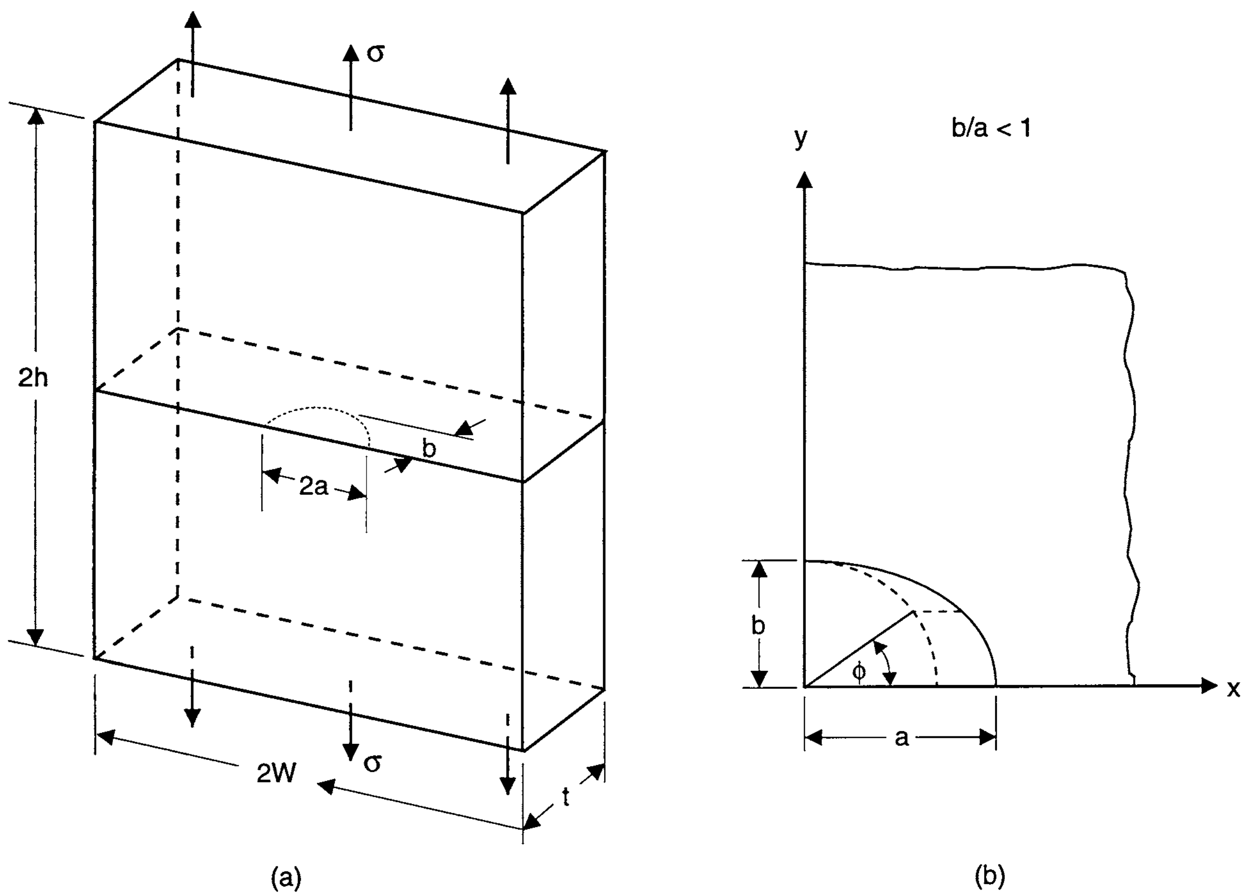

b	- Depth of crack	W	- Width of top flange overhanging the web
2a	- Surface length of crack	2h	- Length of top flange (essentially infinite)
t	- Thickness of top flange	ϕ	- Location around crack profile

Figure A1. Crack Dimensions for Fracture Mechanics Analysis.

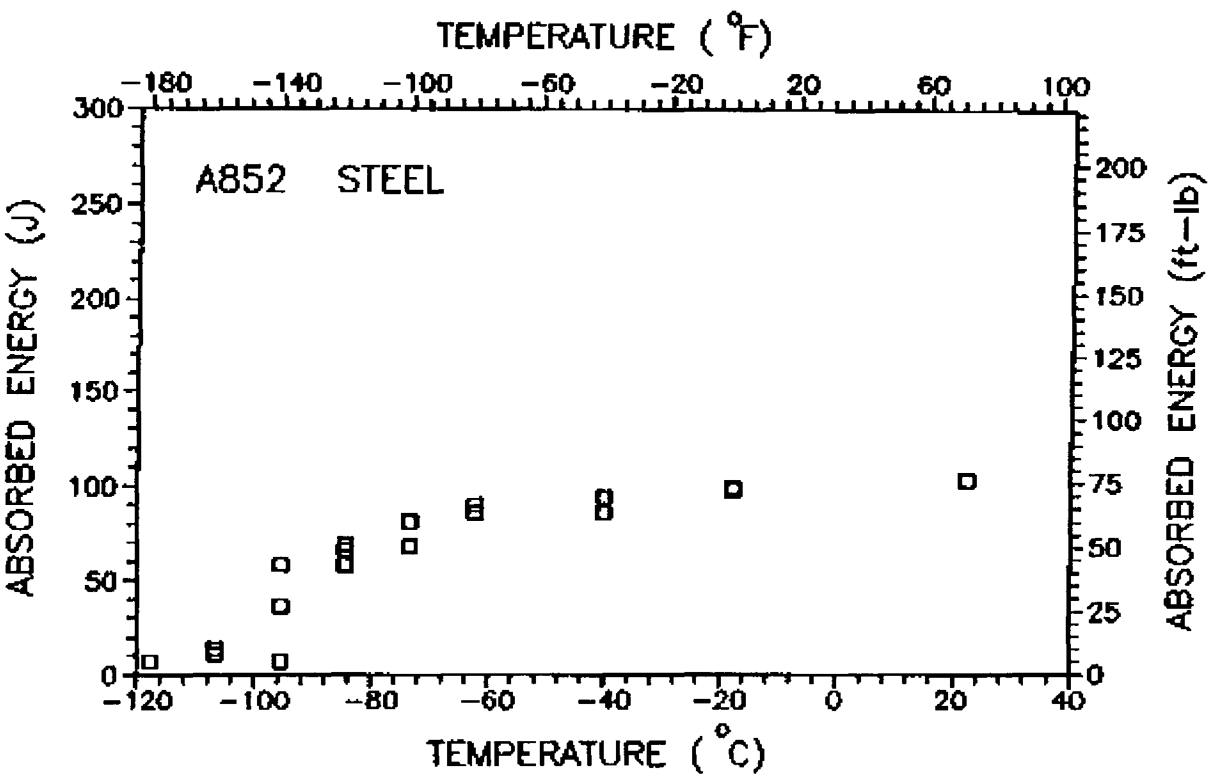

Figure A2. Absorbed Energy vs. Temperature.